January 2016

Low power CMOS IC, biosensor and wireless power transfer techniques for wireless sensor network application

Young-Joon Kim
Purdue University

Graduate School Form
30 Updated 12/26/2015

PURDUE UNIVERSITY
GRADUATE SCHOOL
Thesis/Dissertation Acceptance

This is to certify that the thesis/dissertation prepared

By Young-Joon Kim

Entitled
Low Power CMOS IC, Biosensor and Wireless Power Transfer Techniques for Wireless Sensor Network Application

For the degree of Doctor of Philosophy

Is approved by the final examining committee:

Pedro P. Irazoqui (Chair)	Timothy S. Fisher
Vijay Raghunathan	
Byunghoo Jung	
Kaushik Roy	

To the best of my knowledge and as understood by the student in the Thesis/Dissertation Agreement, Publication Delay, and Certification Disclaimer (Graduate School Form 32), this thesis/dissertation adheres to the provisions of Purdue University's "Policy of Integrity in Research" and the use of copyright material.

Approved by Major Professor(s): Pedro P. Irazoqui, Chair

Approved by: Venkataramanan (Ragu) Balakrishnan 7/26/2016

Head of the Departmental Graduate Program Date

LOW POWER CMOS IC, BIOSENSOR AND WIRELESS POWER TRANSFER TECHNIQUES FOR WIRELESS SENSOR NETWORK APPLICATION

A Dissertation

Submitted to the Faculty

of

Purdue University

by

Young-Joon Kim

In Partial Fulfillment of the

Requirements for the Degree

of

Doctor of Philosophy

August 2016

Purdue University

West Lafayette, Indiana

To my family.

ACKNOWLEDGMENTS

I would like to thank Dr. Pedro P. Irazoqui for his patience and support. I also would like to thank my advisory committee members Dr. Kaushik Roy, Dr. Vijay Raghunathan, Dr. Timothy Fisher and Dr. Byunghoo Jung for taking time out from their busy schedules to review this work. I appreciate all the members in the CID group for their technical discussion and friendship, especially Dr. Jimin Maeng, for help with fabrication, and Hansraj Bhamra, Yuwen Huang for their friendship along the long journey. This work was supported by Defense Advanced Research Projects Agency (DARPA).

TABLE OF CONTENTS

Page

LIST OF TABLES

LIST OF FIGURES

Figure Page

Figure Page

Figure Page

ABSTRACT

Kim, Young-Joon, Purdue University, August 2016. Low Power CMOS IC, Biosensor and Wireless Power Transfer Techniques for Wireless Sensor Network Application. Major Professor: Pedro P. Irazoqui.

The emerging field of wireless sensor network (WSN) is receiving great attention due to the interest in healthcare. Traditional battery-powered devices suffer from large size, weight and secondary replacement surgery after the battery life-time which is often not desired, especially for an implantable application. Thus an energy harvesting method needs to be investigated. In addition to energy harvesting, the sensor network needs to be low power to extend the wireless power transfer distance and meet the regulation on RF power exposed to human tissue (specific absorption ratio). Also, miniature sensor integration is another challenge since most of the commercial sensors have rigid form or have a bulky size. The objective of this thesis is to provide solutions to the aforementioned challenges.

The focus of this presentation is on integration of technologies for implantable wireless sensor network. Firstly, a low power IC for the radio, which consumes most of the power, is fabricated using CMOS technology. This transceiver harvests energy from 915MHz RF radiation power signal. Also, the powering signal provides reference clock to the IC for low power frequency synthesis. A simple receiver is implemented on chip for multi-node access. Then wireless powering techniques were studied to improve the current work. Wireless power transfer (WPT) link distance for implantable devices in prosthetic arm application (targeted muscle reinnervation) is less than 10 cm. At this distance, wireless power transfer using magnetic resonance coupling (MRC) can be much more effective in power transfer efficiency. By focusing on this point, a design technique

using band pass filter theory allows transferring power selectively to a specific target device. Selective WPT enables multi-node access without having to use any further techniques, greatly simplifying the system. A low power SoC is designed to comply with the proposed WPT technique, also dedicated for glucose detection using 180nm CMOS technology. The IC is composed of a low power transmitter based on injection locked ring oscillator. The wireless sensor IC receives power wirelessly from MRC through 27 MHz (ISM band) and transmits in 405 MHz (MICS band). Since our glucose sensor is an amperometric sensor, the IC detects current from the biosensor and mirrors it to an internal ring oscillator, which presents the glucose level in frequency (I-F conversion). Frequency variation due to temperature can be calibrated out through an internal reference clock. Total power consumption of the system is around 20 μW. To complete the system, a glucose sensor is designed and fabricated with graphene petals on carbon fiber. Efforts were focused on flexible, robust and sensitive glucose sensor based on multilayered graphene petals (GP) on thin carbon fiber (CF) tow. GP/CF electrode was decorated with the mixture of Pt nanoparticles (PtNPs), polyaniline (PANI), glucose oxidase (GOx), and nafion. PtNP are electrodeposited onto the graphene for its catalytic behavior toward hydrogen peroxide, which is generated in the process of glucose oxidase (GOx) oxidizing glucose, acting as an electron-transfer promoter. The GOx/PANI/PtNP/GP/CF biosensor showed highly flexible characteristics with good sensitivity and it showed more than 90% of its sensitivity after 4 weeks in phosphate buffered saline (PBS) solution.

1. INTRODUCTION

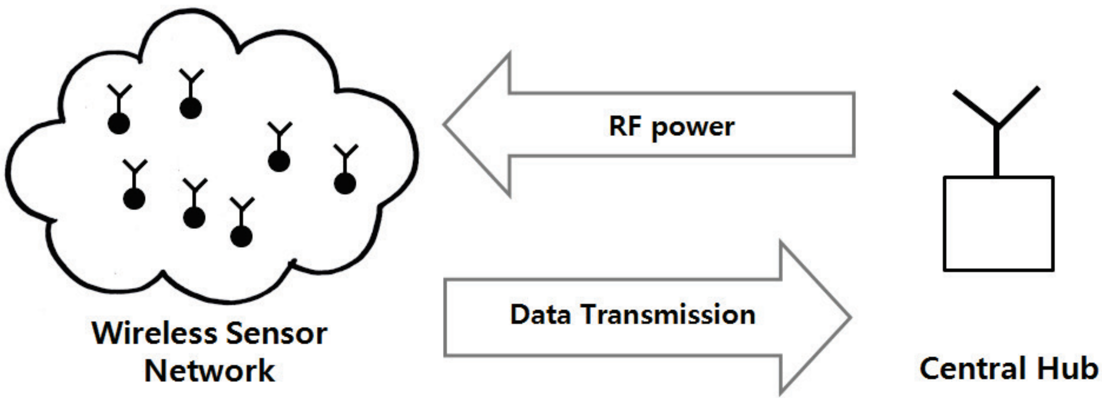

Fig. 1.1 Wireless sensor network with multiple nodes

1.1. Motivation

Wireless sensor networks (WSN) are receiving a great amount of spotlight due to the fast developing technology and focus in medical technology [1]. It is the key technology for smart healthcare. However, in biomedical application, the sensors are required to be compact, low power consuming and battery-less [2]. To meet the requirements, application-specific integrated circuit (ASIC) design is necessary[3]. Therefore, the implementation of a low power transmitter and effective wireless power transfer is needed for wireless sensor network in biomedical application. Also, very small, highly flexible sensor for wearable or implantable sensor application is also required. Throughout this thesis, effective solutions to solve the challenges will be discussed.

1.2. Overview of Current Technologies and Challenges

Many prior work have demonstrated methods to scavenge ambient energy source such as RF radiation energy, inductive energy, thermoelectric energy, solar energy and vibration energy [4-7]. Unfortunately, RF radiation energy has low energy efficiency in general because of the characteristics of antenna. Inductive energy has very limited link distance (usually few cm) and other systems utilize environmental energy source which is not controllable where in biomedical signal recording application, robustness and reliability is critical. Trade-off among energy harvesting techniques require a thorough investigation based on application is required.

Fig. 1.2 Battery takes up most of the size and weight of the system [8].

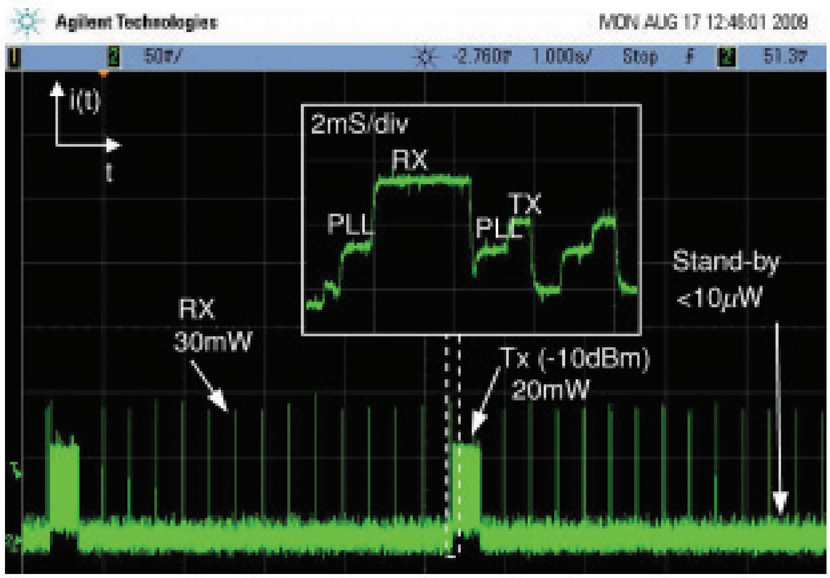

Fig. 1.3 Power consumption of a sensor node composed of commercial components [8].

In addition to the energy harvesting problem, there is a regulation on the maximum allowed RF power exposed to human body to prevent tissue heating [9], which indicates that the source of energy is limited. To extend the link distance under the limited allowed RF energy, many researchers apply aggressive duty-cycling on the system to lower the average power consumption [7]. But this is not always possible because the sensor needs to process high data rate signals (>1kHz), for instance EMG or neural signals in real-time. Thus a low power, energy efficient architecture should be used for the RF blocks. From Fig. 1.3, you can see that radio consumes most of the power consumption in conventional sensor node architecture due to its frequency synthesizers and excessive power output. This strongly suggests that we should focus on designing a power efficient radio block for sensor node network.

WSN also requires multiple sensor node operation. Conventional communication method is robust and reliable but consumes much more power which makes it very difficult for a battery-less operation. Because of this reason, research groups usually use TDMA method [10] with some sort of signal receiving mechanism, which complicates the system when sensing is the sole purpose of the device.

Lastly, research groups focus on the electronics part only and often neglect the sensing function. In many cases, the sensor is a bottleneck of the system, especially for wearable or implantable applications due to their size and flexibility.

1.3. Research Overview

To overcome the aforementioned challenges, battery-less low current active transmission schemes were proposed in [7, 11]. These devices exhibit high data-rate with low power consumption by replacing power hungry LO (local oscillator) and PLL (phase locked loop) by providing the carrier frequency for transmission through ILRO (injection locked ring oscillator). Nevertheless these devices are not suitable for TMR (targeted muscle reinnervation) application due to their lack of multi-node functionality. Battery-less low power transceivers have been proposed in [12, 13]. These devices provide higher receiver sensitivity which allows them to communicate at a further distance but at the cost of high overhead and complexity which requires heavy duty-cycling of the system to operate under practical environment. Others [10] report low current consumption sensor node with multi-node protocol. This device detects the rectified voltage with a reference to synchronize multiple nodes, thus achieving small overhead. Despite the small overhead, the available RF energy source is affected in multi-node functionality, which is undesired.

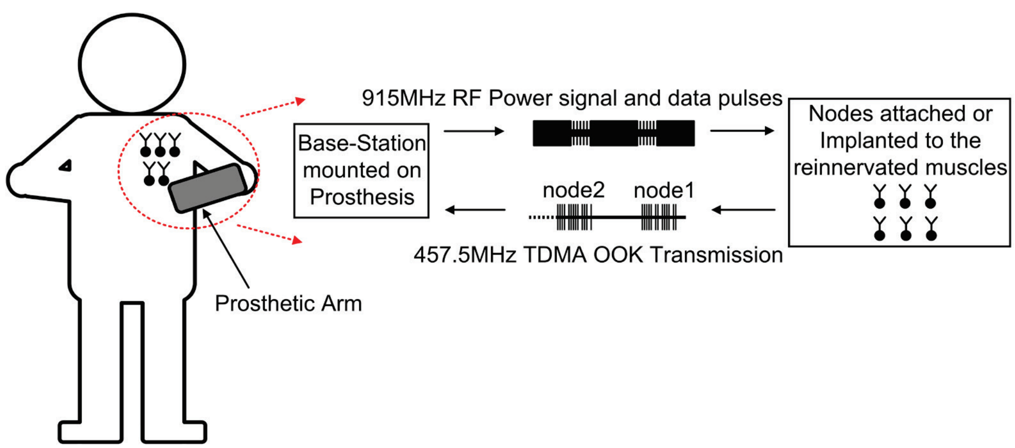

Fig. 1.4 Block diagram of harvesting and telemetry system of WSN

In chapter 2, main focus is on design and implementation of an ultra low power, wirelessly-powered RF front-end for WSN using CMOS technology. A 98μW, 457.5MHz transmitter with output radiation power of -22dBm is implemented. This transmitter uses powering RF signal. A frequency divider divides the RF signal into half to generate the carrier frequency with low power consumption. RF energy is harvested with a Cockcroft-Walton rectifier. Wireless powering RF signal is modulated in power efficient method so that the receiver recovers signal in low power operation to perform time division multiple access. A block diagram is shown in Fig. 1.2.

The communication distance for TMR and the prosthetic arm application is short (< 10cm), indicating magnetic resonance coupling (MRC) method can be more energy efficient. Using filter design topologies [14, 15], transferring power to a designated device by switching the operation frequency is possible. This technique can deliver power to multiple nodes by switching the frequency and matching network for each network. In this way, power division problem in a multi-node system can be solved with an automated impedance tuning network.

For an MRC powered device, the previous transmitter architecture has to be changed to convert a low frequency signal to a high frequency signal. Again, we want a transmitter with low power consumption and a locked frequency with low phase noise. To achieve this, an in injection locked ring oscillator with an edge combiner circuitry is introduced, designed and demonstrated with a three electrode electrochemistry sensing block.

Lastly, I fabricated a glucose sensor on carbon fibers with graphene petals. Wearable and implantable applications require devices to be freely flexible and robust while maintaining a good performance. To achieve robustness and flexibility, outer layers for glucose detection are buried between the graphene petals to fully utilize the mechanical robustness of the graphene petals.

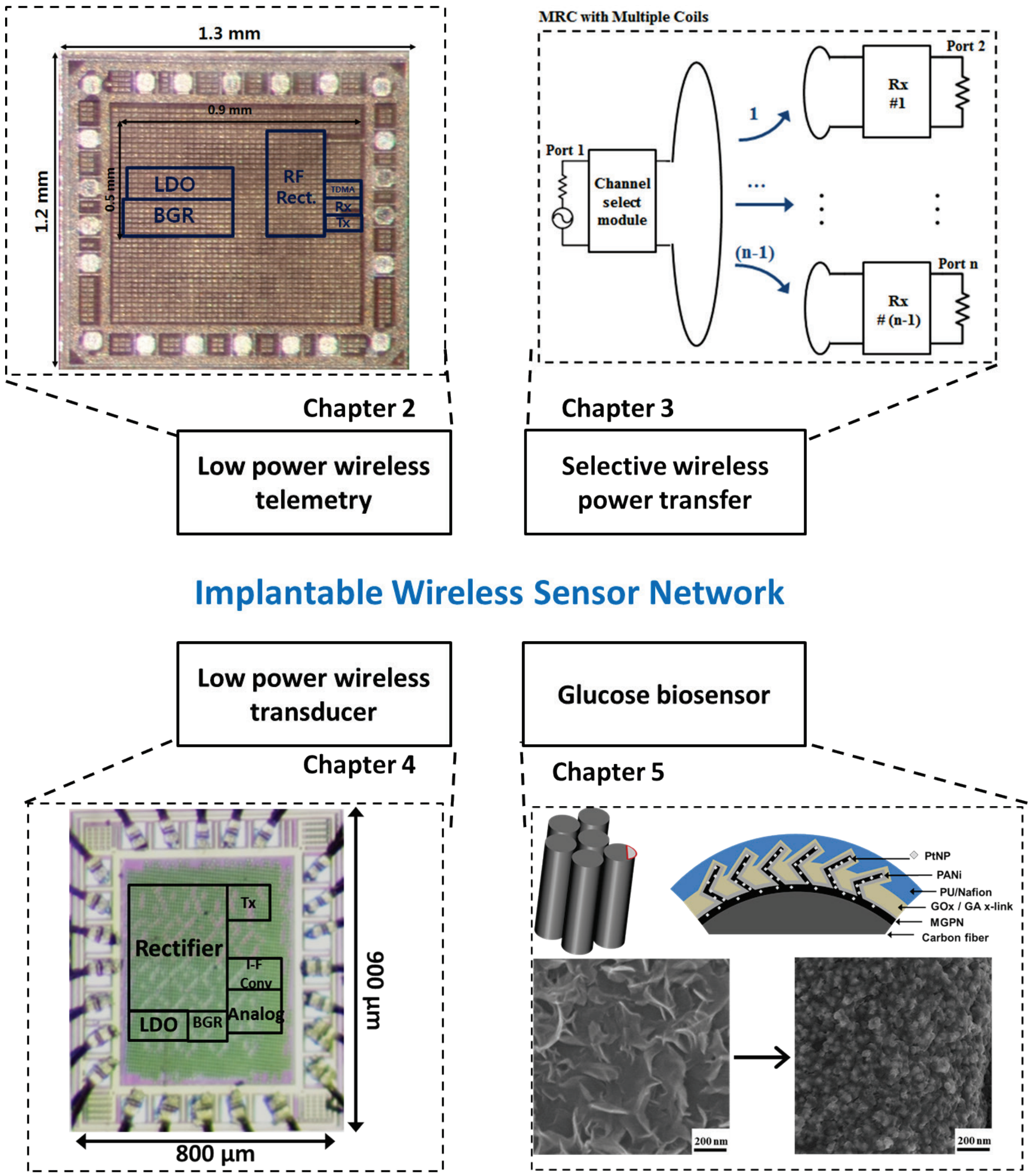

Fig. 1.5 Technology integration for wireless sensor network

To extend the application further onto more general wearable and implantable WSN, the combination of the aforementioned technologies is necessary and it will be the ultimate goal of this work. Each block is explored with depth in the following chapters. We designed and implemented an IC with low power consumption that can harvest RF energy, process sensor data and wirelessly transmit data in chapter 2 and 4. A wireless power transfer technique for adaptive distance tuning and multiple-receiver handling is developed using MRC in chapter 3. Lastly, a miniature sized sensor that can detect glucose concentration using graphene has been explored in chapter 5.

2. AN ULTRA LOW POWER, RF ENERGY HARVESTING TRANSCEIVER FOR MULTIPLE NODE SENSOR APPLICATION

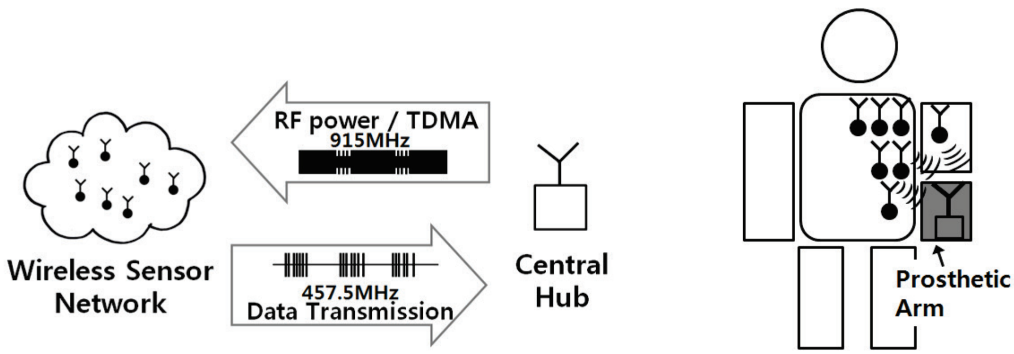

Fig. 2.1 Sensor network application

We designed and implemented an ultra low power, wirelessly-powered RF transceiver for wireless sensor network using 180 nm CMOS technology. We propose a 98 μW, 457.5 MHz transmitter with output radiation power of -22 dBm. This transmitter utilizes 915 MHz wirelessly powering RF signal by frequency division using a true-single-phase-clock (TSPC) divider to generate the carrier frequency with very low power consumption and small die area. The transmitter can support up to 5 Mbps data rate. The telemetry system uses an 8-stage Cockcroft-Walton rectifier to convert RF to DC voltage for energy harvesting. The bandgap reference and linear regulators provide stable DC voltage throughout the system. The receiver recovers data from the modulated wireless powering RF signal to perform time division multiple access (TMDA) for the multiple node system. Power consumption of the TDMA receiver is less than 15 μW. Our proposed transmitter and receiver each occupy 0.0018 mm^2 and 0.0135 mm^2 of active die area, respectively.

2.1. Introduction

Recent advances in low-power transceiver design opened up a new generation of biomedical wireless sensor network application for health monitoring and rehabilitation. But challenges still remain in realizing miniature size of the device, battery-less operation and multiple node accessibility. FCC regulation on RF exposure to human [9] places a tight constraint on delivering energy, demanding a low power device design. Also, multiple node system is required in applications such as targeted muscle reinnervation (TMR) [1, 16] but it is overlooked in many prior works due to a limited power budget.

Conventionally, the TMR sensor nodes are attached to the patient's upper chest and wired to the prosthetic arm. A major bottleneck in the current sensor technology is the use of wired sensors [17] and batteries that limit operation time. The wired surface electrodes suffer from low spatial resolution [18] and require frequent replacements. To overcome these issues, implantable devices have been developed to record the myoelectric activity [19, 20]. Since these devices are implanted, the use of batteries is not desirable because of their bulky size, and replacing a battery leads to a surgical procedure that can cause infections. To eliminate the use of battery, there are various techniques to scavenge ambient energy such as electromagnetic, inductive, thermoelectric, solar and motion energy [4-6, 19]. Unfortunately, inductive energy has very limited link distance, and delivering uniform power to multiple nodes is still a challenge [21]. Thermoelectric, solar and motion energy is not applicable in TMR and most medical implant application because such energy sources are beyond user's control. Thus, the EM energy transfer is considered in this work for its link distance and controllability.

Electromyography (EMG) data requires more than 2 kbps of sampling rate [1, 16], forcing the transmitter to be active more than other high duty-cycled sensor nodes [4, 6], which increases the required power of transmitter. To minimize the power consumption of the transmitter, some have used the passive radio frequency identification (RFID) technology for data transmission [22, 23]. However, the reader design becomes complicated because it needs to detect weak backscattered signals at the same frequency of power transmission.

Additionally, multiple node operation is another issue that arise in EMG data recording application. There are numerous multiple access techniques but due to the complexity and power consumption, TDMA is considered in this application. Multiple node operation is a problem that is overlooked in most of the literature and some overcome this by implementing a conventional receiver [4, 12, 24] or changing the strength of the powering signal [10], which leads to a significant overhead in power consumption or loss in available power.

To solve the aforementioned issues, I developed an RF energy harvesting, ultra low power, wireless telemetry system for TMR application that enables new possibilities for the upper-limb prostheses [17]. We introduce an energy-harvesting telemetry system utilizing an RF transceiver with ultra low power consumption. A TDMA logic circuit is included in the design to realize multiple node synchronization with simple and robust operation requiring very little power overhead. The proposed design also consists of an RF rectifier, bandgap reference and regulators for energy harvesting and power management.

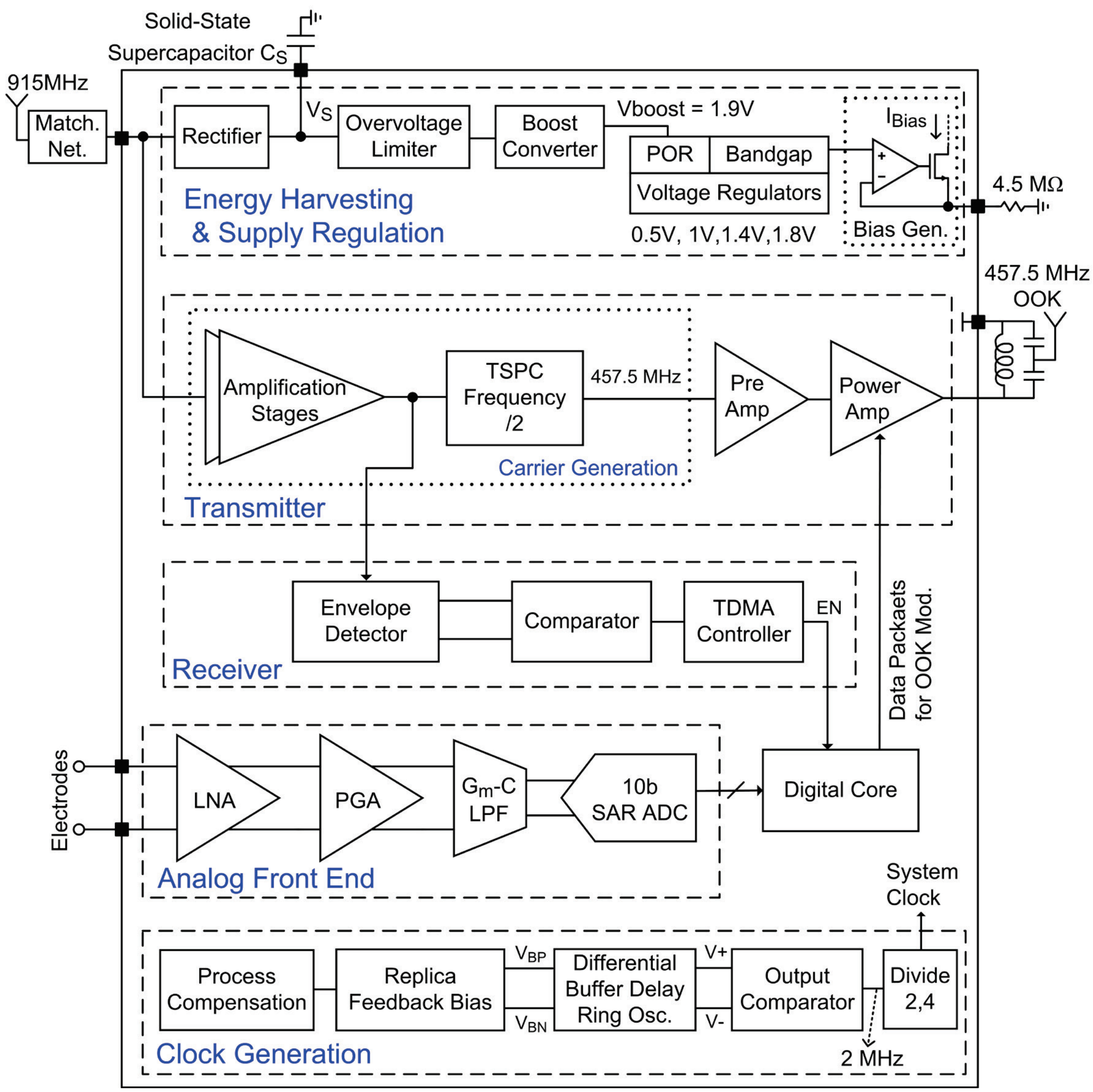

Fig. 2.2 System block diagram

2.2. Proposed architecture and circuit design

Fig. 2.2 describes the system architecture in a block diagram. The base station delivers RF energy in the ISM band (915 MHz) to the device. The RF energy has three purposes in this system; power, reference frequency and multiple node synchronization. Power is distributed to the energy harvester block where it supplies stable DC supply to the internal device. The frequency of the powering signal is taken to the transmitter where it is halved to avoid self jamming. The divided frequency is used as the transmission carrier frequency and On-Off-Keying (OOK) modulation is utilized for its simple and power efficient performance. Short off-pulses in the RF powering signal serve as the indicator for multiple node synchronization.

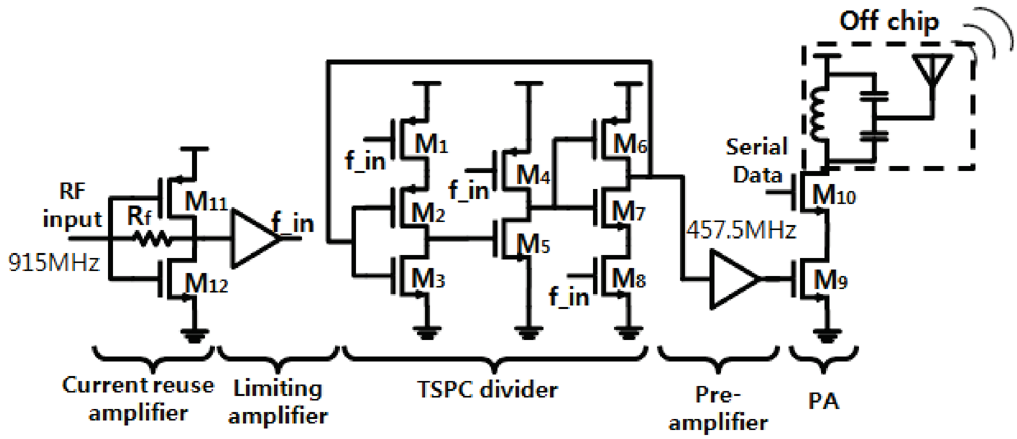

Fig. 2.3 Transmitter schematic

2.2.1. Transmitter

Fig. 2.3 shows the schematic of the proposed transmitter. The current-reused and limiting amplifier is used to convert the incident RF signal to a rail-to-rail signal for the frequency divider. A feedback shunt resistor R_f sustains the transistor in saturation and the stacked transistor structure increases transconductance for the same bias current. The size of M_{11} and M_{12} is kept small due to limited power budget and bandwidth degradation from Miller effect associated with (C_{GSN}+C_{GSP}).

Limiting amplifier is formed with a chain of minimum sized inverters. The purpose of this block is to ensure a digital-like signal and reduce the loading effect for the frequency divider to increase the robustness.

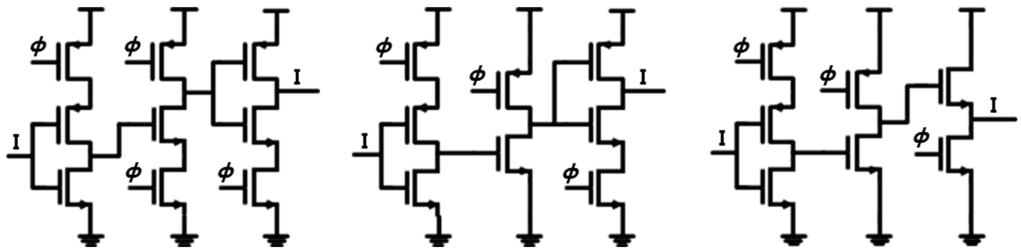

(a)

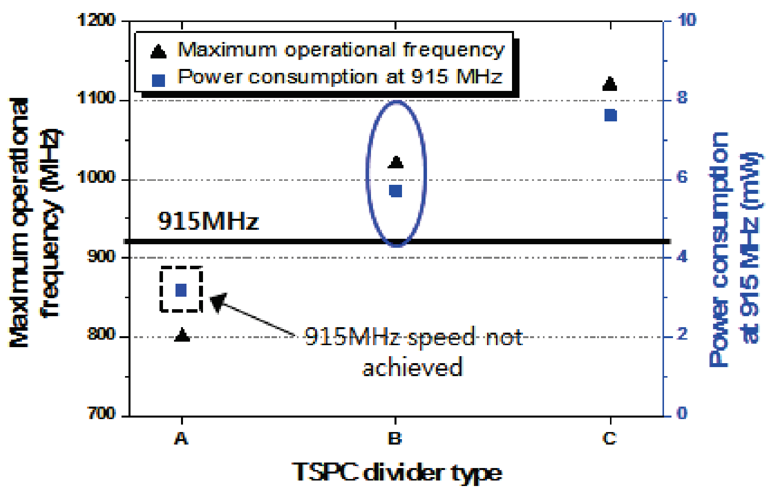

(b)

Fig. 2.4 Types of TSPC dividers (a) and simulation results of maximum achievable frequency and power consumption of the structures at 915 MHz (b).

A TSPC divider is chosen to perform the frequency division for its low power consumption at sub-GHz. Generally, in TSPC frequency dividers, ratioless logic has lower power consumption compared to ratioed logic because ideally a direct path from the supply to the ground never happens and power consumption is determined exclusively by the dynamic switching. But at the same time, ratioed logic has faster switching time with smaller gate capacitance (C_L) at the cost of robustness [25].

To minimize power consumption at a target frequency, combinations of ratioless and ratioed logics are investigated. The simulation results are shown in Fig. 4. Type A has the lowest power consumption but the speed is below our requirement under the reduced power supply and load introduced by subsequent blocks. Thus type B is chosen for the lowest power consumption. High-V_t devices were used for the TSPC divider to reduce the leakage current.

A power efficient switching amplifier is used for the power amplifier (PA). For power reduction, a DC voltage of 0.5 V supplies the amplifier. The matching network is implemented with off-chip components. Because the capacitors have higher Q-factor compared to inductors, a tapped-capacitor network has been used to avoid inductors.

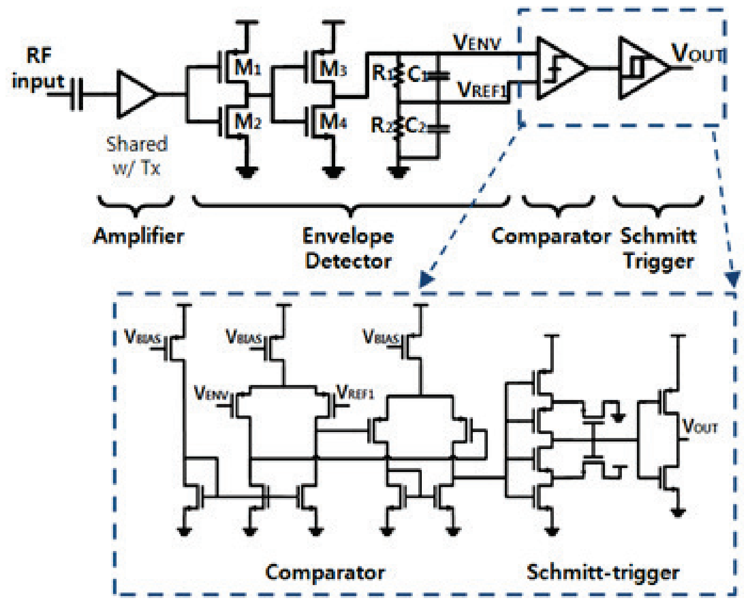

Fig. 2.5 Receiver schematic.

2.2.2. Receiver

The receiver (Fig. 2.5) is designed to detect very short off-pulses of the RF power source with small power consumption because modulation in the RF power source can be considered as an overhead in total available power. The amplifier stage is implemented on-chip that is the same amplifier stage shared with the transmitter to reduce power consumption. The off-pulses are demodulated by using an envelope detector which is composed of inverters driving two different RC time constants; one serving as the envelope detector (V_{ENV}) and the other one with a long time constant to give an average of the envelope (V_{REF1}).

A comparator then digitizes the voltage levels of the two RC circuits for demodulation. The comparator is formed of two differential amplifier pairs with input-referred offset voltage simulated to be less than 10 mV. A Schmitt-trigger inverter stage is cascaded to the comparator to ensure a reliable rail-to-rail digital signal is present at the output.

From the demodulated data, a TDMA logic circuit performs the node synchronization. The transient measurement shown in Fig. 10 explains the operation. When five RF off-pulses are detected within 8 μs of time period, an 'event' is triggered. By counting the number of 'events', a 'node enable' signal is presented when the event counter matches a pre-programmed number in each device. Each device node also has a pre-programmed cycle number where the 'event' counter resets. Maximum number of nodes for synchronization is defined by the number of bits assigned for the pre-programmed number, which is 16 in this design.

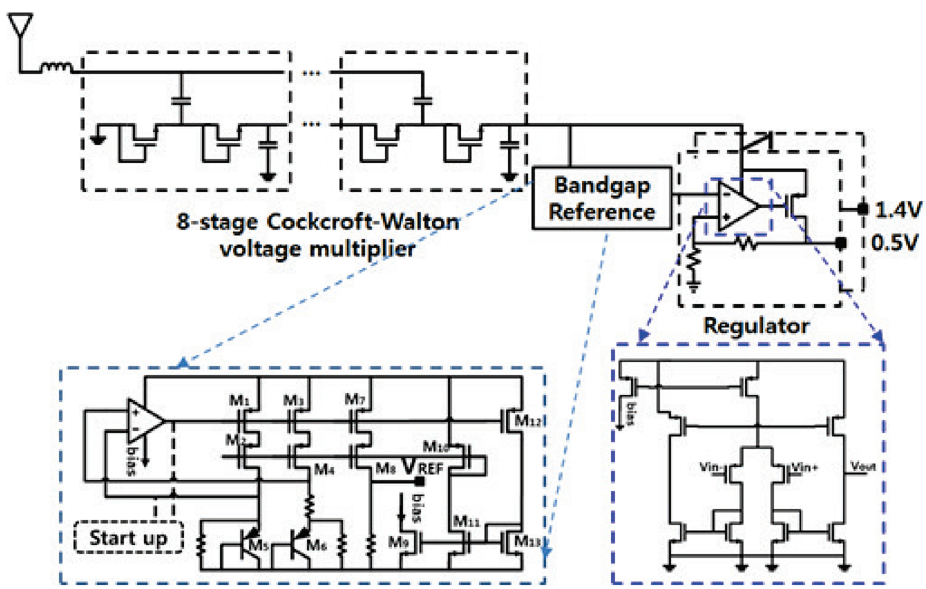

Fig. 2.6. Schematic of the energy harvester and power management

2.2.3. Energy harvester and power management

The RF energy harvester block (Fig. 2.6) is comprised of an RF rectifier, bandgap reference and low dropout (LDO) regulator. An 8-stage Cockcroft-Walton voltage multiplier rectifies and boosts the voltage to a sufficient level with low input signal [26]. Native devices were used in this design for their low voltage drop and tolerable back leakage.

We employed two LDO regulators to supply the PA and elsewhere. An off-chip capacitor of 4.7 μF with effective series resistance (ESR) of 1 Ω is used for stability. The line regulation is measured within 0.1% of its nominal values.

The bandgap reference generates a process, voltage and temperature independent reference for the system [27]. The PMOS current sources of the BGR are cascoded to improve the power-supply- rejection-ratio (PSRR).

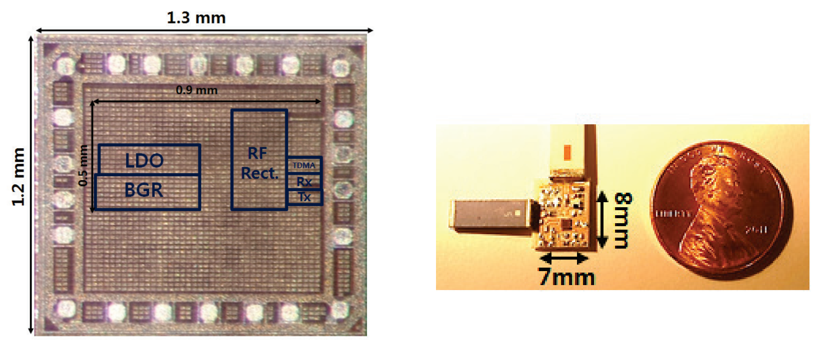

(a) (b)

Fig. 2.7. (a) Die micrograph; (b) Chip assembled example

2.3. Experimental results

The ASIC was fabricated through 180 nm CMOS process technology (Fig. 2.7(a)). The total area of the test-structure including the pads is 1.3 mm × 0.7 mm. The assembled transceiver is shown in Fig. 2.7(b).

Off-chip SMD components were used to implement the matching network for the transmitter. The power consumption for the transmitter is measured to be 98 μW while delivering -22 dBm (Agilent E4404B) to the load (Fig. 2.8(b)) and Table I shows the detailed power consumption breakdown. The minimum power required for the input to generate a stable 457.5 MHz carrier is -10 dBm and the maximum data rate of the transmitter is 5 Mbps, 15 pJ/b. The startup time of the transmitter is 60 ns, which is fast enough for the proposed receiver and TDMA method. The transmitter occupies die area of 0.0018 mm^2.

Table. 2.1 Power consumption breakdown for transmitter

Transmitter Block	Power Consumption
Current-reused amplifier	25µW
Limiting amplifier	
TSPC divider	11µW
Pre-amplifier	13µW
PA (Tx out: -22dBm)	49µW
Total power	98µW

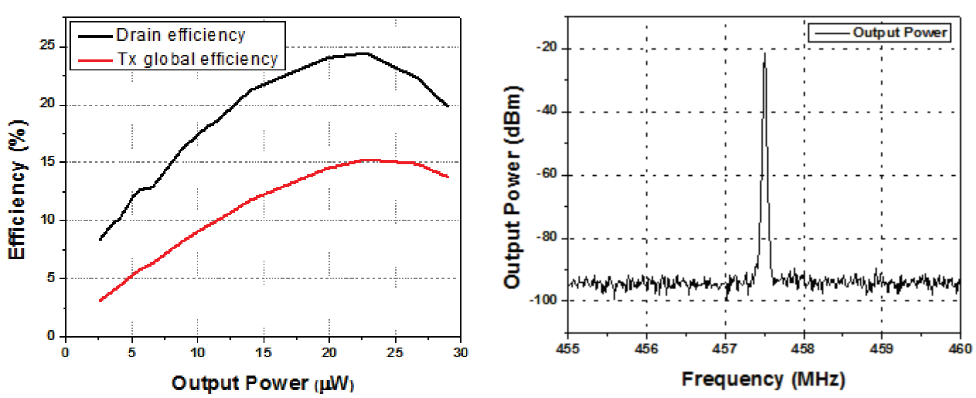

(a) (b)

Fig. 2.8. (a) Measured transmitter efficiency; (b) Measured transmitter output spectrum

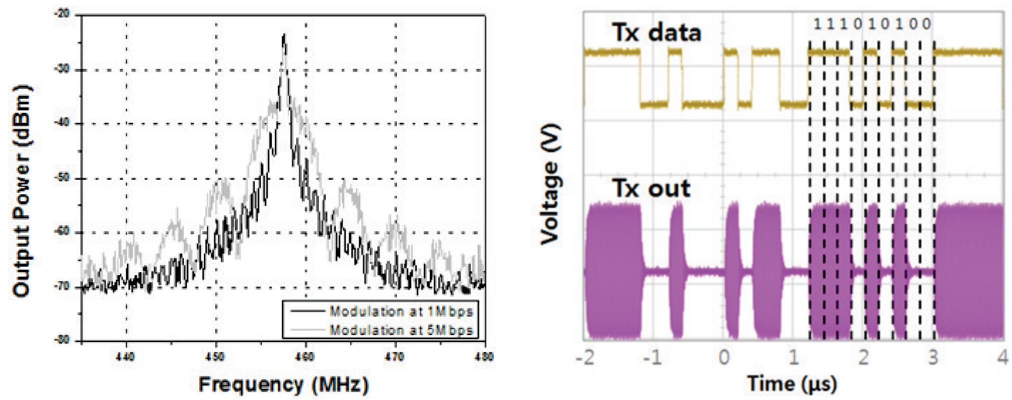

(a) (b)

Fig. 2.9. (a) Spectrum measured with modulated input at 1 and 5 Mbps; (b) Transient waveform of the transmitter with pseudorandom input at 5 Mbps.

The receiver shows sensitivity of -10 dBm with power consumption less than 10 µW. The overall power consumption of the TDMA logic circuit consumes 5 µW. The receiver can detect pulses as short as 0.5 µs in the current TDMA operation mode, giving efficiency of 5 pJ/b. Fig. 10 displays the measured TDMA operation. A waveform generator is used to create the trigger pulses for the RF signal generator. To make sure the receiver and the digital block detects an "event", the input RF signal is configured to have 7 off-pulses in 8 µs period. The measurement was taken on a four node system with three nodes measured due to the limited number of probes in the oscilloscope. It can be seen that the "node enable" signal rises after 5 off-pulses. In this measurement example, the penalty on the total available power caused by modulating the RF powering signal is less than 7% which is much lower than other reported work [10]. The entire receiver including the logic circuits occupy 0.0135 mm^2 of chip area.

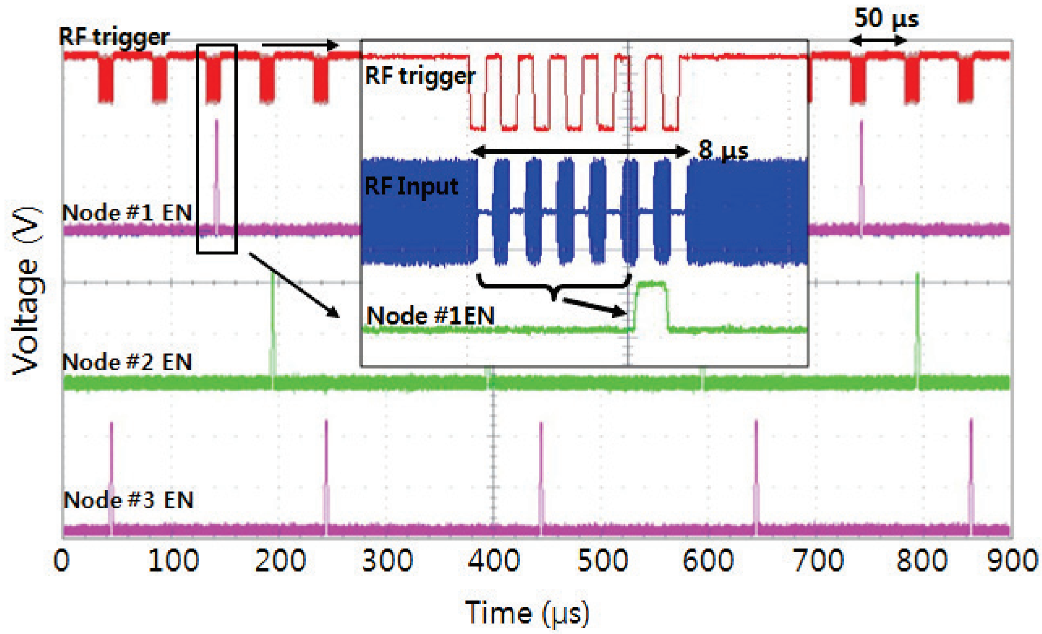

Fig. 2.10. Transient waveform of the RF input and TDMA operation

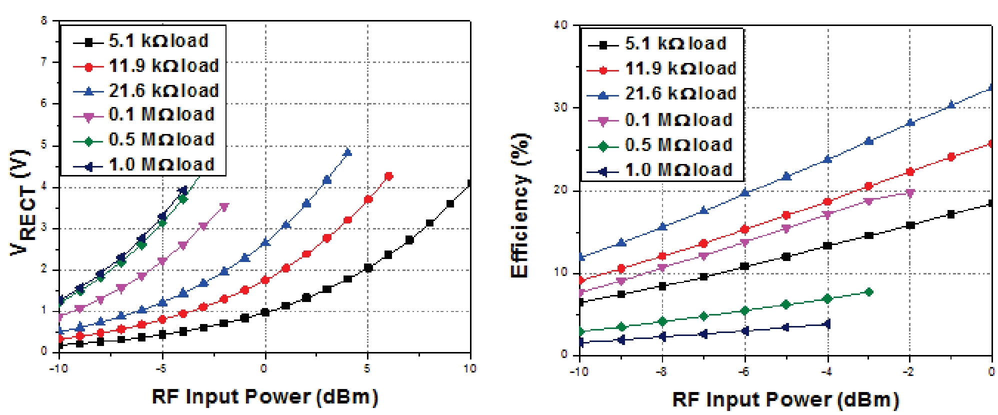

(a) (b)

Fig. 2.11. Measurement of (a) V_{RECT} and (b) efficiency respect to input power under various load conditions.

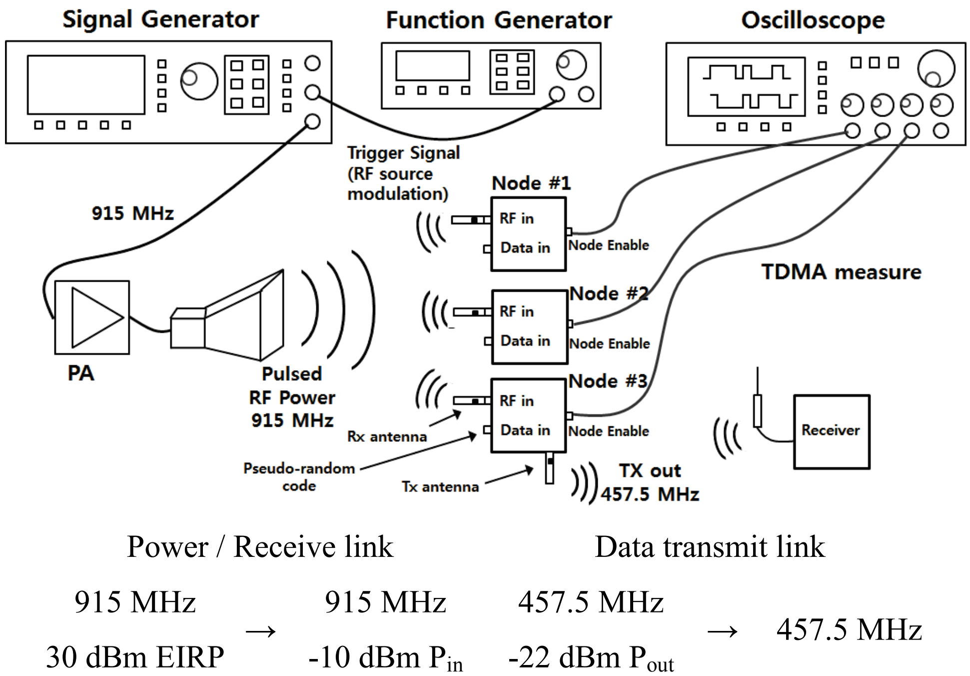

Fig. 2.12. Experiment setup.

Fig. 2.11 shows voltage measurement at the rectifier under different load conditions. External resistance represents the various loading of the system. The diode connected transistors in the rectifier has a nonlinear behavior and it is difficult to optimize the matching network at a wide load range. Thus, a specific load condition that would represent a clinical application is chosen [28]. The overall energy efficiency is over 10% throughout the input power range. The total current consumption of the bandgap reference and voltage regulator is 3μA.

The functionality of the energy harvest, node synchronization and data transmission was verified under the experimental setup shown in Fig. 12. The experiment was performed in a laboratory environment.

The RF energy is delivered by using a signal generator, external PA and a horn antenna. Commercial whip antenna (ANT-916-CW-RCS, Linx Tech) and chip antenna (ANT1204LL05R0915A, Yageo) were used for receiving power where the TDMA synchronization operates flawlessly up to 2.8 m and 2.2 m, respectively. Three transceiver nodes were used at the same time for TDMA verification. Transmitter was tested under the same environment with a commercial chip antenna (7488910043, Wurth Elec). Data input pin is connected to a pseudorandom code generator to and the external base station receives and demodulates the signal. The data rate was tested up to 1 Mbps due to the limitation on the base station. (USRP N210, Ettus) The bit error rate (BER) is measured to be below 0.1% up to 6 m.

For in-vivo experiments, [29] provides an estimation on how much RF energy can be received in an implant. It is shown that when the transceiver is placed between the adipose and muscle, the maximum achievable distance between the transceiver and the base station can be estimated to be more than 30 cm.

Table II summarizes the performance of the proposed transceiver with few works that have recently been published. At -10 dBm input power, the transceiver consumes 110 μW while constantly delivering Pout of -22 dBm to the transmit antenna.

Table. 2.2 Performance comparison of the proposed transceiver and current technology

Reference		This work	[15] '14 JSSC	[14] '14 JSSC	[23] '11 RFIC	[24] '10 ISSCC	[25] '14 TCAS2
CMOS Technology		180 nm	65 nm	90 nm	130 nm	130 nm	180 nm
Energy Harvest		✓	✓	✓	✓	✓	×
RX Frequency		915 MHz	904.5 MHz	915 MHz	×	×	×
TX Frequency		457.5 MHz	402 MHz	2.44 GHz	306 MHz	2.4 GHz	UWB<1GHz
TX Pout		-22 dBm	-18~ -16 dBm	-12.5 dBm	-33 dBm	-45 dBm	0.75Vp-p
Multi-node		✓	✓	✓	×	×	×
Pwr Cons.	E. Harvest.	3 μA	< 1 μA	100 μA	N/A	21.35 μA	×
	Tx (100% on)	98 μW	215 μW	380 μW	50.6 μW	1.15 mW	175 μW
	Rx	<15 μW	13 μW	480 μW	×	×	×

2.4. Full system

The full system that is composed of the transceiver described in this chapter is described in a table. Also a comparison table with the state-of-the-art wireless body sensor network (WBSN) is presented.

Table. 2.3 Measured performance summary of the full system

Supercapacitive RF Energy Harvesting		AFE (LNA, PGA, G_m-C)		AFE - SAR ADC		Clock		TX and RX	
V_S	<0.8V	Supply	1.8V	Supply	1, 1.8V	Supply	1.8V	Supply	0.5,1,1.4V
V_{BOOST}	1.9V	Current	4μA	Current	0.29μA	Current	4.2μA	TX Current	53.6μA
Boost Efficiency	64%	Gain	43–58dB	V_{REF}	1V	Process variation	±2.93%	TX Output Power	- 22dBm
Switching Frequency	1MHz	f_C (High -pass)	0.65-3Hz	Sampling Rate	41.6KS/s	supply variation	0.11%	TX Frequency	457.5MHz
$I_{quiescent}$ for Regulators	0.4 μA	f_C (Low -pass	1KHz	DNL/INL	0.69/1.14 LSB	Core Frequency	2.02 MHz	Data Rate	1Mbps - Burst
$I_{quiescent}$ for Bandgap and Bias Gen.	1.8μA	$V_{irn,rms}$	< 4 μV_{rms} (4Hz-1KHz)	ENOB	9.1bits @ 1KHz			Sensitivity	-10dBm
		THD (Gm-C)	< -56.5dB	FOM	14.3 fJ/step			Modulation	OOK
System Current		12.5μA (total average), 74μA (peak)						RX Current	5.3μA
System Power		24μW (total average),141μW (peak)						RX Frequency	915MHz

Table. 2.4 Performance comparison with the state-of-the-art WBSNs

		This Work	[7]	[9]	[8]	[24]
Supply Voltage		1.8V, 1V - AFE 1.4V, 0.5V - TX 1.4V, 1V - RX 1V – Digital,TX	1.2V - AFE, 1V, 0.5V- TX 0.5V - DSP	0.9V - AFE 0.56V - TX	1V	N/A
Energy Harvesting Source		RF	Thermal, RF	RF	RF	RF
Energy Harvesting Frequency		915MHz	×	904.5MHz	915MHz	300MHz
Sensitivity		-10dBm	30mV,-10dBm	-20dBm	-17.1dBm	N/A
Sensor		EMG	ECG	Off-chip bio-sensor	×	ECoG
Multi Node		✓	×	✓	✓	×
Crystal Oscillator		No	Two	No	No	No
RX Frequency		915MHz	×	904.5MHz	902-928MHz	×
TX Frequency		457.5MHz	402/433MHz	402MHz	2.405-2.475 GHz	300MHz
TX P_{out}		-22dBm	-18.5dBm	-18~ -16dBm	-12.5dBm	N/A
TX Data Rate		1 Mbps	200 kbps	250 kbps	5 Mbps	1 Mbps
Uplink Modulation		OOK	BFSK	OOK	OOK	Backscatter
Downlink Modulation		OOK	×	ASK	FSK	×
Power	AFE	7.5μW	4.8μW	3.6μW*	×	147.2μW**
	TX (100% On)	66μW	160μW	215μW	380μW	2.4μW
	RX	7μW	×	13μW	480μW	×
	Total Power	24μW	19μW‡, 397μW†	N/A	960μW	225μW
CMOS Technology		0.18μm	0.13μm	65nm	90nm	65nm
Chip Area		1.35×1.5mm^2	2.5×3.3mm^2	1×2mm^2	1.4×1.1mm^2	2.4×2.4mm^2

*Off-chip bio-sensor, **64 Channels, ‡R-R and AFib ECG modes and TX is duty cycled at 0.013%
†Raw data mode for continuous data acquisition

2.5. Conclusion

We present a low-power wireless telemetry system, powered by an RF energy harvester, for a multiple node targeted muscle reinnervation sensor application. The transmitter is designed to have a low-power consumption for a battery-less sensor application. The overall system has a stable carrier frequency, high data rate for transmission and robust TDMA performance while consuming only 110 μW, which is the lowest power level for an active multiple node telemetry system that has been reported to date. Based on the proposed power transceiver, a sensor node can be designed with low power consumption [30].

For future improvement, antenna decoupling technique [31] can be included to reduce the system size. The sensitivity of the receiver can be improved by adding a separate gain stage or method introduced in [23].

3. MULTIPLE NODE WIRELESS POWER TRANSFER AND MULTIPLE ACCESS CONTROL TECHNIQUE

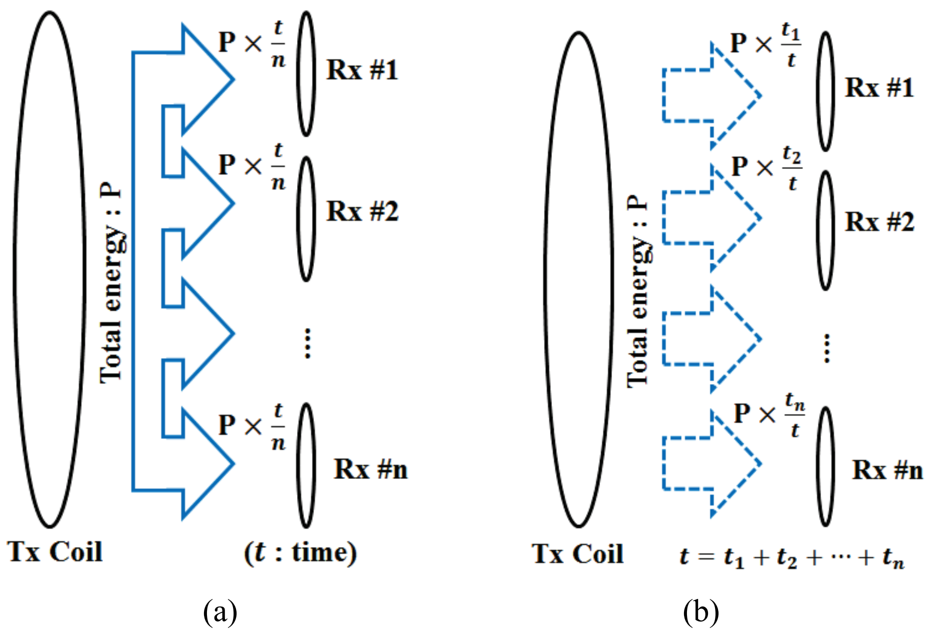

Fig. 3.1. Power distribution in multiple node system. (a) A conventional simultaneous WPT with multiple receivers. (b) Selective WPT with multiple receivers, assuming uniform coupling in both cases.

In a multiple-receiver wireless power transfer (WPT) system, determining the condition for uniform power distribution at a maximum efficiency is a challenging issue. In this paper, a selective wireless power transfer technique using magnetic resonant coupling (MRC) is introduced for smart power delivery in a multiple-receiver system. The proposed method selectively and exclusively delivers power to only one designated receiver among multiple receivers, eliminating the cross-coupling effect and unbalanced power division problem across the receivers. This is achieved by separating the resonant frequencies of the receivers to isolate the coupling effects between coils. The power division ratio of the receivers is controlled by changing the duration time ratio for power transfer. In this work, a one-transmitter, three-receiver, selective MRC system is designed and fabricated. The power distribution is demonstrated under perfectly matched condition, showing power transfer efficiency (PTE) of 24~29% at a very small coupling coefficient of 0.01 with a 12 mm-diameter receiver coil. Distance compensation and a one way communication of time-division multiple access (TDMA) is demonstrated for a multiple-receiver system, using the proposed method.

3.1. Introduction

Portable electronic device charging via wireless power transfer is an emerging technology that enables applications such as smart healthcare, home and office devices [1, 32]. Based on the advances in microelectronics technology, the size of such devices is shrinking so drastically that they are now becoming wearable and even implantable [33, 34]. At the same time, these portable devices are commonly available around everyday life that allow the user to play music, monitor vital signals, and wirelessly communicate. In order to deliver power to ubiquitously existent miniature devices, miniature and multiple-receiver WPT techniques have been previously explored [3, 15, 35] using magnetic resonance coupling [32, 36].

Current WPT techniques for multiple receivers focus on delivering power simultaneously to all of the devices in the system [15, 37, 38] as shown in Fig. 3.1(a). But in applications such as wearable or implantable devices, where spatial freedom is required, simultaneous power delivery system has a problem in distributing uniform power to the receivers. In a non-stationary environment, the receiver that has a stronger coupling strength to the transmitter has dominant influence to the system, resulting to an unbalanced power distribution. Power division issue was addressed in [21], but precise control of division ratio still remains as an issue and it is not suitable for wearable or portable application because the configuration requires a repeater to pair with any additional receiver and a large inductance tuning is also needed in the receiver device, which requires considerable space. [39] makes another approach, but the system is limited to two receivers.

Another issue in a simultaneously powered multiple-receiver system comes from the fact that portable electronic devices often requires spatial freedom, and it is extremely difficult to find a maximum power transfer condition for multiple receivers in an environment with variable distance [37]. There is abundant literature on methods to compensate for change of location in a single-receiver system [40, 41], but these solutions cannot be applied to systems with multiple receivers under simultaneous power transfer scenario.

To overcome the aforementioned problems in the current multiple-receiver WPT system for miniature electronic device charging application, we propose a selective WPT technique using bandpass filter theory and MRC (resonantly coupled filter energy transfer) [15, 42]. The WPT system is modeled with distinct resonant frequencies for the receivers that form passbands at separate center frequency as shown in Fig. 3.2(c). By selecting the corresponding source frequency and impedance values for the transmitter, only one energy link is active at a time. In other words, among multiple receivers, only one receiver is powered at a time.

This method can resolve the power division issue by closely controlling the time duration of the power being transferred to each receiver (Fig. 3.1(b)). Additionally, in a battery charging application, the selectiveness presents an extra efficiency to the system since any effort towards a fully charged device can be prevented by selectively not transferring power to that particular receiver.

Secondly, the proposed selective WPT using filter theory is advantageous in achieving the maximum power transfer efficiency for multiple receivers. Because the resonant frequencies of the receivers are distinct and only one receiver is powered at a time, at its unique frequency, the cross-coupling effect between the receiver being powered and the others have negligible influence to the main power transfer link. This fact implies that the impedance tuning method to compensate for change of position can be applied in a multiple-receiver system, which ensures that maximum power transfer efficiency can be achieved in a dynamic environment.

Additionally, the proposed selective WPT method can be used in a TDMA, multiple-receiver system where the power receiver acts as a node. To reduce the power consumption and system complexity of a wireless sensor network (WSN) device, TDMA is widely used for its simple mechanism [10, 12, 43, 44]. Since power reduction is one of the critical requirements in biomedical sensor application, most of the state-of-the-art sensor devices communicate at a single frequency [10, 43, 44]. But in order to implement TDMA in a multiple-node system, a synchronization signal must be present at each node that defines the timeslot for its data transmission. Some research groups achieve synchronization by using a conventional RF wireless receiver, which draws significant power [12, 43]. Others try to solve the multiple access issue by modulating the wireless power transfer source, which depreciates the total available power [10]. In comparison with the previously reported work, frequency-selective WPT permits maximal power transfer to multiple loads by time multiplexing and at the same time it could be used as a synchronization signal, defining the timeslots for each node that can enable a one-way TDMA communication. No additional circuit is needed because the presence of the wireless power source can be detected from the energy harvesting unit, which is an essential part of WPT.

In this work, we present a selective WPT design using a resonator-coupled 2-pole BPF model [45]. The center frequency is predetermined and the bandwidth is decided by the filter theory. The passband for the selective WPT is made sure that power isolation between the receivers is guaranteed, as shown in Fig. 3.2(c). The design starts from a single receiver system and extends to a multiple receiver system. Relay switches were used in the transmitter to implement the dynamic capacitance for selective power transfer and compensation for distance variation. S-parameter measurements were taken by using a vector network analyzer (VNA) and power measurement by a signal analyzer in a 50 Ω load. Compensation for distance variation is demonstrated by controlling the dynamic capacitance. Then a simple passive rectifier using discrete schottky diodes is integrated with the selective WPT system to show the power distribution in a multiple-receiver system. Demonstration of the TDMA is performed by using three wireless transceivers and a base station. For a biomedical application, a SAR field simulation is included.

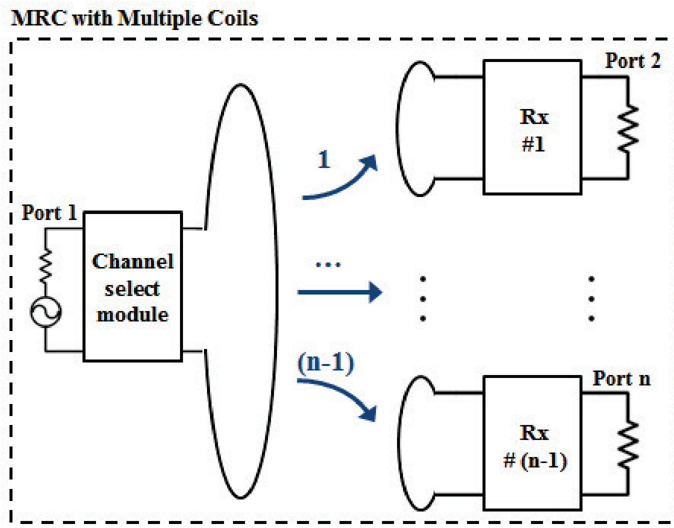

(a)

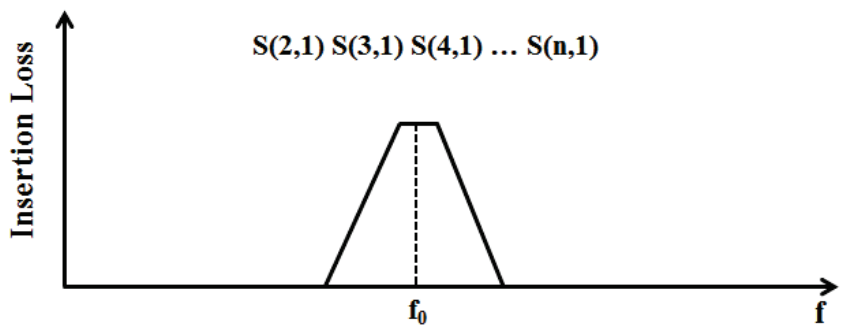

(b)

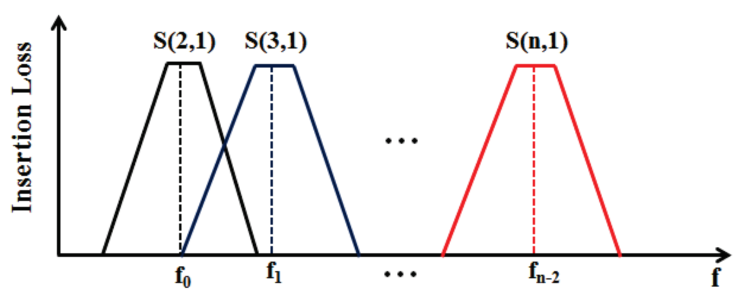

(c)

Fig. 3.2. MRC with multiple receivers. (a) Block diagram of the MRC with multiple receivers. (b) Frequency response of the conventional single frequency, simultaneously powered multiple-receiver WPT. (c) Frequency response of the proposed selective WPT

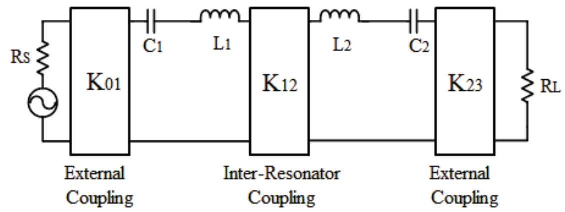

(a)

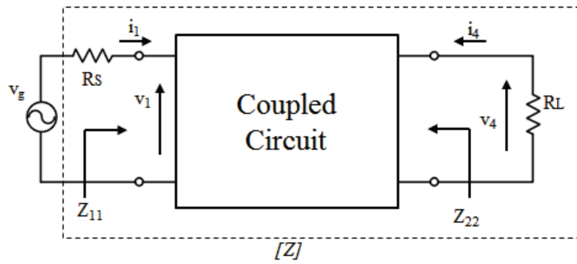

(b)

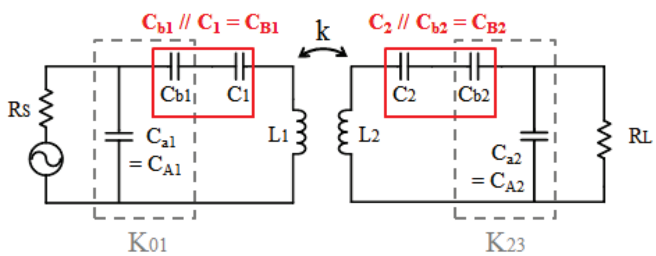

(c)

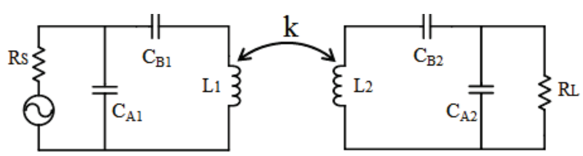

(d)

Fig. 3.3. MRC schematic. (a) The 2-pole BPF model. (b) Impedance matrix of the resonator circuit. (c) Substitute impedance inverters with capacitors and combine series capacitance. (d) Final design.

3.2. Design of a selective MRC system

This section covers the design of the selective MRC system in detail. It covers the bandpass filter model used in the selective MRC design. The design starts with a 50 Ω-load MRC system with a single receiver. Then the design extends to a three-receiver system and an adaptive distance tuning is considered for a dynamic environment.

3.2.1. MRC System Design Based on a BPF theory

The resonator-coupled 2-pole BPF is used as an equivalent circuit to model the MRC system as shown in Fig. 3.3. In characterizing the filter model, an (n+2) coupling matrix [M] can be used as shown in (3.5) [14, 46-48], where the elements are normalized coupling coefficients. M_{01}, M_{23}, and M_{12} represents the external coupling to the source, external coupling to the load and inter-resonator coupling, respectively. The source and load terminations (R_s, R_L) are normalized to unity impedance.

In this particular system, small and thin coils are used for the receivers. Additionally, this work does not include any techniques to enhance the Q-factor for general demonstration. Thus, the coils suffer from limited Q-factors that are far from being ideal. So the effect of a non-infinite resonator unloaded Q-factor is included in the calculation by giving an offset δ_i as shown in (3.6)-(3.8) [14] where Q_1 and Q_2 denote Q of L_1 and L_2, respectively. M_{12} is decided by the 2nd order element values for the low-pass filter prototypes (g_n) [47], where in this example, Butterworth prototype was used for its low insertion loss characteristic (g_1= g_2=1.4142).

$$M_{12} = \frac{1}{\sqrt{g_1 g_2}} \tag{3.1}$$

$$k = M_{12} FBW \tag{3.2}$$

$$FBW = \frac{w_2 - w_1}{w_0} \tag{3.3}$$

$$f_0 = \frac{w_0}{2\pi} = \frac{1}{2\pi\sqrt{L_1 C_1}} = \frac{1}{2\pi\sqrt{L_2 C_2}} \tag{3.4}$$

Physical dimensions of the coils determine the coupling coefficient (k) which relates to M12 and fractional bandwidth (FBW) shown in (3.2)-(3.3), where ω_2 and ω_1 are the upper and lower band-edge frequencies, respectively. In this design, the dimension of the coils is decided by considering a portable electronic device charging scenario. A 2-turn, 56 mm-diameter coil is used for the transmitter (Tx) coil and a 5-turn, 12 mm-diameter for the receiver (Rx) coil. The vertical distance from the Tx coil to the Rx coil is set to be 40 mm so that higher power transfer is guaranteed at a closer location. The horizontal distance from the center of the Rx coil to the center of the Tx coil is 15 mm (k=0.01). The electrical parameters of the coils are listed in Section III. The center frequency (f_0) of the resonator is decided by finding the maximum Q of the coils, where in this example, 22.5 MHz is selected.

The response of the BPF is characterized by the impedance matrix, *[Z]*. The diagonal entries of *[R]* and *[U]* indicate the existence of loads and resonators, respectively.

$$[Z] = [R] + [U] + j[M] \tag{3.5}$$

$$[M] = \begin{bmatrix} 0 & M_{01} & 0 & 0 \\ M_{01} & 0 & M_{12} & 0 \\ 0 & M_{12} & 0 & M_{23} \\ 0 & 0 & M_{23} & 0 \end{bmatrix} \tag{3.6}$$

$$[R] = \begin{bmatrix} 1 & 0 & 0 & 0 \\ 0 & 0 & 0 & 0 \\ 0 & 0 & 0 & 0 \\ 0 & 0 & 0 & 1 \end{bmatrix}, \; [U] = \begin{bmatrix} 0 & 0 & 0 & 0 \\ 0 & s+\delta_1 & 0 & 0 \\ 0 & 0 & s+\delta_2 & 0 \\ 0 & 0 & 0 & 0 \end{bmatrix} \tag{3.7}$$

$$s = \frac{j}{FBW}\left(\frac{w}{w_0} - \frac{w_0}{w}\right) \tag{3.8}$$

$$\delta_i = \frac{-j}{Q_i FBW} \tag{3.9}$$

The derivation process extremely simplifies if we constrict the frequency to f_0 as it would terminate (3.8) to zero. As it is shown in Fig. 3.3(b), all the voltage (v_n) and current (i_n) elements in the source, load and resonators can be derived from [z] and source voltage, v_g, by (3.10)-(3.11). The derivations are quite simplified since the source and load are normalized to unit impedance. The reflection coefficient S_{11} and transmission coefficient S_{21} at the center frequency can be obtained by (3.12)-(3.13) [14].

$$\begin{bmatrix} v_g \\ 0 \\ 0 \\ 0 \end{bmatrix} = [Z] \begin{bmatrix} i_0 \\ i_1 \\ i_2 \\ i_3 \end{bmatrix} \tag{3.10}$$

$$v_n = 1 \times i_n = [Z]_{n,1}^{-1} \times v_g \tag{3.11}$$

$$S_{11} = 1 - 2Z_{1,1}^{-1} \tag{3.12}$$

$$S_{21} = 2Z_{4,1}^{-1} \tag{3.13}$$

Similarly, the power transmission and reflection ratios are defined by η_{21} and η_{11} as following.

$$\eta_{11} = |S_{11}|^2 \times 100 \tag{3.14}$$

$$\eta_{21} = |S_{21}|^2 \times 100 \tag{3.15}$$

Using the impedance matrix and the power transmission ratios, we can find the condition of M01 and M23 that maximizes the power transfer. From the coupling values, the impedance inverters (K_{01}, K_{13}, K_{23}) in Fig. 3.3(a) can be solved by (3.16)-(3.18) [14, 47, 48]. The normalized source and load impedances are restored back to 50 **Ω**.

$$K_{01} = M_{01}\sqrt{50L_1 2\pi f_0 FBW} \tag{3.16}$$

$$K_{23} = M_{23}\sqrt{50L_2 2\pi f_0 FBW} \tag{3.17}$$

$$K_{12} = M_{12} 2\pi f_0 FBW\sqrt{50L_1L_2} \tag{3.18}$$

The impedance inverters are realized by lumped elements C_a and C_b, as displayed in Fig. 3.3(c). Capacitors are chosen for their low series resistance and easier tuning mechanism compared to [21] where inductor is lossy and difficult to tune. The values are calculated as (3.19)-(3.20), where K_{ex} represents K_{01} for source and K_{23} for load.

$$C_a = \frac{\sqrt{50^2 - K_{ex}^2}}{2\pi f_0 50 K_{ex}} \tag{3.19}$$

$$C_b = -\frac{1 + (2\pi f_0 C_a 50)^2}{(2\pi f_0)^2 C_a 50^2} \tag{3.20}$$

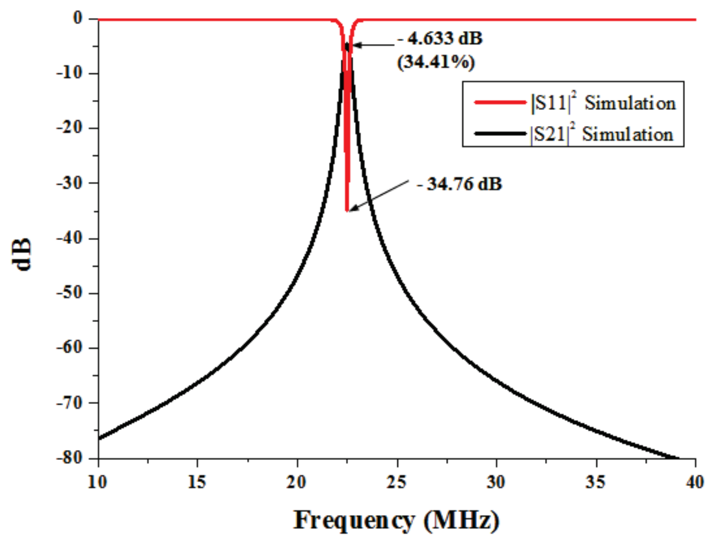

Fig. 3.4. Calculated frequency response of a single-Tx, single-Rx MRC system (f0 = 22.5 MHz).

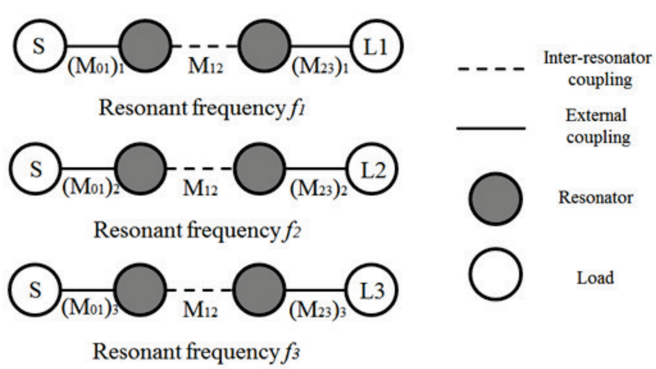

Fig. 3.5. Resonantly coupled BPF model for three resonant frequencies in a three receiver WPT system

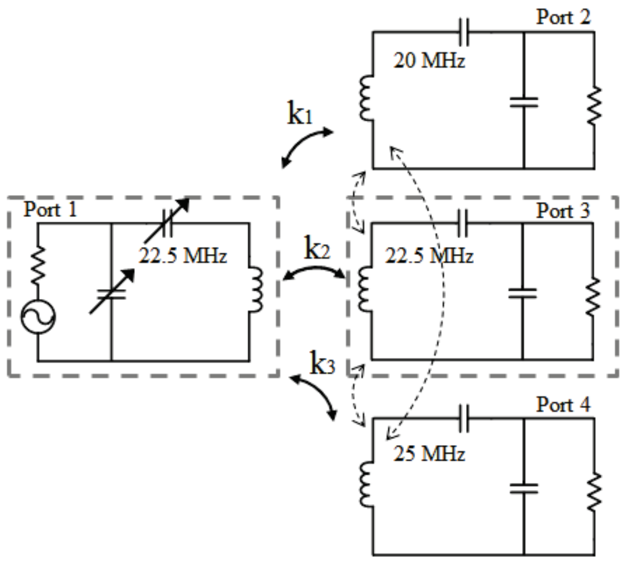

Fig. 3.6. Circuit diagram of the selective MRC in a three-receiver system with the Tx tuned at 22.5 MHz.

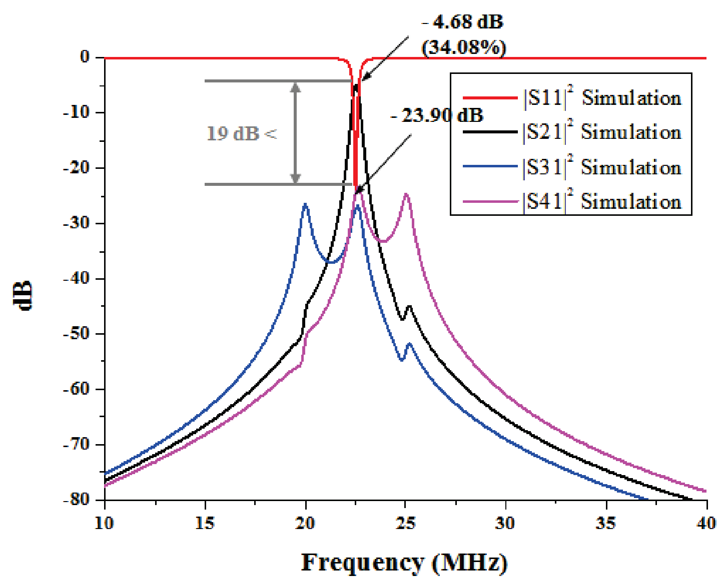

Fig. 3.7. Calculated frequency response of a three-receiver system with the Tx tuned at 22.5 MHz. The receivers are designed at 20, 22.5 and 25 MHz.

Based on the design method, the frequency response of the BPF model can be obtained as Fig. 3.4. The S_{21} at f_0 can represent the theoretical maximum PTE value because the source is matched to 50 Ω and reflection power can be neglected since it is less than 0.1%.

3.2.2. Design of a selective MRC system

Based on the previous design method on the 2-pole BPF model, the center frequency of the passband can be controlled by changing the external coupling values, or the capacitors. Now, we want to expand the previous network to a multiple-receiver system (Fig. 3.5). The previous BPF design method and its frequency response shows that if the center frequency of the receiver is separated, depending on the fractional bandwidth, the cross-coupling effect between the receivers can be isolated up to a certain level. The resonant frequencies of the receivers are determined by (3.21).

$$f_1 = \frac{1}{2\pi\sqrt{L_{rx1}C_{rx1}}},\ f_2 = \frac{1}{2\pi\sqrt{L_{rx2}C_{rx2}}},\ f_3 = \frac{1}{2\pi\sqrt{L_{rx3}C_{rx3}}} \tag{3.21}$$

The selective WPT is designed by the method described in Section 3.2.1 for the power transfer links between the transmitter and three receivers with 2.5 MHz frequency separation.

Because there are multiple Rx coils within a close distance, cross-coupling exists between the Rx coils. Since the passbands of the networks are located at different frequencies, the cross-coupling effect has little impact on the main power transfer link. On the other hand, conventional simultaneous powering systems [21, 38] are difficult to decouple or remove the cross-coupling effect between the receivers which can have significant impact on the system even at a very small change of mutual inductance.

The circuit setup and the power distribution in a three-receiver system are shown in Fig. 3.6 and 3.7. The capacitance at the receivers has a fixed value while it is dynamic on the transmitter. In Fig. 3.6 and 3.7, the system is tuned to Rx #2 (22.5 MHz), which is represented as S_{21}. The sharp dip of S_{11} at the resonant frequency indicates the matching condition between Tx and Rx #2. The resonant frequencies of each receiver are 20 MHz, 22.5 MHz and 25 MHz. Although power leakage to undesired receivers and cross-coupling between receivers exist, which are displayed by S_{31} and S_{41}, the system guarantees less than 2% (< -19dB) of power crosstalk respect to the main power transfer link. Compared to the maximum power transmission ratio in a 2-pole network (Fig. 3.4), the degradation is less than 0.5%. Similar results can be observed in transferring power to Rx #1 and #3. Again, the term $|S_{21}|^2$ at the resonant frequency can be considered as the PTE since the reflection power is less than 0.4%. The calculations show that the power is exclusively delivered to the designated receiver node and power isolation is guaranteed to a sufficient level.

3.2.3. Design of selective WPT system in a dynamic environment

Although the design is optimized at a 40 mm vertical distance, the power transmission is not quite optimized when the coils approach each other. This is because as the distance between the coils decreases, the coupled condition enters over coupled region and frequency splitting occurs [49]. Since this work includes dynamic capacitor network, an adaptive distance tuning system can be integrated without additional effort.

We will assume the capacitance on the receiver is fixed, as it is difficult to implement a dynamic capacitance system in a miniature environment. There are many literatures on techniques to compensate for distance variation in WPT but the methods are based on tuning the inductance or changing the frequency of the power source which is not desired due to increased complexity of the system and size [41, 50]. Others assume the system with infinite Q where it is not true in miniature applications [21, 40]. In this work, the matching condition for distance variation is obtained by fixing the external coupling value, M_{23}, to the value obtained in Section 3.2.2. This will keep the capacitors in the receiver constant. Now M_{12} can be calculated for different coupling coefficients that maximizes (13). Therefore, only the capacitance in the transmitter will change for distance variation. If the Q-factors of the resonators are infinite, single-side tuning can achieve perfect matching condition [40], resulting theoretical maximum power transfer efficiency. In this miniature-sized WPT system, single-side tuning can recover over 80% of the theoretically maximum power transfer which can be achieved by double-side tuning at distance range from 10 to 40 mm.

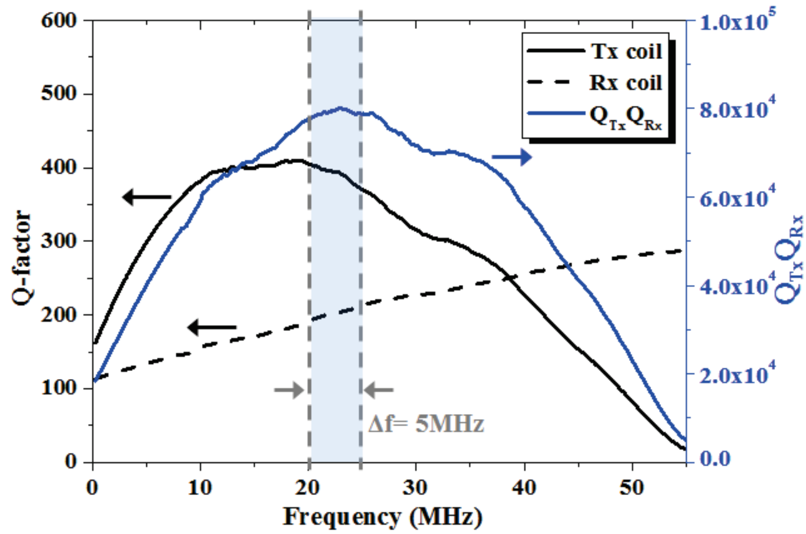

Fig. 3.8. Measurement of the Q factors for Rx and Tx coils.

Table. 3.1 Coil inductance at design frequencies

Coil	20 MHz	22.5 MHz	25 MHz
Tx Coil	491 nH	496 nH	502 nH
Rx Coil 1	358 nH	359 nH	360 nH
Rx Coil 2	351 nH	351 nH	352 nH
Rx Coil 3	363 nH	364 nH	365 nH

Table. 3.2 Optimum capacitance values for the selective mrc

	Power Transfer Link	Rx	Tx
Capacitance values	Rx #1 (20 MHz)	C_{s1}: 200.5 pF	C_S: 141.7 pF
		C_{p1}: 1474.8 pF	C_P: 1416.6 pF
	Rx #2 (22.5 MHz)	C_{s2}: 159.7 pF	C_S: 110.2 pF
		C_{p2}: 1244.4 pF	C_P: 1180.2 pF
	Rx #3 (25 MHz)	C_{s3}: 123.8 pF	C_S: 87.7 pF
		C_{p3}: 1043.2 pF	C_P: 1000.7 pF

3.3. Fabrication of a selective MRC system

The first step of constructing an MRC system is to fabricate and characterize the coils. The size of the coil is selected by considering the application dimensions and the power requirements. For a high power application, power transfer efficiency would be the most important factor in the WPT system so a coil with high Q is favored over compact dimension. On the other hand, in a wireless sensor network or portable device application, maintaining the system in a compact size while keeping the power efficiency at an acceptable level would be important. This work will demonstrate the latter case.

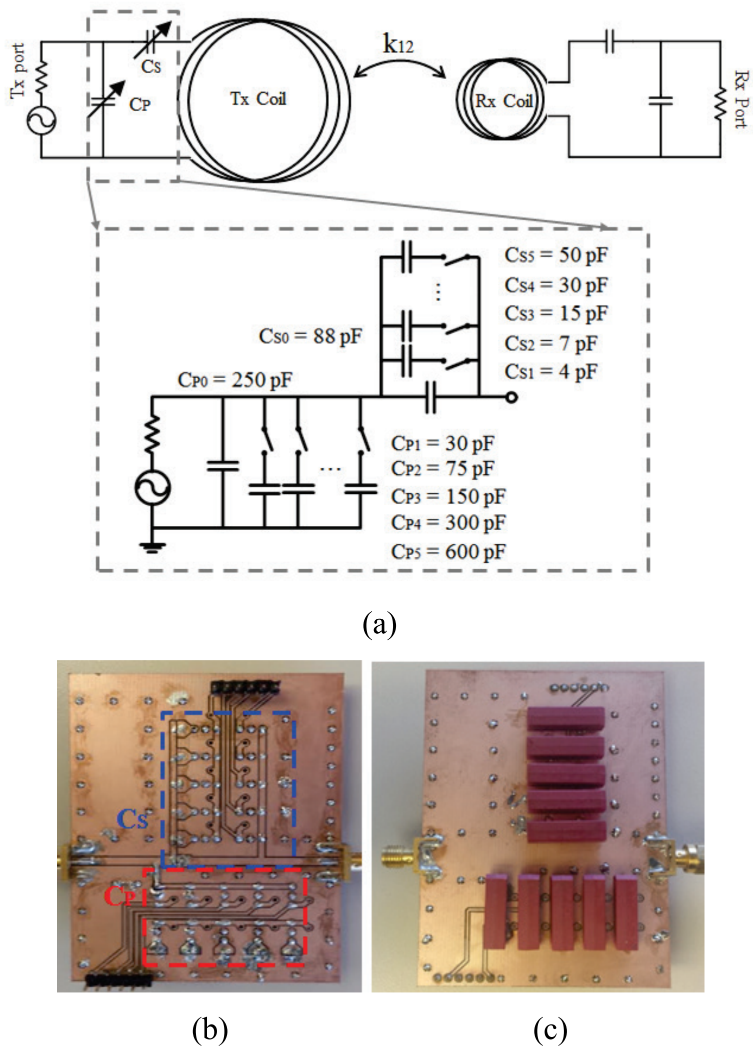

Fig. 3.9. Dynamic capacitance system for the transmitter. (a) Schematic. (b) Top picture. (b) Bottom picture (flipped).

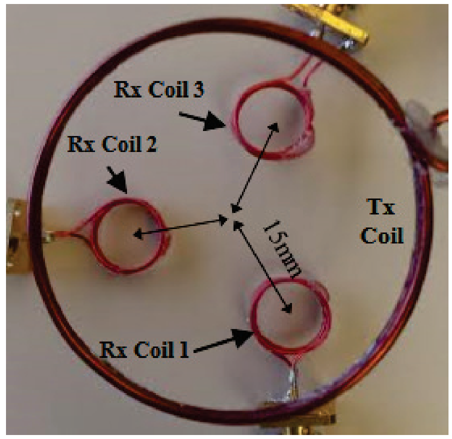

Fig. 3.10. Selective MRC measurement

The Rx coils are a part of the portable device. Thus the receiver coil should be small and the wire needs to be thin. In this demonstration, we used a standard AWG-14 wire for the Tx and AWG-22 wire for the Rx coil. Fig. 8 illustrates the measured Q-factor for the Tx and Rx coils respect to frequency. The operation frequency of the system is chosen by locating the maximum frequency range of $Q_{Tx}Q_{Rx}$. Since the inductance of the coils changes respect to frequency, the coils are characterized along the design frequency range (Table 3.1). Little inductance variance exists within the coils due to handwork. The displacement of the coils is shown in Fig. 3.10 where the vertical distance between Tx and Rx is 40 mm. Then the mutual inductance between the coils can be measured by using the VNA. Once all the coil parameters are determined, the lumped element values and the expected performance can be calculated as Table 3.2 by the design method presented in Section 3.2.

In this paper, relay switches (9002-05-00, Coto Tech.) were used at the transmitter to implement dynamic capacitance (Fig. 3.9). Depending on requirements, other type of low loss switches can be used to replace relays. The receiver side has fixed capacitance values as previously mentioned.

3.4. Measurement and system demonstration

In this part, the frequency response of the selective WPT system is measured using a VNA. Also the efficiency of the system is measured for both stationary and mobile cases.

Then the power division and TDMA operation is demonstrated. Lastly, the safety issue regards to a biomedical application is discussed.

3.4.1. Power transfer efficiency measurement results

The frequency response of the selective WPT system is measured using a 4-port VNA (N5230C, Agilent). Fig. 3.11 shows the measured S-parameters, matched to Rx #2 (22.5 MHz), in the setup shown in Fig. 10 (k_{12} = 0.01). The S-parameter measurement results show close resemblance to the simulated frequency response. As η_{11} is less than 1%, if we neglect the power reflection, the power transmission ratio η_{21} can be considered as the PTE at the resonant frequency with the matched condition.

To measure the power transmission, a signal generator (N5172B, Agilent) with a power amplifier (ZHL-1-2W-S+, Mini-Circuits) was used as the power source and a signal analyzer (N9010A, Agilent) was used to measure the received power. The measurement was performed with the source power at 2 W and all the loads terminated to 50 **Ω**. The results are shown in Fig. 3.12, where the efficiency is 23.98~28.84%. Power transferred to irrelevant receivers is less than 0.6%.

The differences from the calculation results are due to the losses in the relay switches and mismatches from the optimum capacitance value. Table 3.3 compares the power transfer efficiency with those of other works with multiple receivers. Although, no Q or coupling enhancement techniques were used in this work, the power transfer efficiency respect to the normalized distance is competitive compared to others.

A demonstration of the WPT under distance variation is displayed in Fig. 3.13. One of the receivers is changing its vertical displacement and others remain stationary at its original location (40 mm vertical distance and 15 mm misalignment). When all the capacitance values are fixed, the power transmission ratio starts to decrease as the receiver approaches the transmit coil beyond the critical coupling point. In a simultaneously powered multiple-receiver system, it is difficult to cope with degradation due to misalignment. But the selective WPT system in this work can restore the power delivered to the load by tuning the dynamic capacitance at the transmitter and compensate for the change of coupling strength, individually.

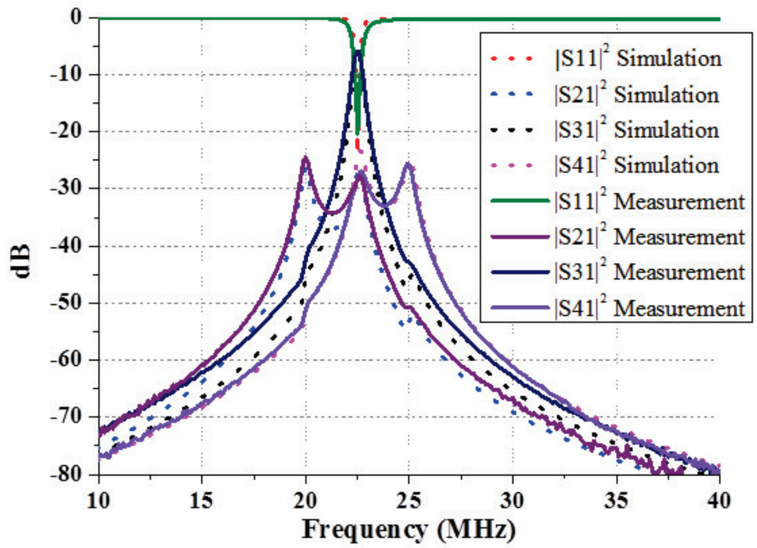

Fig. 3.11. Measurement compared with the calculated results for selective WPT. Tx tuned for Rx #2 at 22.5 MHz.

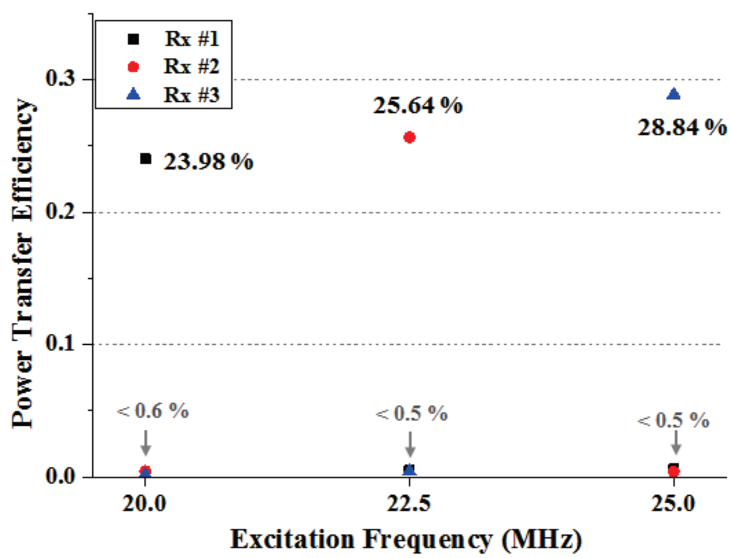

Fig. 3.12. Measured PTEs of the three receiver system. Energy transferred to undesired receiver is less than 0.6%.

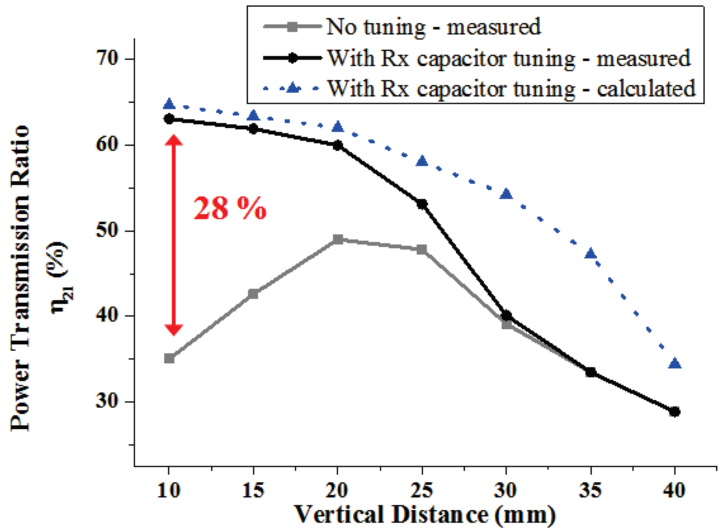

Fig. 3.13. Power transmission ratio measurement under distance variation. The ratio is improved up to 28% by tuning the Tx dynamic capacitance, indicating that more power is delivered to the load.

Table. 3.3 PTE comparison of multiple receiver WPT systems

	Rx coil size (Rx)	Tx coil size (Tx)	Distance (d)	Normalized distance (r)	No. of receivers	Adaptive distance tune	Power division control	Efficiency (PTE)
[39]	150 mm	150 mm	130 mm	0.867	2	No	No	0.51 ~ 0.55
[37]	315 × 225 mm^2	350 × 300 mm^2	160 mm, 280 mm	0.749	2	No	No	0.60
[21]	300 mm	300 mm	160 mm†	0.533	2	No	Yes	0.87
This work	12 mm	56 mm	42.7 mm	1.647	3	Yes	Yes	0.24 ~ 0.29

† Includes a repeater coil located in between transmitter and receiver.

Normalized distance (r) is defined by $r = \frac{d}{\sqrt{Rx \times Tx}}$, where d is defined as distance between center to center of coils.

3.4.2. Demonstration of power division

A voltage rectifier is required to demonstrate the power division control in time domain. For the rectifier, we implemented a two stage voltage doubler using schottky diodes (HSMS-282, Avago). A 1 kΩ resistor is used as the load of the rectifier, which can represent a typical biomedical sensor application [28]. Function generator is then used as the power source and a microcontroller (ATmega328P, Atmel Corp.) controls the relay switches of the dynamic capacitance. As it can be seen from Fig. 3.9(a), the microcontroller uses 10 digital bits to control the 10 switches of the dynamic capacitance. The switch closes when the digital bit is high and opens when low. The coils are displaced as shown in Fig. 10 and the vertical distance between the Tx and Rx coil is 40 mm. Equal time distribution is shown in Fig. 3.14(a). A 25 mW source is used. For the first 10 ms interval, the power source is set to 20 MHz and the dynamic capacitor is matched to Rx #1, according to Table 3.2. The DC voltage measured in Fig. 3.14(a) shows that power is selectively delivered to only Rx #1 during this time.

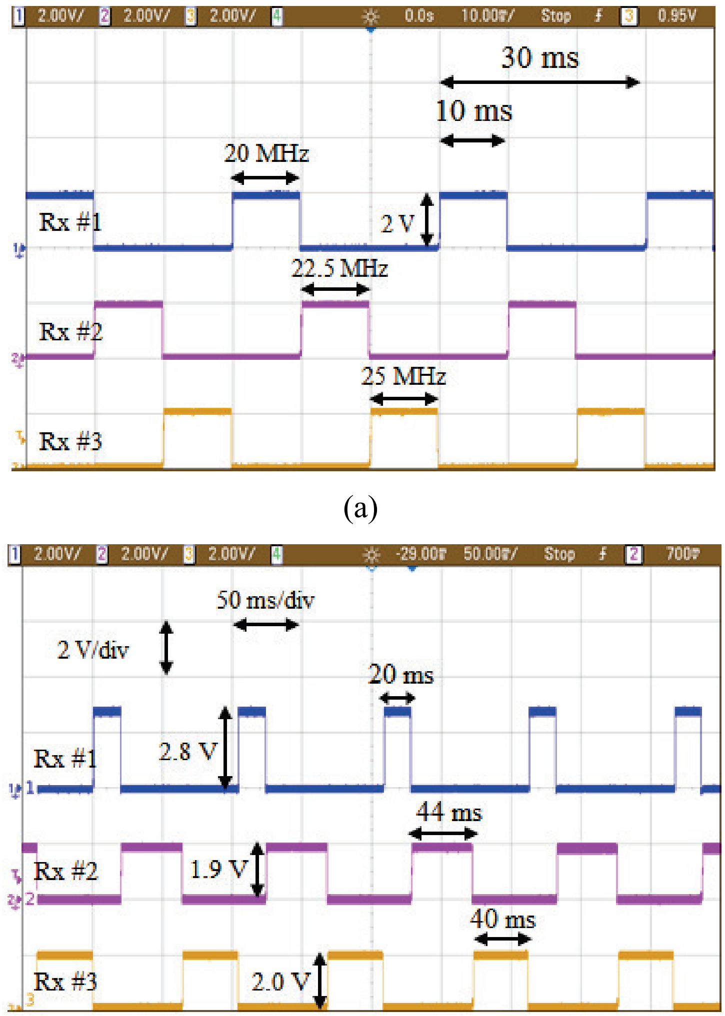

(a)

(b)

Fig. 3.14. Time domain measurement of the load voltage at the rectifier in a three-receiver system. (a) Each node is powered for 10 ms. (b) Power division management for equal power distribution.

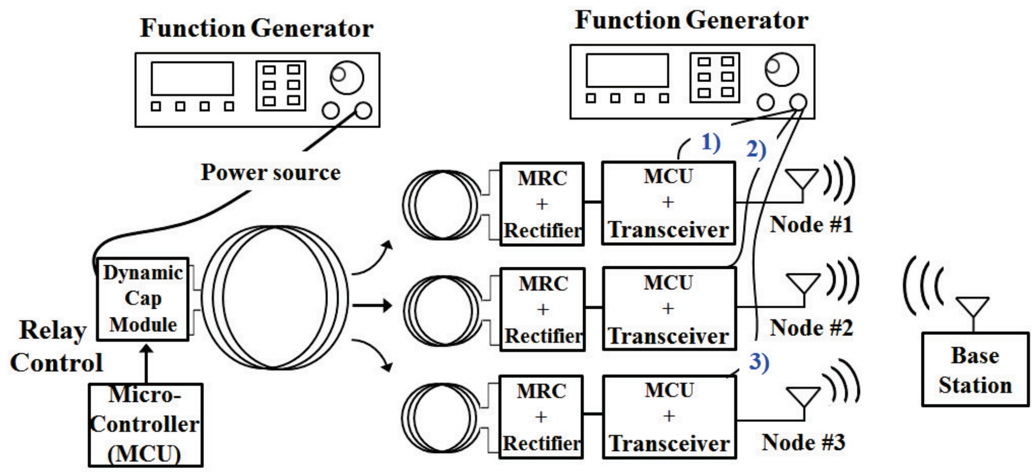

Fig. 3.15. Test setup for TDMA demonstration. 1), 2), and 3) are the analog signals of positive-ramp sawtooth, negative-ramp sawtooth and sine wave which are digitized by the ADC and wirelessly transmitted out. The data transmission occurs when power is present, similar to the timeslot shown in Fig. 3.14(a). Base station receives data in a time-division multiplexed manner for the three nodes.

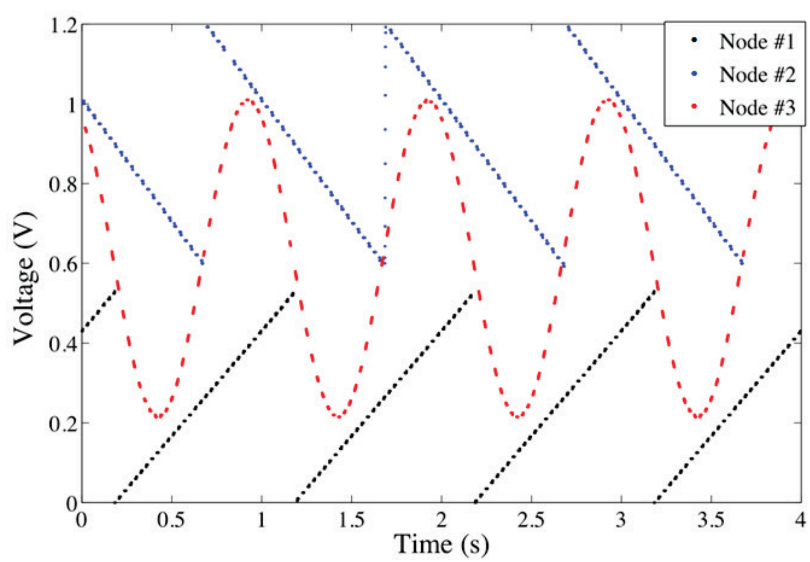

Fig. 3.16. Reconstructed waveform from the data received at the base station. Each node transmits digitized information for its analog signals in a time multiplexed manner and the original analog signal is reconstructed with the data received by the base station.

After the first 10 ms interval, the power source is changed to 22.5 MHz and the dynamic capacitor is now set to Rx #2. Similarly, all the receivers are powered for 10 ms in a 30 ms cycle. The time interval and the period can freely be controlled.

If equal power distribution is required among multiple receivers, the time interval can be changed as Fig. 3.14(b). In this example, Rx #1 is moved to 20 mm from the Tx coil and other receivers remain stationary. The dynamic capacitance at the transmitter is matched to Rx #1 by the technique demonstrated in Section 3.4.1. During the first time interval of 20 ms, the source frequency is set to 20 MHz and the dynamic capacitance is matched to Rx #1. The DC voltage measurement in Fig. 3.14(b) shows that power is selectively delivered to only Rx #1. During the second time interval of 44 ms, the source frequency is changed to 22.5 MHz and the dynamic capacitance is matched to Rx #2, according to Table 3.2. The method is similar for Rx #3.

From (3.22), it can be shown that the DC power at each node rectifier is balanced.

$$\frac{2.8^2\,[V^2]}{1000\,[\Omega]}\times\frac{20\ ms}{104\ ms}:\frac{1.9^2}{1000}\times\frac{44}{104}:\frac{2.0^2}{1000}\times\frac{40}{104}=1:1.013:1.021 \tag{3.22}$$

3.4.3. Demonstration of TDMA

WSN and biomedical sensor devices require minimal power consumption for longer device lifetime and WPT coverage range. Due to this reason, multiple node synchronization in such applications is usually achieved by TDMA. Each node has its own timeslot for data transmission and this is determined by an external signal. Selective WPT and its power distribution can serve as synchronization signal for a one-way TDMA communication.

The verification setup is shown in Fig. 3.15. Demonstration of the TDMA is performed by using a commercial off-the-shelf microcontroller embedded transceiver (nRF51822, Nordic Semiconductor) attached to the receivers, which acts as a wireless sensor node. The selective WPT system with the rectifier supplies power to the transceiver. The transceiver is put into idle mode (2.6 μA of current consumption) when no power is received, and wakes up when power is present. The wake-up signal is generated from the first stage of the voltage doubler, which has a small time constant. The output of the first stage of the doubler is similar to Fig. 3.14(a), and the second stage of the voltage doubler supplies power to the transceiver. All the transceivers transmit at the same frequency channel and transmit data only when the power is present. Since the transceiver has an embedded microcontroller and an analog-to-digital converter (ADC), analog signals were fed into each node for verification. A positive-ramp sawtooth, negative-ramp sawtooth and a sine wave is introduced to the ADC of each node, respectively. The ADC in each node digitizes the analog signal and the transceiver transmits the corresponding information when power is present, similar to the timeslot shown in Fig. 3.14(a). The data transmitted from three nodes is then received at the base station in a time multiplexed manner. The transceiver does not have to be in the receive mode for multi-node synchronization purpose and the overall multi-access communication architecture is significantly simplified. The reconstructed waveform from the demodulated data at the base station is shown in Fig. 3.16, which concurs with the analog signal introduced to each node.

The minimum duration time per node in the current demonstration is mainly limited by the transceiver's wake-up protocol but it can be shortened by using a custom radio for further resolution improvement.

3.4.4. Safety considerations for biomedical applications

For an implantable biomedical application, the receiver should be hermetically sealed by a bio-compatible material. Many research groups are investigating such technologies [51, 52] and depending on the surgical situation, an appropriate material can be chosen.

In order to expand the application to in-vivo studies, the specific absorption rate (SAR) should be under the safety limits. HFSS (Ansys) was used solve the electromagnetic field effect. Blood was selected as the homogeneous phantom tissue since it is one of the lossiest human tissues. The electrical parameters of the blood was obtained from [53] at 20 MHz. The Tx coil is excited with a 2 W source, 5 mm away from the phantom tissue. Fig. 3.17 shows the calculated results with peak localized SAR of 0.46 W/kg, which is 4 times less than the 2 W/kg guideline of the International Commission on Non-Ionizing Radiation Protection (ICNIRP).

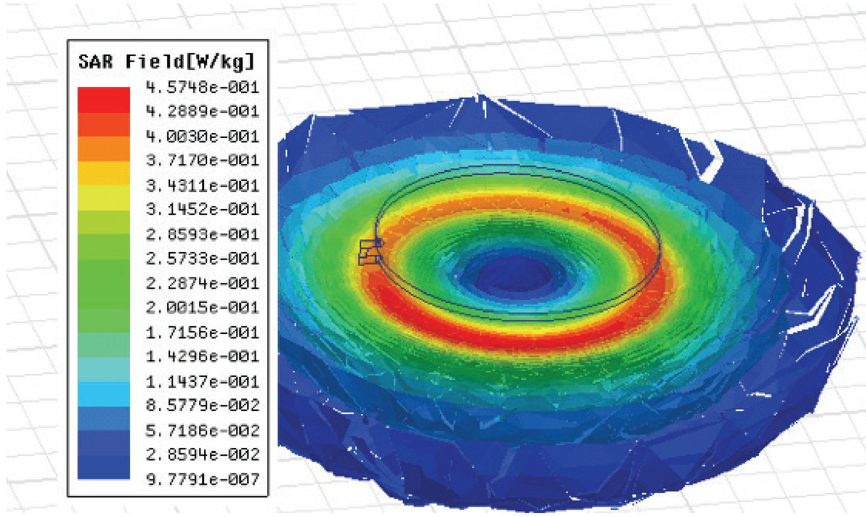

Fig. 3.17. Simulation result of local SAR field. Peak field is 0.46 W/kg, which is 4 times less than the ICNIRP regulation.

3.5. Conclusion

This work demonstrated a selective WPT methodology for a multiple-receiver system. Selective WPT can achieve high power transfer efficiency with accurate control over power division in a dynamic environment. A demonstration of the adaptive distance tuning and TDMA is demonstrated in a three-receiver system. The potential for in-vivo study is verified under the ICNIRP regulations, using an electromagnetic field solver.

The proposed selective WPT is fabricated for a portable device charging application and the PTE is mainly limited by the low Q of the receiver coils. For future improvements, Q enhancement techniques can be employed to increase the overall efficiency. The application can also extend to a larger and higher power system at a lower operation frequency. The design and demonstration in this work provides a guideline for smart, energy efficient wireless power transfer in a multiple-receiver system.

4. LOW POWER, INJECTION LOCKED RING OSCILLATOR BASED TRANSMITTER FOR SELECTIVE MRC SYSTEMS

4.1. Introduction

4.1.1. Motivation

Power consumption is one of the biggest concerns in the implantable wireless sensor network (WSN) application [54]. Efforts were focused on miniaturization and as a result many research groups have developed wirelessly powered device without the use of a battery systems [7, 10, 30]. But obviously, wireless power transfer technique has its limits. The coverage range is limited by the device power consumption and specific absorption ratio (SAR) regulation. Also, implantable sensor is generally in motion, which indicates that intermittent power outage can occur depending on the location of the device. In order to overcome such problems, the power consumption of the device has to be minimized. It is known that the radio consumes most of the power in a sensor node [8, 28] and many researchers have been investigating low power transceiver techniques.

In addition to minimizing the device power consumption, a robust WPT protocol has to be developed to deliver a reliable power source to the sensor node. Wireless power transfer can be categorized into two fields: RF radiation and inductive coupling. RF radiation is known to have longer coverage range with low transfer efficiency as a tradeoff. Also the radiation frequency has to be high enough so that the antenna can fit in the device. But on the other hand, when the radiation frequency is high, medium attenuation becomes intolerable that it is almost impossible for an implantable application. The antenna detuning is very difficult to predict under different medium shape and type, such as tissue, muscle, fat or bone [55, 56]. The inductive coupling or magnetic resonance coupling method has the advantage of high power transfer efficiency at the cost of coverage range. Although the coverage range is short, for implantable applications, power transfer is quite reliable since inductors are predictable under different medium and the compensation can be made from the power transmit coil [57, 58]. In addition, the tissue attenuation is negligible for MRC [15], whilst the RF radiation is not.

In this paper, we propose and implemented a wirelessly-powered multi-node low-power SoC for glucose detection. The chip is wirelessly powered with a magnetic resonance coupled link in the 27 MHz, ISM-band and the MRC signal is injected to the internal oscillator for frequency lock. An edge combiner is then used to multiply the oscillator frequency to a 405 MHz, MIC-band and to transmit out through an electrically small loop antenna. Multi-node synchronization is demonstrated by the power transmit coil and its associated network explained in [57] with a microcontroller. The glucose detection is performed by a potentiostat and a current-to-frequency (I-F) converter where it is internally duty cycled for minimal power consumption. A miniature glucose sensor is fabricated on graphene petal and integrated to the SoC for demonstration.

4.1.2. Prior art overview

There has been works on multi-node energy-harvested SoCs for wireless sensor network. Most of the cases, there are two communication channels needed. One is needed for the data transmission and another for either energy transfer or data reception for multi-node synchronization. In terms of data transmission, work has been focused on minimizing the power consumption by replacing the phase lock loop (PLL) or delay lock loop (DLL) with other low power frequency locking techniques to establish a solid communication channel [10, 12, 59]. In extreme cases where low power is the most important factor among design parameters, frequency locking is ignored at the cost of carrier frequency drift so sometimes the receiver design can become challenging [60]. Either case, conventional PLL is not desired in a low power design since just by itself usually consumes around 1 mW [61-63].

As an effort to minimize the device size and lifetime, most of the recent work has energy harvesting function integrated on chip in various ways such as vibration, magnetic couple, RF radiation, or small electrical potential energy[4, 30, 35, 64, 65]. Although vibration or small electrical potentials are widely available in various ways, the foot print of the implantable wireless sensor node application is so small that the amount of extractable energy is scarce, leaving the chip with very little power to spare. RF radiation is another attractive technique for its long distance but the size of the antenna is the bottleneck. The wavelength for 915 MHz, ISM-band is about 30 cm which is somewhat difficult for antenna integration and if the operation frequency is increased to or beyond 2.4 GHz, the antenna suffers from various attenuations including human body and frequency detuning. In order to obtain reliable energy source in a small footprint, magnetic resonance coupled energy is an effective solution for its motion track compensation techniques and high efficiency in body area application [57, 58].

Among these techniques, extensive work has been done to extract clock source from the wireless power transfer, especially the RF radiation [10, 11, 30], which is convenient to manipulate due to its higher frequency. There are work reported on low frequency injection locking but ideal signal source or crystals have been used as the injection signal [8, 66].

4.2. Ring oscillators and injection locking

Ring oscillator has attracted much attention in many communication systems because of its integrated nature, low power. A ring oscillator is a chain of delay cells where the output of the last stage is fed back to the input of the chain, which completes a 'ring' (Fig. 4.1). The oscillation period is the time it takes a transition to propagate twice around the loop. For an N-stage ring oscillator, the oscillation frequency is approximated as (4.1) where t_d is the propagation delay of each delay cell.

$$f = \frac{1}{2Nt_d} \tag{4.1}$$

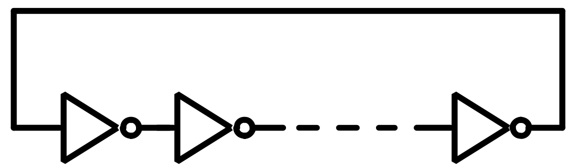

Fig. 4.1 Ring oscillator

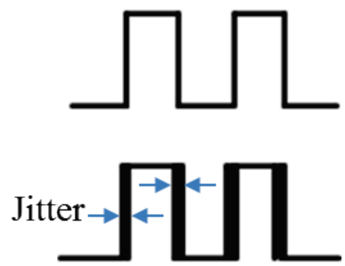

Fig. 4.2 Clock jitter

Jitter is defined as "short-term variation of a signal from its ideal position in time" and its transient characteristic is illustrated in Fig. 4.2. The frequency domain representation of jitter is called phase noise which is characterized by single-sideband noise spectral density (dBc/Hz).

To use the ring oscillators as the internal clock for the carrier frequency, there are couple things to be considered a forehead. First, the clock has to be at a stable constant frequency. Second, the phase noise has to be low enough. And lastly, the power consumption should be significantly lower than conventional frequency synthesis techniques.

Low phase noise clock synthesis can be achieved by injection locking the clock frequency with environmental couplings: MRC. Injection lock was first observed by Christiaan Huygens in 17th century, known as the pendulum synchronization phenomenon. Injection locking can be categorized as three types: first-harmonic, sub-harmonic and super-harmonic injection locking. First-harmonic is the most simplest injection locking method and the injection frequency is the fundamental frequency of the oscillation. Sub-harmonic and super-harmonic injection locking method is injecting sub-harmonic or harmonic of the oscillation frequency. The MRC frequency is usually in the sub-100MHz range and wireless communication frequency is at least hundreds-of-MHz range. So in our case, a sub-harmonic injection locking method is applicable.

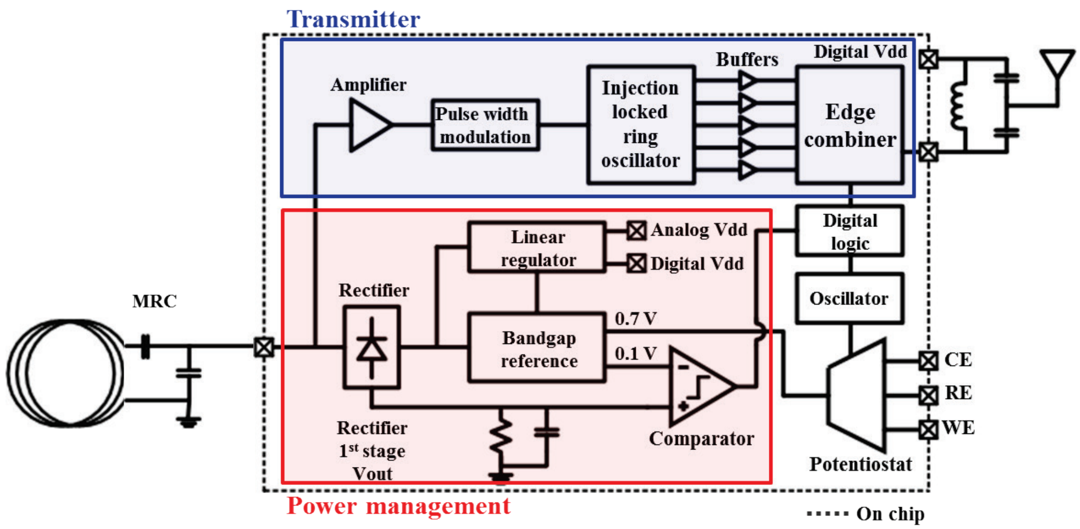

Fig. 4.3 Full IC architecture

4.3. Proposed IC architecture

The full IC architecture is shown in Fig. 4.3. It is composed of the MRC with power management block to supply constant DC power to the entire IC. A comparator is there to detect selective WPT so that the transmitter only transmits when there is an incoming WPT.

Transmitter part is composed of a pulse width modulation block, injection locked ring oscillator and an edge combiner. The injection locked ring oscillator runs at 81 MHz. Then an edge combiner multiplies the 81 MHz to a 405 MHz, in MICS (Medical Implant Communication Service) band.

There is a potentiostat as the analog block of the system. It is commonly used in a three-electrode cell and the three electrodes are used for detection of glucose level and the analog data is converted to a frequency and transmitted out.

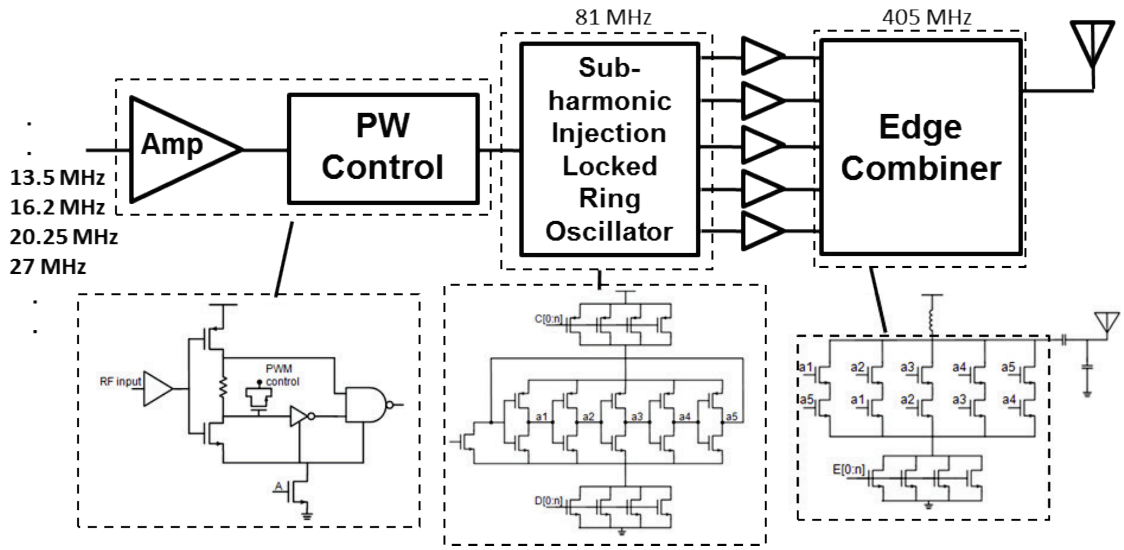

Fig. 4.4 Transmitter architecture

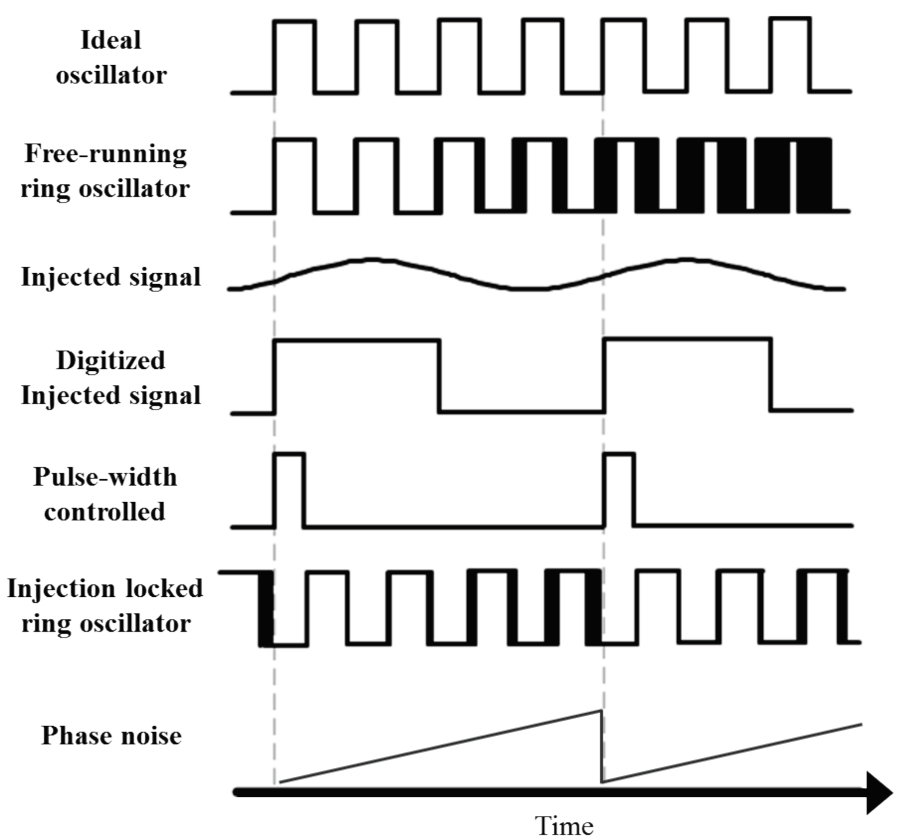

Fig. 4.5 Injection locked oscillation scheme

4.3.1. Transmitter

The transmitter is composed of an amplifier, pulse width (PW) control, injection locked ring oscillator and edge combiner block. When the MRC injected signal enters the IC, the initial amplifier slightly amplifies the signal so that a rail-to-rail signal is obtained. This is described in Fig 4.5 as the digitized injected signal. Then the pulse width controller block modifies the pulse width so that it can be used for injection in the ring oscillator as shown in Fig. 4.5. The ring oscillator locks onto the injected signal, maintaining at a constant frequency and suppressing its phase noise. Lastly, the edge combiner which is commonly used in digital circuits is used to multiply the frequency at the ring oscillator and transmits this out through an antenna.

The MRC signals can take various divisions of 81 MHz, including the ISM band, 27 MHz. The PW control block is composed of an inverter, variable capacitor, a delay cell and a NAND gate. The incoming digitized signal goes into the inverter and by controlling the variable capacitance, correct signal shape can be created. The PW modified signal is then injected into the ring oscillator which locks the oscillation frequency at 81 MHz. A simulation of phase noise comparison with free-running ring oscillator is shown in Fig. 4.6.

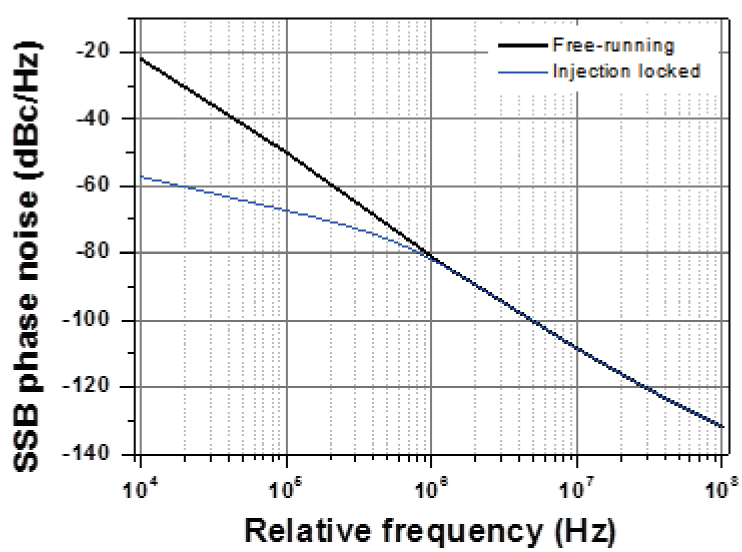

Fig. 4.6 Simulated phase noise of ring oscillator oscillating at 81 MHz

A detailed schematic of the individual blocks are displayed in Fig. 4.7-4.9.

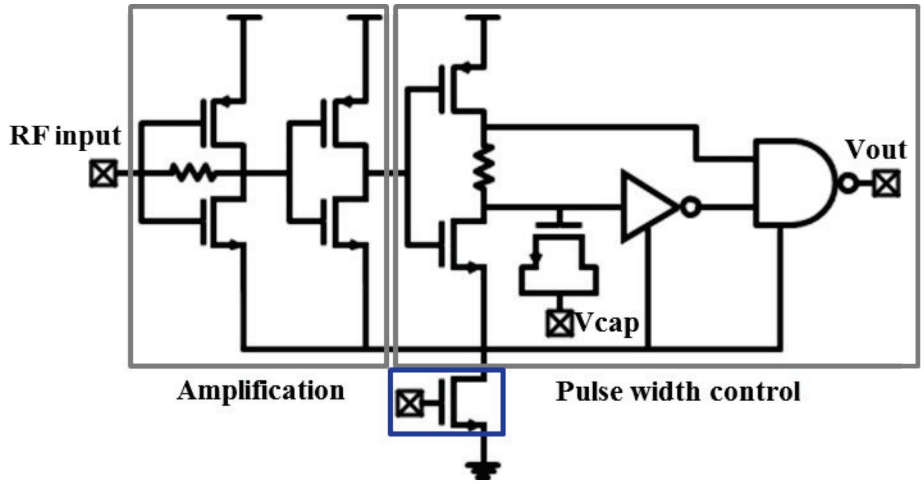

Fig. 4.7 Schematic of the amplification and pulse width control block

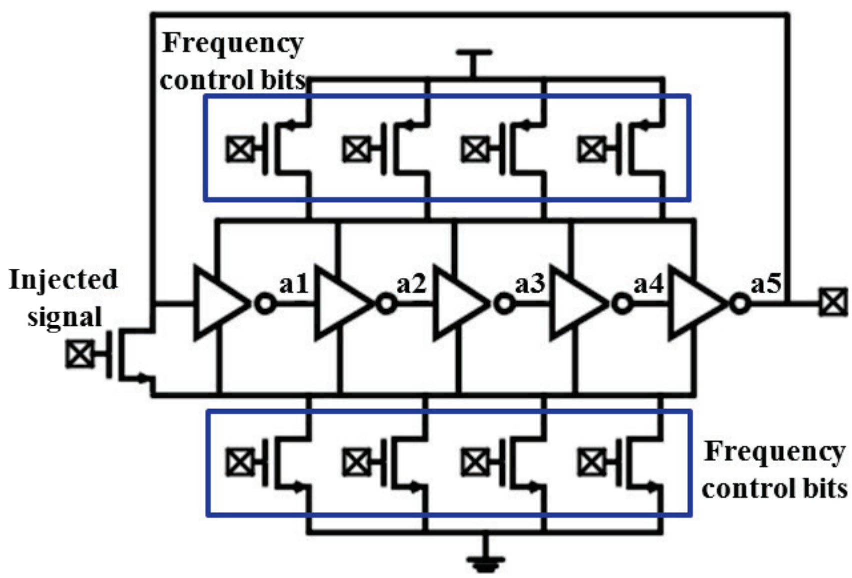

Fig. 4.8 Schematic of the injection locked ring oscillator

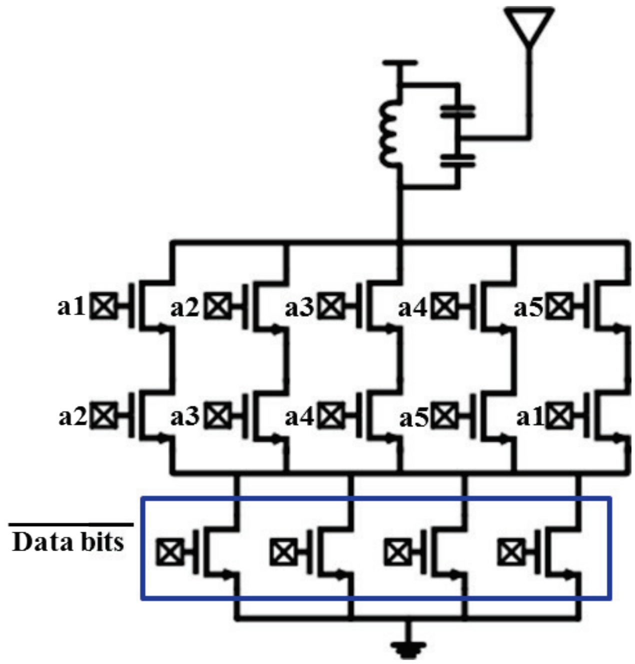

Fig. 4.9 Schematic of the edge combiner

The blue lines indicate high V_t devices to reduce leakage current for power saving when it is not transmitting, or it is in shutdown mode. Static asymmetry trimming inverters are added after the multiphase outputs of the ILRO to sharpen the edges of the waveform to make it suitable for efficient transmission at the edge combiner. The edge combiner multiplies the frequency by five. The waveform is described in Fig. 4.10. The drain of the edge combiner is directly connected to the matching network and the antenna for radiation.

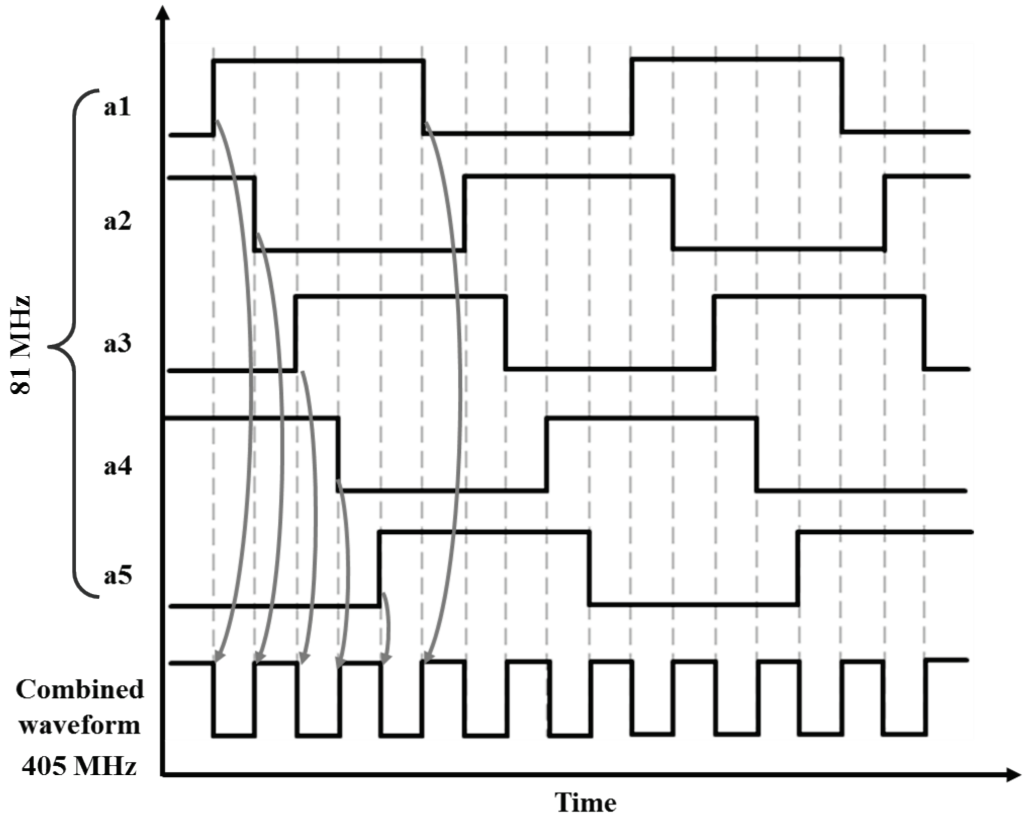

Fig. 4.10 Waveform of the multiphase outputs of ILRO and edge combiner

4.3.2. Power management and MRC

The system is wirelessly powered by magnetic resonance coupling, explained in chapter 3. As long as the frequency of the incoming powering signal is a division of a whole number of 81 MHz, the ILRO will lock to 81MHz. A rectifier converts the high frequency signal into a DC. Bandgap reference and low-dropout regulator conditions the DC into a stable power source that supplies the entire IC. A comparator is present in the power management to send the peripheral circuit into a low power sleep mode when there is no incoming MRC power source present. Analog and digital vdds are separated to isolate the switching noise from the digital blocks affecting the analog part. The block diagram is shown in Fig. 4.11.

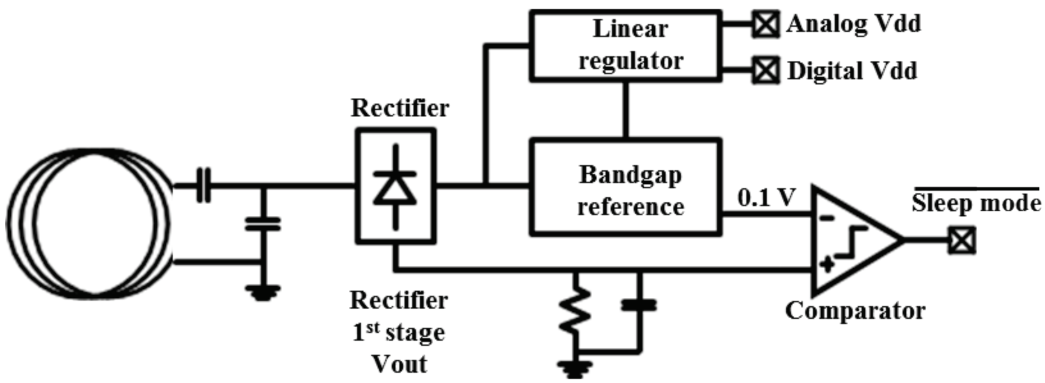

Fig. 4.11 Block diagram of the power management system

The rectifier is shown in Fig. 4.12 where it is composed of 4 stages of voltage doubler with schottkey diodes. A voltage multiplier composed of voltage doublers are used because of their effective voltage boosting strength even with low input signal.

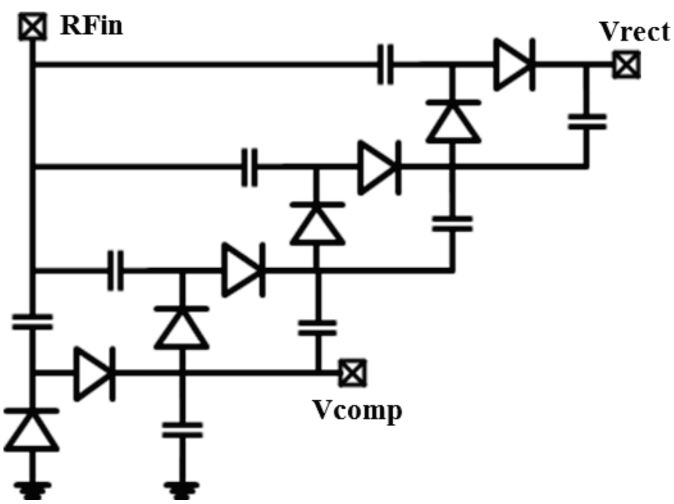

Fig. 4.12 Voltage rectifier. 4-stage voltage doubler.

A low-dropout voltage regulator then conditions the rectified voltage into a constant and stable DC voltage. Off chip capacitor-less design was chosen to minimize the size of the final system. The schematic is shown in Fig. 4.13.

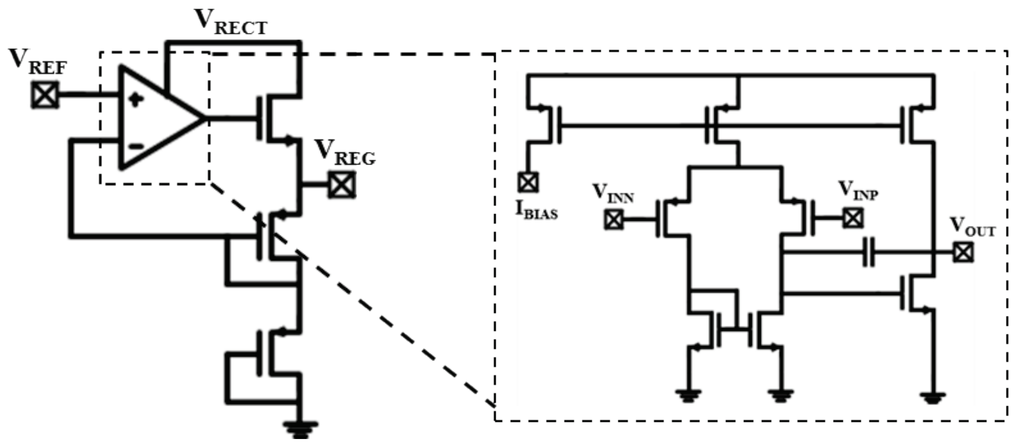

Fig. 4.13 Schematic of the voltage regulator

A bandgap reference also delivers constant current bias and voltage references for the blocks as shown in Fig. 4.14.

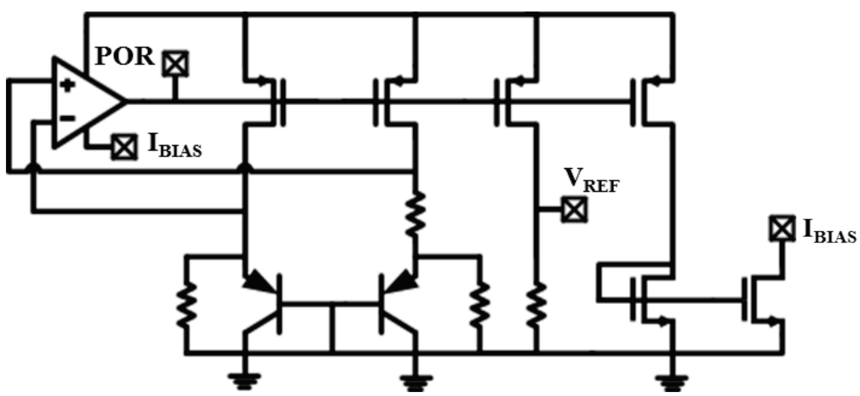

Fig. 4.14 Schematic of the bandgap reference

4.3.3. Continuous glucose detection

The glucose concentration detection is basically an amperometric measurement in a three-electrode potentiostat Details on the electrochemical reaction are explained in chapter 5.

The current measurement is the measured data from the glucose detection and a common way to convert this into information would be through an analog-to-digital converter (ADC). But an ADC is a complicated block that consumes a lot of silicon space and power so a convenient and efficient method is chosen. The current flow is mirrored into a ring oscillator that initially oscillates at a constant frequency. As the current flow increases, the oscillation frequency increases. A reference oscillator is also included in the design for calibration purposes such as temperature and corner variation.

The following figures illustrate the potentiostat. We use the 1.2V analog Vdd as the working electrode potential. Reference and counter electrode is displayed in Fig. 4.16, giving 0.5V difference. In order to improve the precision of the current-copying circuit, a cascode method was used as shown in Fig. 4.16 and 4.17. Also a separate power source was used for the potentiostat to isolate any switching noise injecting from the I-F converter.

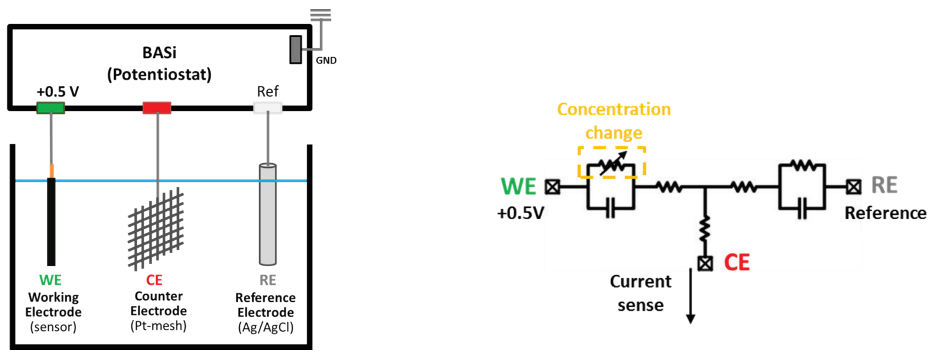

Fig. 4.15 Generic equivalent circuit of the three-electrode electrochemical cell

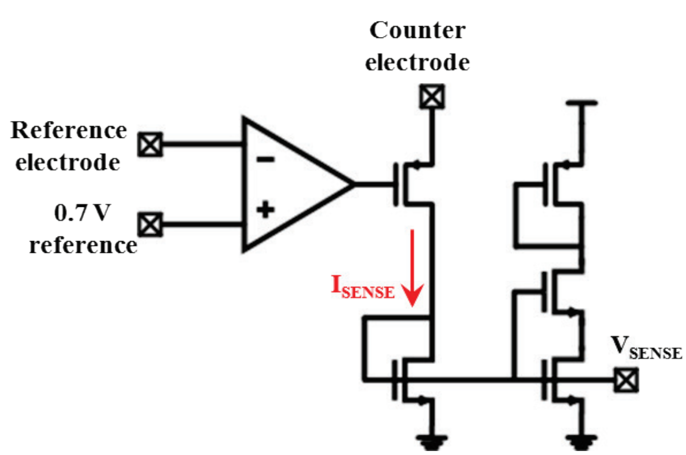

Fig. 4.16 Schematic of the analog potentiostat

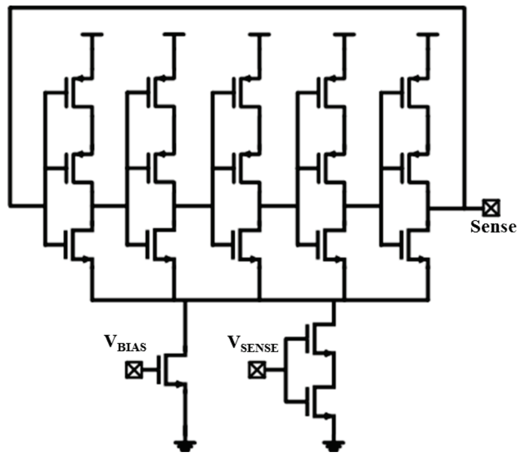

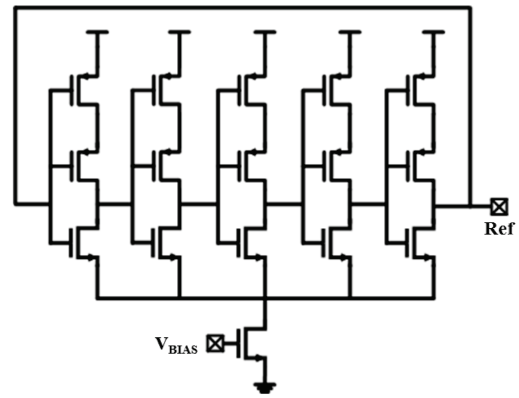

(a) (b)

Fig. 4.17 Schematic of the (a) I-F converter and (b) the reference oscillator

The oscillation occurs typically around 25 kHz but we plan to use a lower frequency for easier communication and less switching events at the edge combiners for lower switching loss. The internal oscillator is used as the clock for duty cycling. The frequencies of sense and reference oscillator are divided by 6 using series of D flip-flops. Then the reference oscillator is used to generate duty cycled pulses for energy efficient communication as shown in Fig. 4.18.

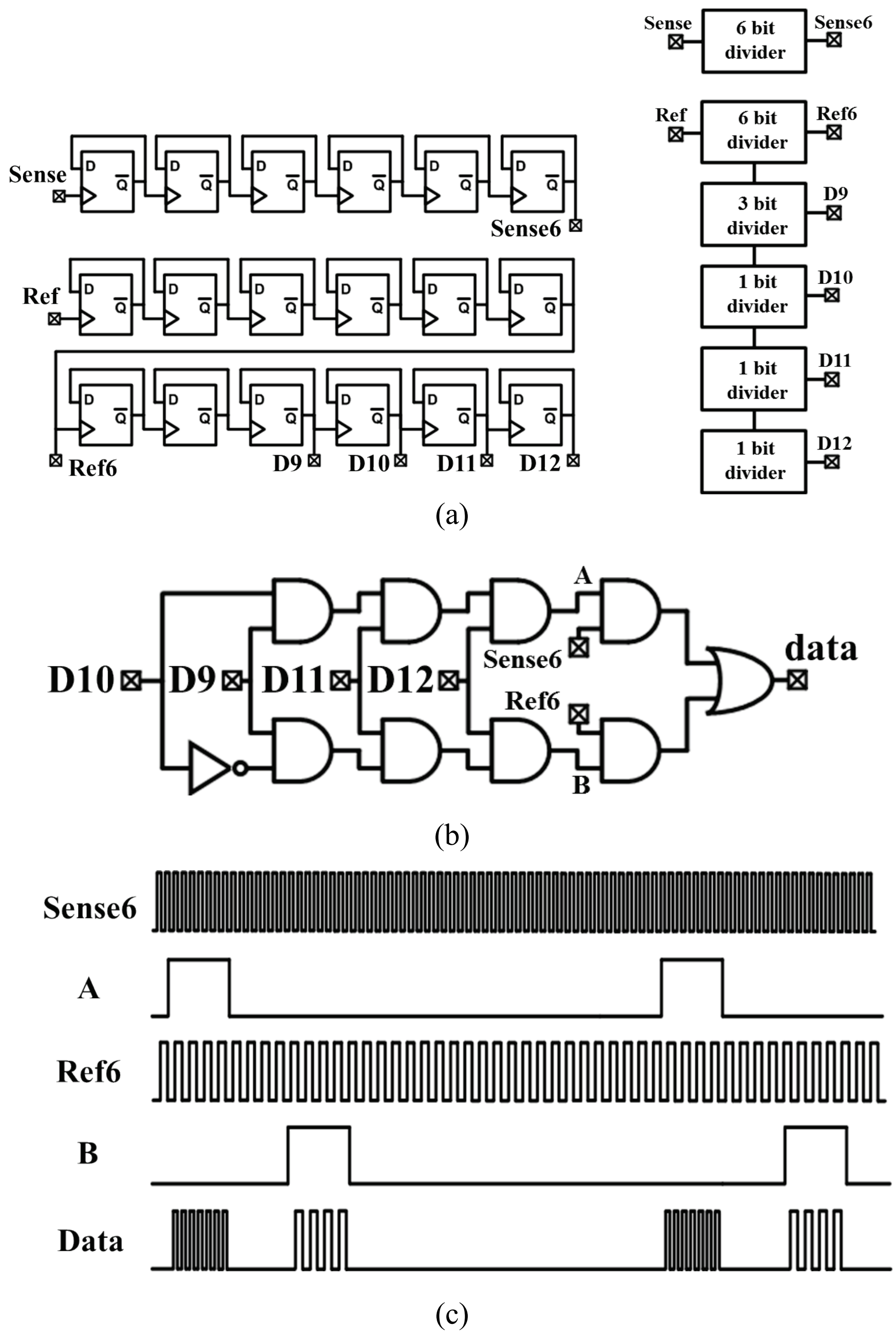

Fig. 4.18 (a) Series of D flip-flops for frequency division. (b) Block diagram for duty cycling (c) Waveform for duty cycling.

4.4. Measurement

We have designed and implemented all the functional blocks described in section 3 using 180 nm CMOS technology. A micrograph of the die is shown in Fig. 4.19. Total area of the chip is 580 μm × 720 μm and the power consumption of the system is measured to be 4.3 μW for the analog parts, 8.2 μW for the I-F converter and 231 μW for the transmitter when it is at on state. The leakage current for the transmitter when it is at off state is less than 4.3 nA.

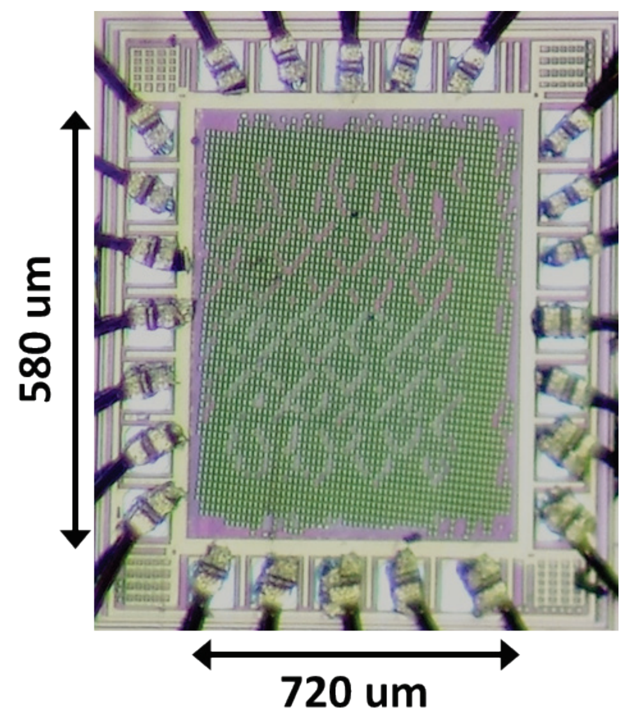

Fig. 4.19 Chip micrograph

The phase noise of the ILRO is measured as Fig. 4.21. It is shown that the ring oscillator locks to its various sub-harmonics and the phase noise is significantly decreased compared to free-running oscillator. The separation of the phase noise of 9^{th} harmonic and the first harmonic is about 20dB after 100kHz offset from the 81 MHz, which meets the prediction of 20logN separation [66].

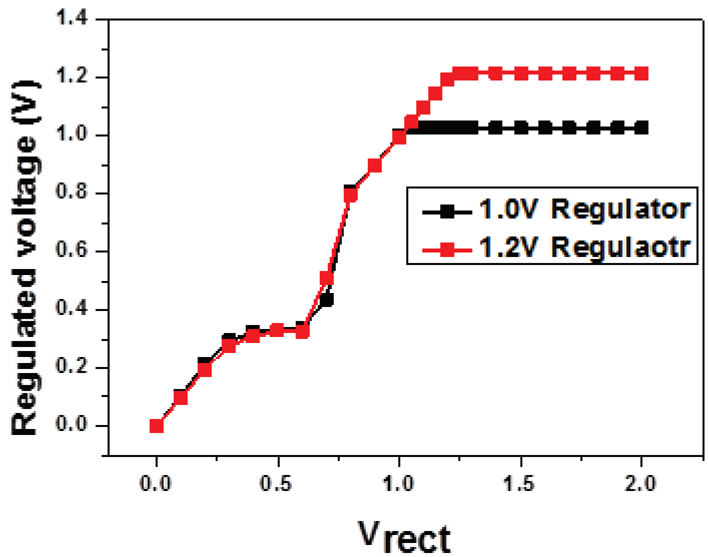

Fig. 4.20 Regulated voltage.

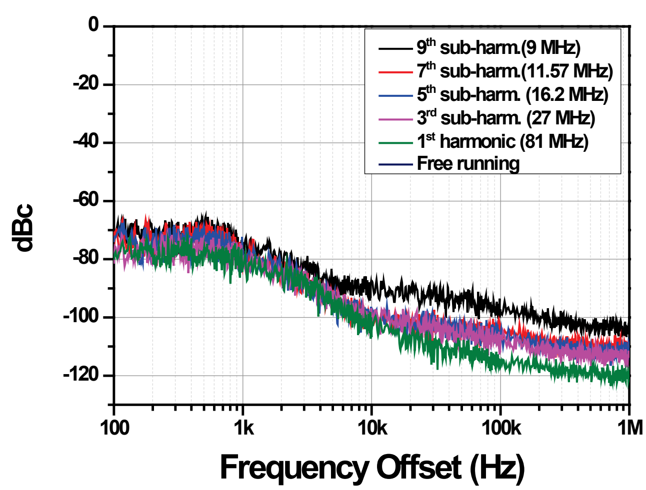

Fig. 4.21 Measured phase noise of the ILRO for different injection frequencies.

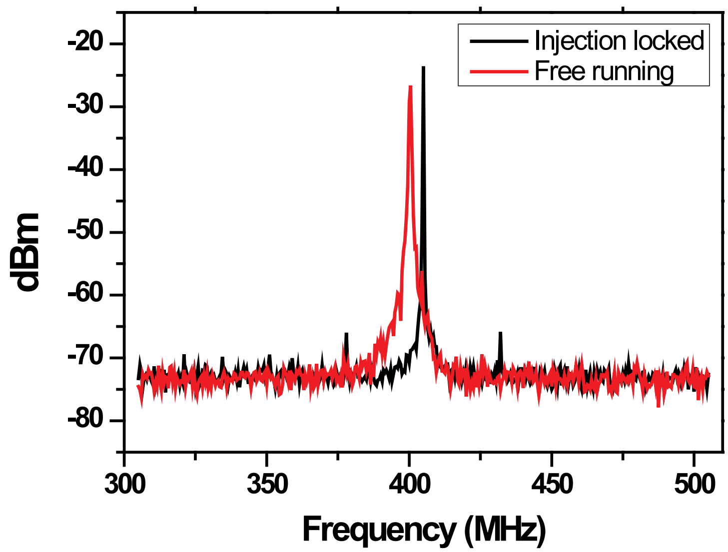

Fig. 4.22 Measured spectrum of the transmitter. Injection frequency of 27 MHz.

The output spectrum of the transmitter is shown in Fig. 4.22. The transmitter's output power was measured to be -22dBm with a 50 Ω termination. For a demonstration purpose, the transmitter is connected to a pseudo-random-number-generator with a bit rate of 3Mbps and the received data is demodulated faithfully as shown in Fig. 4.23.

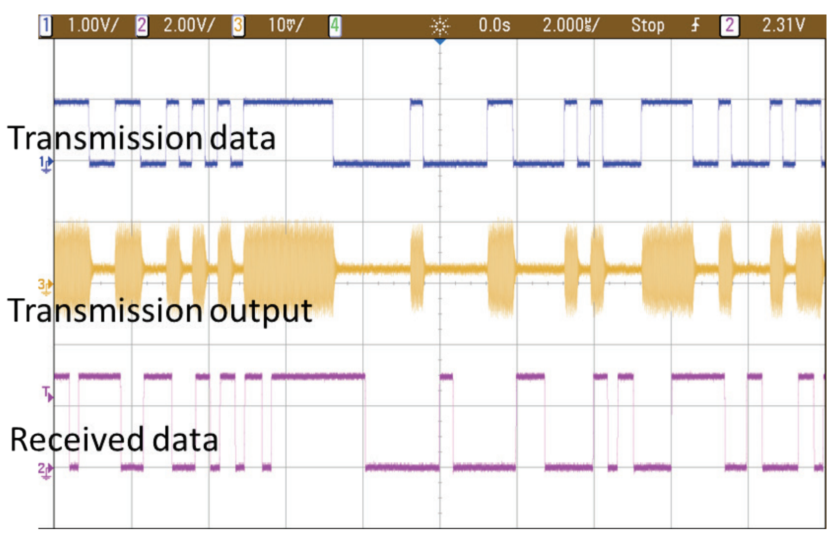

Fig. 4.23 Transient measurement of the transmitter at 3 Mbps and the received data with random numbers.

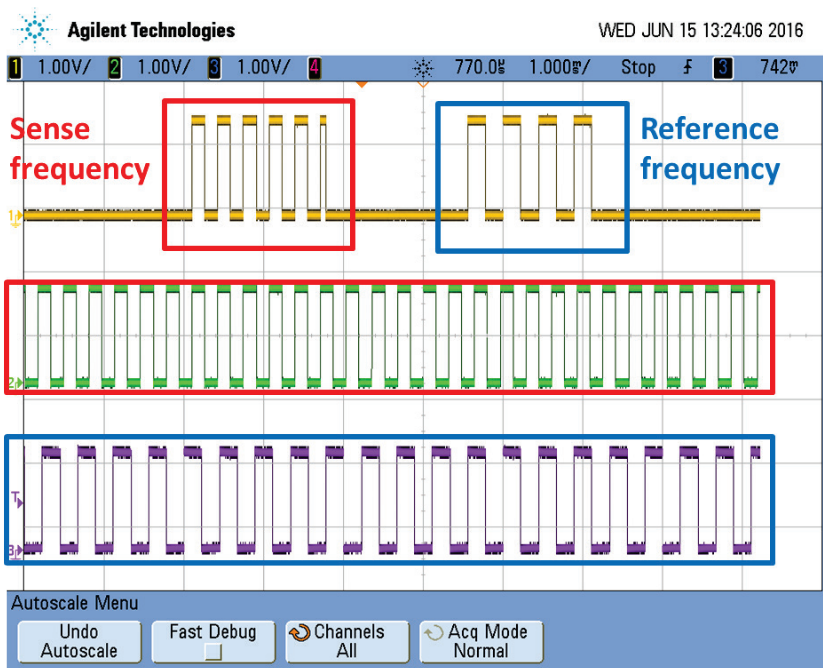

Fig. 4.24 Transient measurement of the internal I-F converter and digital blocks

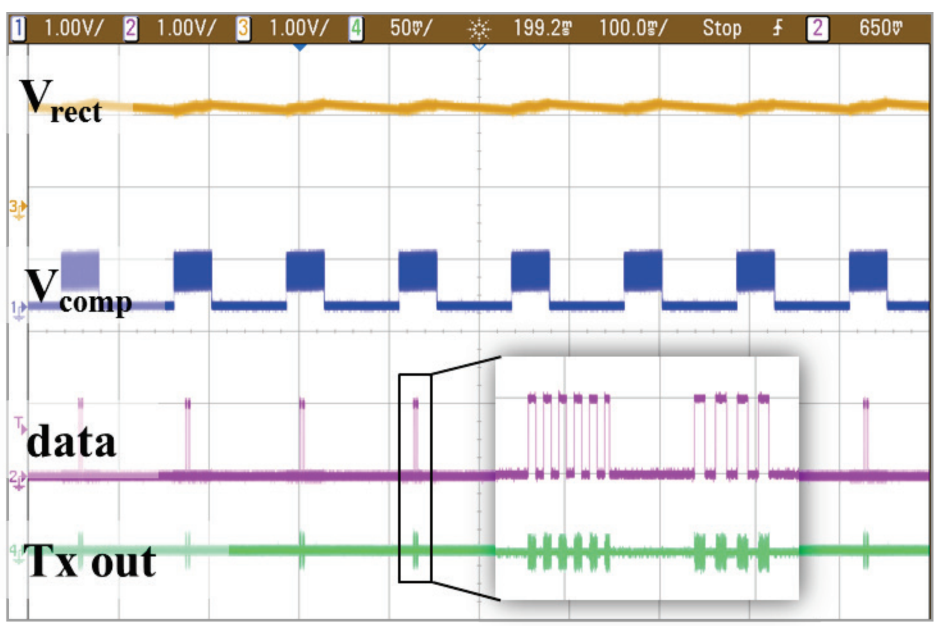

Fig. 4.25 Various transient waveforms within the chip when it is being wirelessly powered. The WPT is duty cycled to 33%. The V_{comp} waveform is trigerred when the MRC signal is present. The RF out port is terminated to 50 Ω and Tx out waveform displays the I-F converter bits are being transmitted out accordingly.

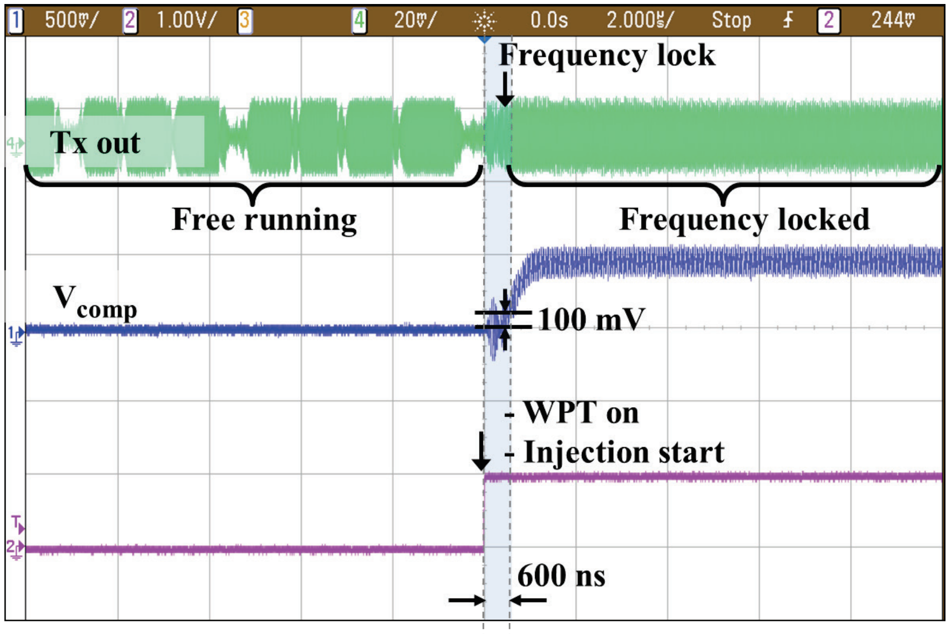

Fig. 4.26 V_{comp} trigger and locking time. V_{comp} is compared with a 100 mV reference to trigger wake-up. The locking time and trigger time is less than 600 ns.

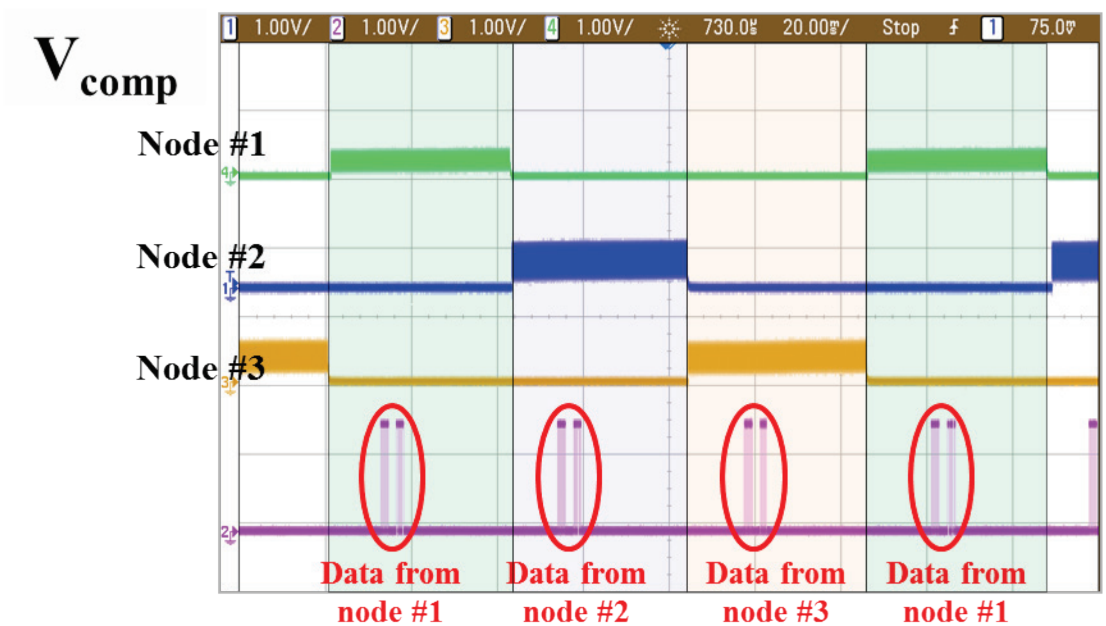

Fig. 4.27 TDMA demonstration with 3 sensor nodes. Each node is wirelessly powered selectively. V_{comp} displays the presence of WPT and its time multiplexed window. The time multiplexed window indicates which node is sending the data.

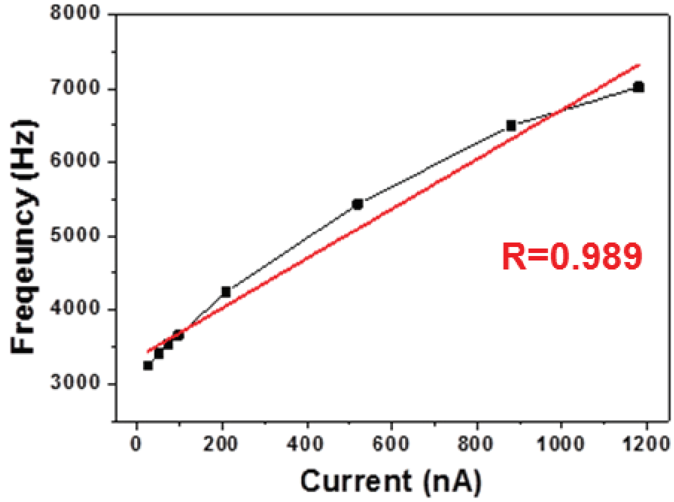

Fig. 4.28 Measured I-F converter frequency with the equivalent circuit model. Linearity calculated from 0 to 1200 nA.

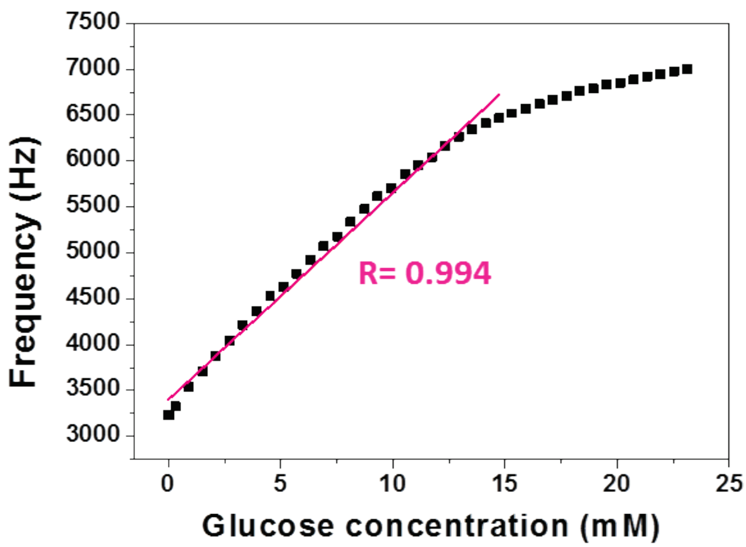

Fig. 4.29 Measured I-F converter frequency for glucose concentration in a three-electrode electrochemical cell setup. Linearity calculated from 0 to 15 mM.

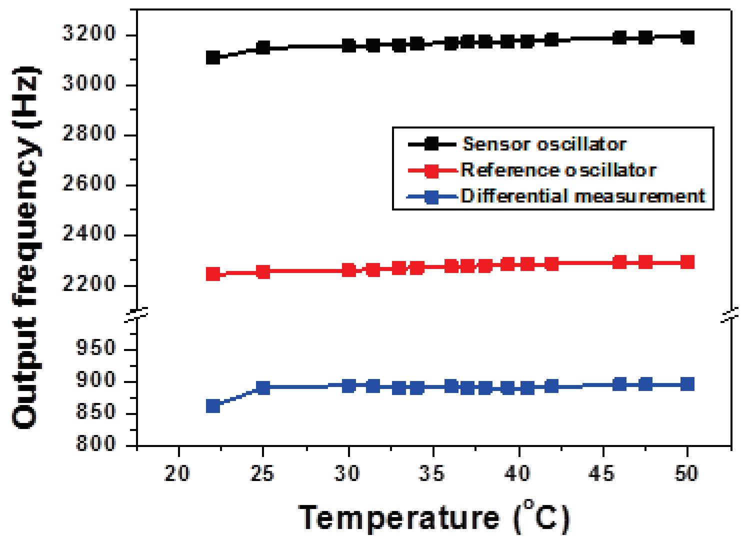

Fig. 4.30 Measured output frequency versus temperature

Fig. 4.24 illustrates the I-F conversion and the digital blocks for duty cycling. The waveforms are same as described in the previous design section, transmitting only 6% of the time. The measurement of the I-F conversion is shown in Fig. 4.28. As described in the previous section, the frequency increases with the current and the curve is linear up to approximately 1200 nA.

Fig. 4.29 shows the oscillation frequency of the I-F converter at a real glucose measurement environment, with a sensor, which will be described in chapter 5, attached to the working electrode. The linear range can be further increased with changing the surface area of the sensor. The minimum detection limit for the sensor and the chip all together is 30 μM and the sensitivity is 248 Hz/mM. These parameters can be modified by changing the size of the sensors (more current will flow with a larger sample size, hence giving higher sensitivity and more precise detection limit in sacrifice of the linear range and vice versa). In this example, the size of the sensor was determined so that the sensing range is linear up to 15mM, which is the glucose concentration range in human blood. Table 4.1 lists the key features and performance of the present work.

Table. 4.1 Performance summary of the IC

		[7]	[12]	[10]	[66]	This work
Supply voltage		Tx@0.5V & 1.0V AFE@1.2V	1V	Tx@0.56V AFE@0.9V	Tx@0.6V Rx@0.8V	Tx@1.0V AFE@1.2V
EH source		Thermal, RF	RF	RF	Non-harvest	Inductive
EH frequency		/	915 MHz	904.5 MHz	/	…20.25, 27, 40.5 MHz (ISM)
Tx frequency		402/433 MHz	2.4 GHz	402 MHz	402 MHz	405 MHz
Tx modulation		BFSK	OOK	OOK	OOK	OOK
Tx Pout		-18.5 dBm	-12.5 dBm	-18~-16 dBm	-17 dBm	-22 dBm
Multi-node		No	Yes	Yes	Yes	Yes
Crystal oscillator		Two	No	No	One	No
Power	PMU	3 µA	< 80 nA (off) 100 µA (on)	< 1 µA	/	1.8 µA
	AFE	4.8 µW	/	3.6 µW	/	4.3µW
	Tx	160 µW	380 µW	215 µW*	160 µW	231 µW 14.3 µW (duty cycled)
	Rx	/	480 µW	13 µW	180 µW	/
CMOS tech.		130 nm	90 nm	65 nm	90 nm	180 nm
Chip area		2.5×3.3 mm^2	1.4×1.1 mm^2	1×2 mm^2	> 1.2×0.9 mm^2	0.9×0.8 mm^2

4.5. Conclusion

We have designed and demonstrated a glucose readout IC that can wirelessly send out data, powered by magnetic resonance coupling. The injection frequency is 27 MHz, ISM band signal, which is used for WPT to power the entire device. A small board size of 6×15 mm^2 is made with a loop antenna as the final system. The system includes six off-chip components, where five of them were used for passive matching network and one for energy storage.

5. HIGHLY FLEXIBLE GLUCOSE BIOSENSOR BASED ON MULTILAYERED GRAPHENE PETALS

5.1. Introduction

Glucose is a key substance in human metabolism and glucose levels in blood or body fluids are closely related to critical disease and organ malfunction. To get a close study on how glucose is related to human body mechanisms, numerous efforts have been devoted to develop continuous glucose monitor (CGM) device. Additionally, it can also alert a patient at the moment when the blood sugar level is above certain point so that actions can be taken. Moreover, CGM can give feedback to an insulin pump in which it can eventually become an artificial pancreas. In order to continuously monitor glucose level in human body, the sensor has to be consistently in contact with body fluid, requiring the sensor to be either implantable or wearable. For implantable or wearable applications, there are couple factors that need to be considered.

First of all, CGM device has to be highly sensitive while maintaining small form factor and flexibility. CGM systems are mostly implantable or minimally invasive wearable applications so the sensor has to be small enough for approaches such as contact lens. Also, glucose level in interstitial fluid, tear or other body fluids are usually much lower than that in blood, thus requiring higher sensitivity.

Secondly, sufficient life span has to be guaranteed. There can be various reasons for sensor failure *in vivo* condition but we will focus mainly on the following two phenomena. One is the body response to the sensor and the other is the instability of the sensor. When a sensor is implanted, the body immediately notices awkwardness and the host responds to the foreign subject. The biofouling effect quickly debilitates the performance of the sensor. Also, mechanical damage caused by body movement and enzyme leaching are the factors to the decrease of sensitivity.

Lastly, CGM devices must be biocompatible. Either the sensor is implantable or wearable, chances of substance transfer from the sensor to body is high. Thus no toxic material should be used for the sensor.

There has been great amount of work put into CGM system research, especially in increasing device life span. Most of them have focused on increasing the device life span by applying additional polymer coating on the outer layer of the sensor surface to restrain protein adhesion, such as epoxy-enhanced polyurethane(PU) [Yu], poly(vinyl alcohol)/poly(lactic-co-glycolic acid) (PVA/PLGA) [67], poly(3,4-ethylenedioxythiophene) (PEDOT) [68] and PLGA [69]. [70] reported a glucose sensor coated with PU. The sensor was then deployed for *in vivo* testing which lasted more than a month. [67]used PVA/PLGA for protective layer and life span measurement showed above 65% of the initial performance after 30 days. Researchers of [68] electrodeposited enzyme with PEDOT and the devices were stored dry as off-the-shelf condition in between weekly tests. More than 75% of the initial sensitivity remained after a 5-week. [69] showed a glucose sensor coated with layers of PU and PLGA to enhance its life time. Results show that PLGA significantly preserved its initial performance even after 44 days in bovine serum. These researches demonstrate increased life span of glucose sensors but most of them fail to show fully flexible, highly sensitive devices. Most of them are fabricated in conventional rigid metal substrate and the extra layer of protective membrane significantly reduces the sensitivity.

In this paper, we demonstrate an all-flexible, highly-sensitive glucose sensor for miniature sized, implantable or wearable application. Most of the current biosensors are fabricated on rigid metal substrate or require laborious thin film process techniques. Once the sensor is made, it is sometimes very difficult to integrate with the system because of its physical structure. To overcome the limitations and complications in the current biosensors, we used very thin carbon fiber (CF) as the substrate material. The carbon fibers are 5 μm in diameter and these serve as the flexible base substrate for the biosensors. Then multilayered graphene petals (MGP) are directly deposited on the CF through a chemical vapor deposition method. The MGPs greatly enhance the surface area and provide highly conductive template for Pt nanoparticle electrodeposition.

Additionally, the unique shape of the MGPs minimizes enzyme leaching from the electrode, therefore leading to increased life time of the devices. The Pt nanoparticles (PtNP), well known for their catalytic behavior, are electrodeposited onto the edges and planes of the graphene petals to increase the electrochemical performance. A thin polyaniline (PANI) nanofiber polymer layer is deposited on the PtNP/MGP surface for enzyme immobilization. Polyaniline (PANI) is chosen for the polymer material for its high surface area, porosity and high electrical conductivity [71, 72]. The porous structure of the PANI nanofibers favor a high density of enzyme immobilization [73] and it is reported that excess enzyme can maintain the sensor's sensitivity, leading to an increase in lifetime. The PANI layer is thin enough so that the petal like structure of graphene is preserved. The petal structure acts as an encapsulating structure to prevent enzyme leaching. In this work, flexible CF/GP/PtNP/PANI-GOx electrodes are fabricated and its performance was measured in PBS. The GP-PtNP glucose sensors show excellent sensitivity and retained most of its initial sensitivity even after 5 weeks of use with minimal effects from interfering substances. The electrode is optionally coated with polyurethane for longer device life span.

5.2. Results

5.2.1. Multilayered graphene petals on carbon fiber

Diameter of 5 μm carbon fiber tow was used as the base substrate material. A microwave plasma chemical vapor deposition (MPCVD) process was used to grow the graphene on the bundle of carbon fibers and the procedures are described in [74]. MPCVD was operated with 700 W at a pressure of 30 Torr under H_2 and CH_4 maintained at 50 and 10 sccm, respectively. The petals protrude out from the surface of the carbon fiber approximately 300 nm and the thickness of the GP plane ranges from 1 nm to 15 nm, indicating less than 50 graphene layers. Carbon and graphene are hydrophobic in nature and to use them as electrodes, acidic treatment has been applied for functionalization.

Raman spectroscopy is an effective method for characterizing carbon based materials. The D band at 1350 cm^{-1} indicates various defects and anomalies. The G peak at 1580 cm^{-1} is due to the doubly degenerate zone center E_{2g} mode [75]. It can be seen that the D peak increased after the functionalization, indicating increased number of defects and oxygenated species on the graphene layers [76]. The PtNP deposition does not show significant change in Raman spectroscopy. Several new peaks appear after PANI deposition. The peaks at 800 cm^{-1} are assigned to the out-of-plane C-H bending of the quinoid ring and the peaks at 1500, 1166, 1420 cm^{-1} mainly originate from C and N or C and H bonds [77].

As an effort to render additional electroactiveness toward H_2O_2 oxidaiton[68, 78], Pt nanoparticles are deposited on the surface of the GPs (Fig. 5.3). The edge-line of the petals are almost entirely covered with Pt and the inner faces of the petals are covered with arrays of Pt nanoparticles (<20nm). These Pt nanoparticles have significant effect on H_2O_2 and glucose sensing. Amperometric measurement was performed by a three electrode electrochemical cell and the results show that electro-reactivity toward H_2O_2 increased approximately 100 folds after Pt nanoparticle deposition.

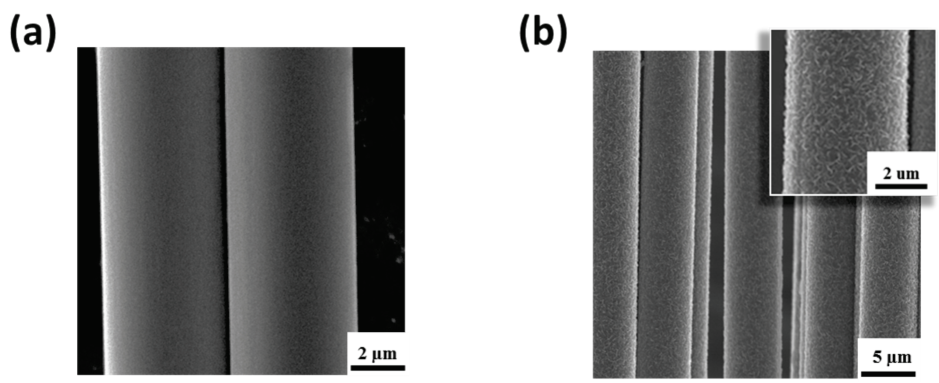

Fig. 5.1 SEM images of (a) bare carbon fiber and (b) graphene petals on carbon fiber

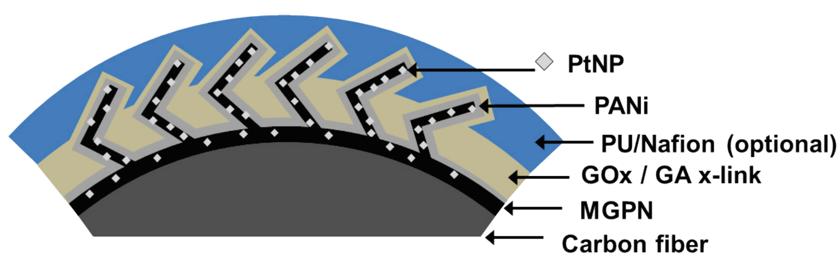

Fig. 5.2 Layers of the present work

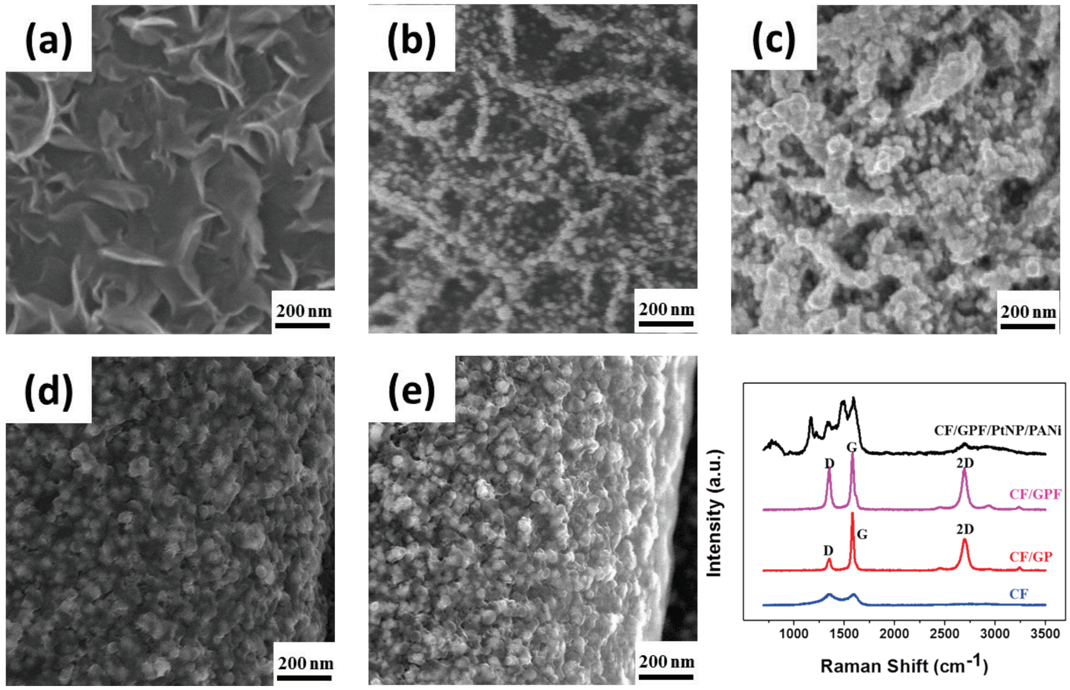

Fig. 5.3 SEM images of (a) graphene petals, (b) PtNP on graphene petals, (c) PANI electro-polymerized on GP/PtNP, (d) GOx crosslinked with glutaraldehyde on GP/PtNP/GOx, (e) PU coated on GP/PtNP/GOx/PU and (f) Raman spectroscopy of some of the materials.

5.2.2. Enzyme immobilization and glucose sensing

To make a glucose sensor, the GOx enzyme is immobilized onto the electrode. But first, a thin layer of PANI is deposited on to the CF/GP/PtNP electrode. Because of PANI's characteristics of porous nanofiber-like structure, biocompatibility and high conductivity [79], it serves as an adequate active-surface for enzyme immobilization. The thickness of the PANI is made smaller than 50 nm so that the large surface of GPs is fully utilized, thus providing a highly porous morphology (Fig. 5.3(c)) for enzyme immobilization that ultimately leads to an increase in sensor lifetime, stability and fast response [80]. Excess enzyme has been used to minimize the effect of enzyme activity loss [81] and the enzyme has been cross-linked on to the PANI layer with glutaraldehyde.

The electrochemical glucose sensing is determined by measuring the anodic current of oxidation of H_2O_2, produced by the enzymatic activity (5.1), (5.2).

$$\mathrm{D-glucose} + O_2 + H_2O \xrightarrow{GO_x} \mathrm{D-gluconic\ acid} + H_2O_2 \tag{5.1}$$

$$H_2O_2 \rightarrow 2H^+ + O_2 + 2e^- \tag{5.2}$$

The amperometric glucose sensing measurement setup is similar to the H_2O_2 test, described previously, and a working potential of 500mV was applied. Figure 5.4 displays a typical amperometric response of the glucose sensor with addition of successive aliquots of increasing concentrations of glucose in 1x PBS at room temperature. The glucose sensor performs a rapid step response to the injections of glucose aliquots and reaches a steady-state value within 5 seconds. The amperometric glucose calibration plot (Fig. 5.5) exhibits linear sensing range from 0 mM to 66 mM with the correlation coefficient R of 0.996. The sensitivity, detection limit (signal to noise ratio of 3) and the sensing range of the glucose sensor is summarized and compared to glucose sensors comprised of similar materials in Table 5.1.

To our knowledge, the sensing range of the CF/GP/PtNP/PANI-GOx biosensor is wider than any biosensors reported in literature. The wide sensing range of the biosensor enables detecting glucose level in any body fluid including blood, saliva, urine and sweat. Together with the flexibility of the materials comprising the biosensor and robustness of graphene, this present work it is highly suitable for wearable or implantable applications which opens possibilities for new non-invasive glucose sensing applications where various human serums can be continuously monitored.

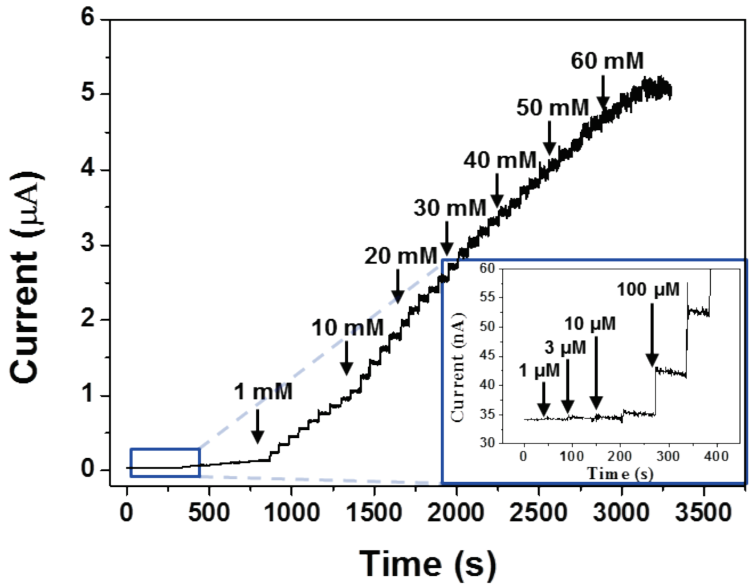

Fig. 5.4 Amperometric measurement with addition of glucose in PBS 1x solution.

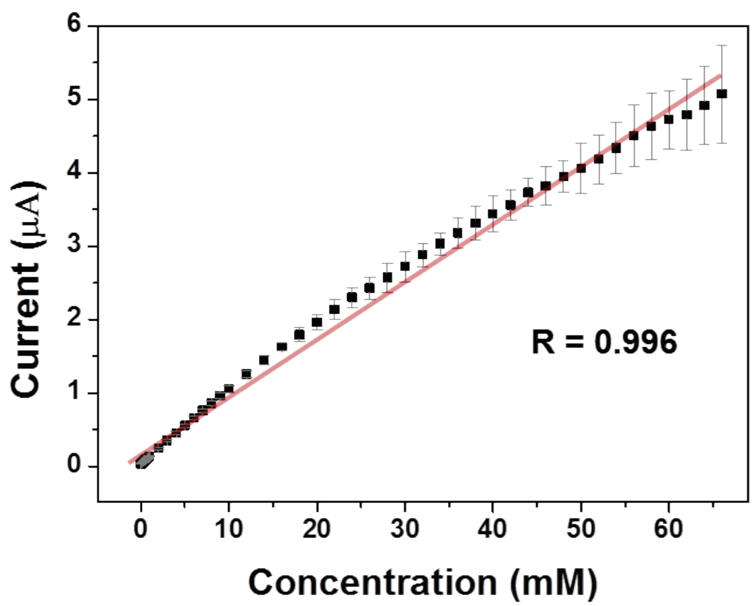

Fig. 5.5 Calibration curve.

Table. 5.1 Comparison of state-of-the-art glucose biosensors

Base Materials	**Substrate**	**Detection limit (µM)**	**Sensing range (mM)**	**Sensitivity ($\mu AmM^{-1}cm^{-2}$)**	**Reference**
GOx-PANI/PtNP/graphene	Carbon fiber	2	0.002-66	5.67	This work
GOx-PB/PtNP/graphene-hybrid	PDMS	10	0.01-0.7	1.0	[82]
GOx/PtNP/graphene	Glass	0.5	0.05-1	580	[83]
GOx/PB	Tattoo	3	0.003-0.1	23	[84]
GOx/MWCNT	GCE	5	0.005-2.5	2.8	[85]
GOx-PEDOT/PtNP/graphene	Silicon	0.3	0.01-50	0.65	[68]

5.2.3. Device lifetime and flexibility

The stability of the GP/PANI/GOx structure has been validated by performing a sensitivity test in every 3-4 days. Sensitivity of the biosensor was measured in glucose levels between 0 mM to 10 mM. The sensors were kept in PBS (pH: 7.4) in between tests at room temperature and the solution was renewed every day to prevent possible contamination. The sensitivity of the GP/PtNP/PANI-GOx sensor increases initially and then reaches a stable value which remains for over 5 weeks, showing robust enzyme immobilization on the petal morphology.

The mechanical flexibility and robustness of the biosensor was confirmed by performing a bend test. The CF/GP/PtNP/PANI-GOx sensor was mechanically bent and subsequently released to its initial form while conducting an amperometric glucose measurement. The fiber tows were bent in 90° and 30° angle while measuring the glucose concentration of 1mM (Fig 5.6). It is shown that the current decreases less than 10% of its initial value while bent 90° and quickly goes back to its original steady-state value when it returns to its initial form. The biosensor shows less decrease of current when it is bent 30°. After the biosensor returns to its original shape, the measurement went back to its stable state. Also, the biosensor went through a series of bending test for more than 500 times and showed no noticeable decrease in sensitivity.

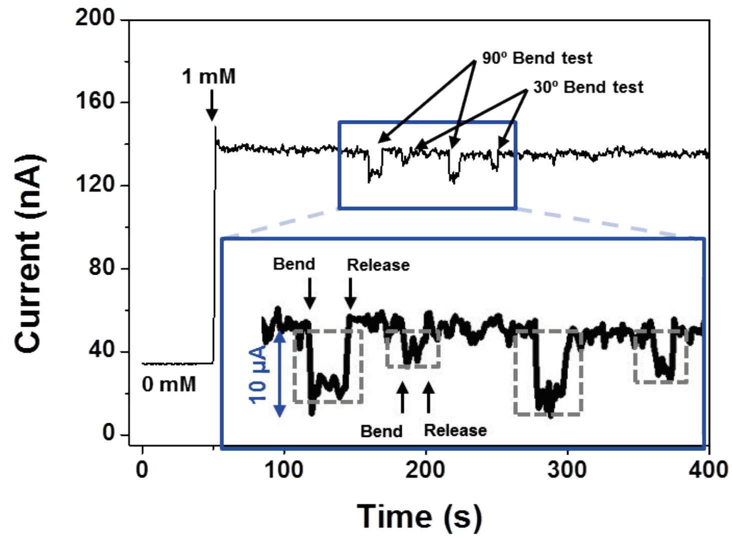

Fig. 5.6 Bend test.

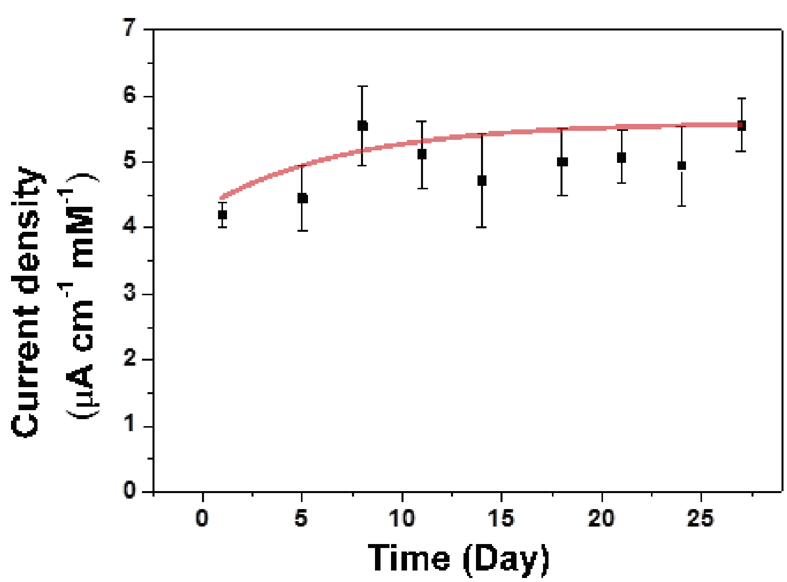

Fig. 5.7 Life time and sensitivity of the biosensor

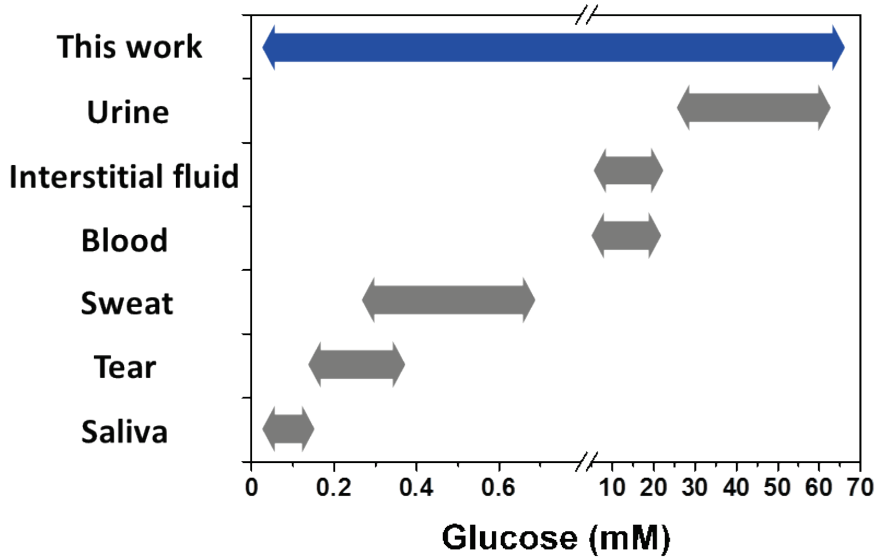

Fig. 5.8 Sensing range of this biosensor and the glucose concentration level in various body fluids.

5.3. Conclusion

We have demonstrated a highly flexible biosensor for implantable or wearable application using graphene petals on a carbon fiber tow. The carbon fiber tows with graphene petals act as the flexible substrate material for the sensor and most of the layers, including PtNP, PANI and GOx, are buried within the graphene petals, fully utilizing the robust mechanical nature of graphene. A factor on robustness toward flexibility has been tested which shows reliable results over time and stress. Our work also shows long lifetime and wide sensing range toward glucose, showing a suitable candidate for continuous monitoring systems for various body fluids (Fig 5.8) [82, 86-89].

On a fabrication point of view, our work involves no complicated array fabrication protocol or semiconductor process and most of the work can be done electrochemically. Graphene can be grown on more than 6000 carbon fiber tows at a time and the high sensitivity of the biosensor opens up a potential for mass production.

5.4. Experimental section

Graphene petals were grown on the carbon fiber tow by microwave plasma chemical vapor deposition (MPCVD) with a SEKI AX200S following method described in our previous work [68, 74]. The carbon fiber tows are elevated by two ceramic stands on a molybdenum puck inside the MPCVD chamber. The chamber is evacuated to base pressure of 2 Torr and then while H_2 and CH_4 were maintained at 50 and 10 sccm, respectively, the pressure of the chamber was allowed to reach 30 Torr. The microwave plasma at an excitation frequency of 2.45 GHz is then ignited at 700 W. The microwave plasma was maintained for 15 minutes to permit multilayered graphene petal growth across the entire carbon fiber tow (Figure 1). Further acidic treatment was applied to the CF/GPs for functionalization.

A three-electrode electrochemical setup is used, similar to the previous measurement setup where the CF/GP acts as the working electrode, Ag/AgCl as the reference electrode and Pt gauze as the counter electrode. The electrodes were dipped in a Pt plating solution consisting of $H_2PtCl_6{\cdot}6H_2O$ (4mM, Sigma Aldrich, 206083) and Na_2SO_4 (0.5M, Sigma Aldrich, 71959) to electrodeposit the nanoparticles onto the CF/GP electrodes. 300 cycles of voltage pulses (0.5 V, 200 ms) were applied to the CF/GP electrode. After electrodeposition, the sample was thoroughly washed in deionized water.

Electropolymerization was conducted on the CF/GP electrode with the similar setup as described previously but with a solution containing aniline monomers (0.05 M) and H_2SO_4 (0.5 M). Constant DC voltage of 0.8 V was applied between the working electrode and reference electrode for 5 minutes. The sharp edges of the graphene petals remained its shape after the PANI decoration. The electropolymerizied sample was then soaked in deionized water to remove all the debris of PANI.

Enzyme solution containing 10 mg/mL (150 unit/mL, Sigma Aldrich, G7141) was prepared in PBS (0.01M, PH=7.4) for immobilization of glucose oxidase. The electrode was dipped in the enzyme solution for 2 hours to let the enzyme absorb into PANI layer. The electrode was then taken out of the solution and rinsed with PBS to remove residues. Then the electrode was dipped vertically, in a vial containing 20 μl glutaraldehyde (0.1%, Sigma Aldrich, 340855). The GOx were cross-linked for 3 hours and after that the electrode was rinsed again in PBS. The electrode is optionally coated with Nafion to block any anion interferences such as uric acid or ascorbic acid.

All electrochemical experiments were performed in a three-electrode setup (BASi Epsilon Three-electrode Cell) where GP/PtNP/PANI-GOx electrode acted as the working electrode, Ag/AgCl electrode as the reference and Pt gauze as the counter electrode. Amperometric measurement was performed in a 0.01M PBS solution (10mL) at a working potential of 500 mV with a stirrer spinning at 500 rpm. Around 20 CF/GP/PtNP/PANI-GOx electrodes (length 15mm) were used at a time to create a sample. To form an electrical contact, they were connected to a copper strap with silver paste and the interconnection part was insulated with an acid resistant lacquer and polydimethylsiloxane (PDMS). The electrode was then submerged in the aqueous solution for measurement. The sensitivity was calculated based on the number of fiber electrodes and length.

S-4800 (Hitachi) was used for all the field emission scanning electron microscopy (FESEM) micrographs. The power was set to 5.0 kV and no preparation was required before image analysis.

Raman spectroscopy was performed using Xplora confocal Raman microscope by Horiba Jobin Yvon. All the spectra were collected at room with laser wavelength of 532 nm. The laser power was 1.3 mW with 100× objective lens.

6. SUMMARY AND FUTURE WORK

6.1. Summary

This thesis showed two core technologies enabling wireless implantable sensor networks for smart healthcare in the future: low power IC and the wireless power transfer for multiple nodes and implementation of a miniature implantable biosensor.

Two different WPT techniques using the RF radiation and inductive coupling have been demonstrated. The most power hungry block in the wireless sensor network IC, which is the transmitter, has been intensively studied and a low power design is implemented to minimize the power consumption of the entire system. An automated WPT method for dynamic environment has been proposed and demonstrated for multiple node system. To pair with the electronics of a system, a miniature glucose sensor has been fabricated using graphene petals on carbon fiber tow. The biosensor showed high flexibility with good sensitivity and lifetime.

The IC, wireless power transfer technique and the biosensor together compose the implantable wireless glucose sensor.

6.2. Future work

Based on the techniques demonstrated in this paper, future work can be done on device packaging. Currently, the work demonstrated in this paper is presented on a PCB level but further miniaturization is possible with flip-chip packaging and ultimately, the final device packaging substrate should be something flexible and biocompatible, such as parylene or PDMS.

Also, the coil for the WPT can be miniaturized using thin film process. Some of the work has been demonstrated but a system level packaging still remains as future work.

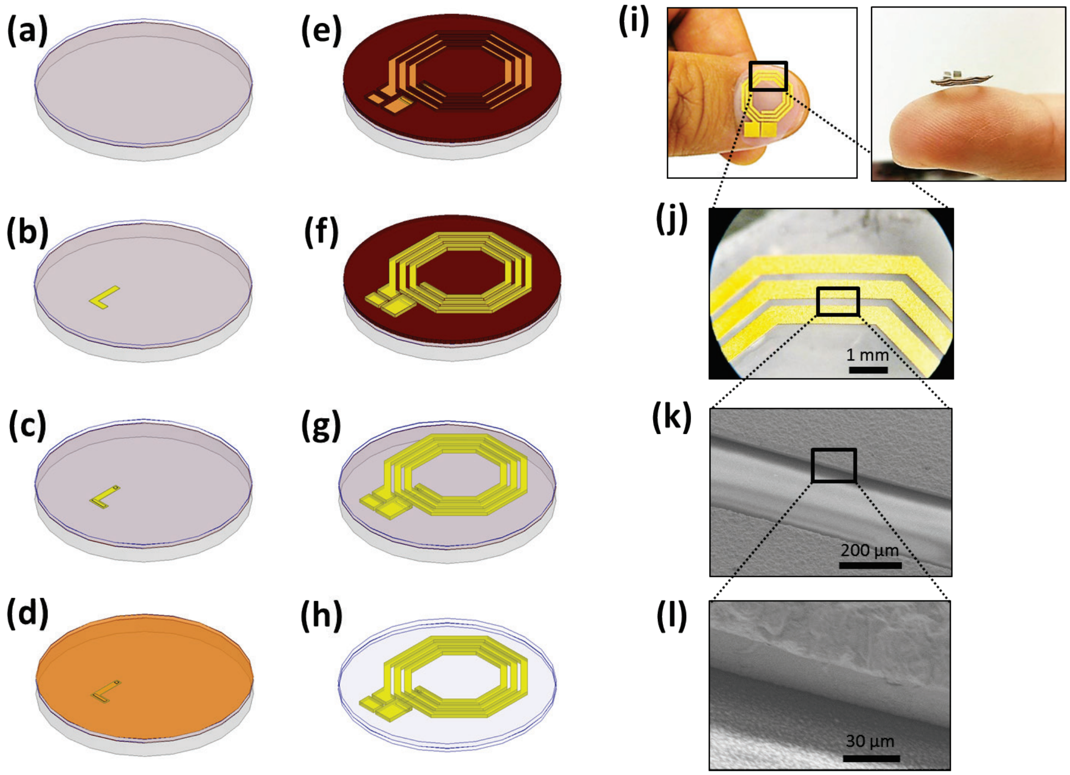

Fig. 6.1 Fabrication process of the WPT coil on parylene [58]. (a–h) Contact lens platform fabrication process. (a) Deposition of sacrificial PR and parylene-C film on Si carrier wafer. (b) Formation of first metal layer. (c) Deposition of parylene insulating layer and formation of via-holes. (d) Deposition of seed metal layer. (e) Thick PR masking. (f) Electroplating of second metal layer. (g) PR strip and seed metal etching. (h) Package releasing from carrier wafer. (i) Photo images of fabricated device before (left) and after (right) heat molding. (j–l) Photo images of fabricated device viewed in different magnifications

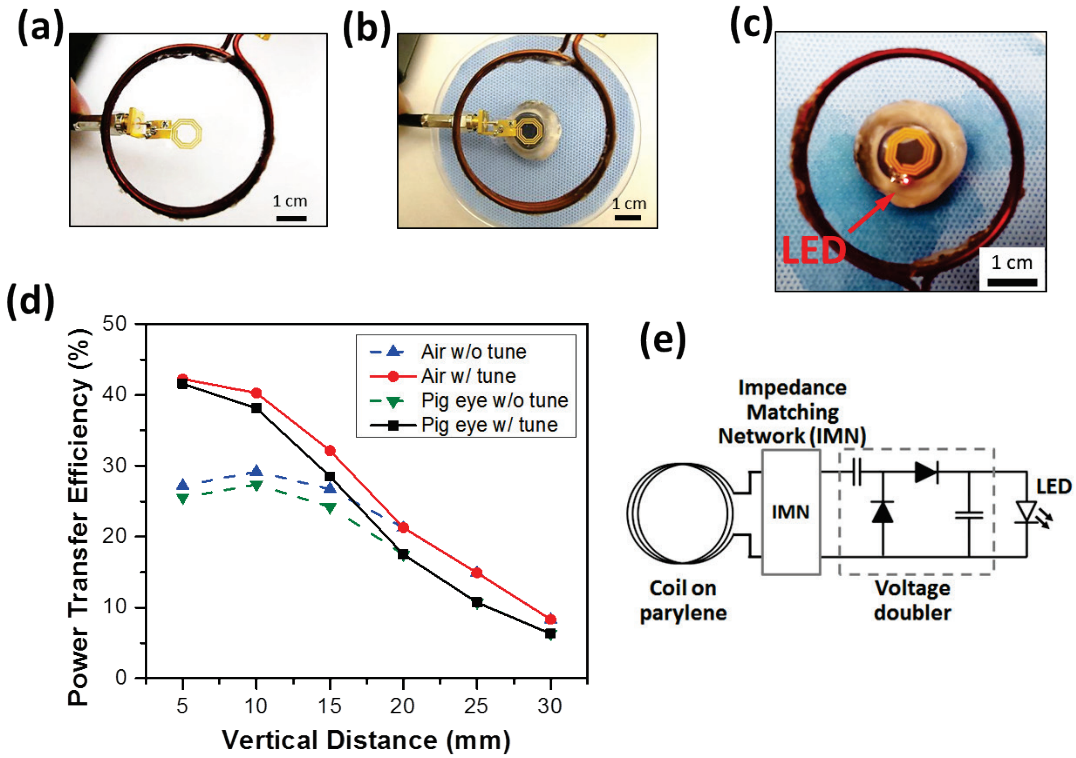

Fig. 6.2 Measurement setup and power efficiency with a pig eye [58]. Measurement of power transfer to parylene contact lens platform. (a) PTE measurement setup in air. (b) PTE measurement setup on pig eye. (c) Wireless powering demonstrated on pig eye with red LED illumination. (d) Measured PTE results in air and on pig eye. In both cases, measurements are performed with and without compensation for distance variation. (e) Schematic of a rectifier and an LED integrated into the parylene contact lens platform to demonstrate energy harvesting scenario On the electronics side, the power consumption of the IC can be improved by using a better process technology. Also the receiver part of the system can be miniaturized so that the user can check their biosignals from their implant devices with a portable device.

LIST OF REFERENCES

LIST OF REFERENCES

[1] M. Patel and W. Jianfeng, "Applications, challenges, and prospective in emerging body area networking technologies," Wireless Communications, IEEE, vol. 17, pp. 80-88, 2010.

[2] E. Y. Chow, Y. Chin-Lung, O. Yuehui, A. L. Chlebowski, P. P. Irazoqui, and W. J. Chappell, "Wireless powering and the study of RF propagation through ocular tissue for development of implantable sensors," Antennas and Propagation, IEEE Transactions on, vol. 59, pp. 2379-2387, 2011.

[3] A. K. RamRakhyani, S. Mirabbasi, and M. Chiao, "Design and optimization of resonance-based efficient wireless power delivery systems for biomedical implants," Biomedical Circuits and Systems, IEEE Transactions on, vol. 5, pp. 48-63, 2011.

[4] J. Jang, D. F. Berdy, J. Lee, D. Peroulis, and B. Jung, "A wireless condition monitoring system powered by a sub-100 /spl mu/W vibration energy harvester," Circuits and Systems I: Regular Papers, IEEE Transactions on, vol. 60, pp. 1082-1093, 2013.

[5] N. J. Guilar, R. Amirtharajah, and P. J. Hurst, "A full-wave rectifier with integrated peak selection for multiple electrode piezoelectric energy harvesters," Solid-State Circuits, IEEE Journal of, vol. 44, pp. 240-246, 2009.

[6] G. Chen, M. Fojtik, K. Daeyeon, D. Fick, P. Junsun, S. Mingoo, et al., "Millimeter-scale nearly perpetual sensor system with stacked battery and solar cells," in Solid-State Circuits Conference Digest of Technical Papers (ISSCC), 2010 IEEE International, 2010, pp. 288-289.

[7] F. Zhang, Y. Zhang, J. Silver, Y. Shakhsheer, M. Nagaraju, A. Klinefelter, et al., "A batteryless 19 μW MICS/ISM-band energy harvesting body area sensor node SoC," in Solid-State Circuits Conference Digest of Technical Papers (ISSCC), 2012 IEEE International, 2012, pp. 298-300.

[8] J. Pandey and B. P. Otis, "A sub-100 W MICS/ISM band transmitter based on injection-locking and frequency multiplication," Solid-State Circuits, IEEE Journal of, vol. 46, pp. 1049-1058, 2011.

[9] US Federal Communications Commission, "Evaluating Compliance with FCC-Specified Guidelines for Human Exposure To Radio Frequency Radiation," vol. OET Bulletin 65, ed. Washington DC, 1997.

[10] L. Xia, J. Cheng, N. E. Glover, and P. Chiang, "0.56 V, -20 dBm RF-powered, multi-node wireless body area network system-on-a-chip with harvesting-efficiency tracking loop," Solid-State Circuits, IEEE Journal of, vol. 49, pp. 1345-1355, 2014.

[11] F. Zhang, M. A. Stoneback, and B. P. Otis, "A 23 μA RF-powered transmitter for biomedical applications," in Radio Frequency Integrated Circuits Symposium (RFIC), 2011 IEEE, 2011, pp. 1-4.

[12] G. Papotto, F. Carrara, A. Finocchiaro, and G. Palmisano, "A 90-nm CMOS 5-Mbps crystal-less RF-powered transceiver for wireless sensor network nodes," Solid-State Circuits, IEEE Journal of, vol. 49, pp. 335-346, 2014.

[13] M. Vidojkovic, X. Huang, P. Harpe, S. Rampu, C. Zhou, H. Li, et al., "A 2.4GHz ULP OOK single-chip transceiver for healthcare applications," in Solid-State Circuits Conference Digest of Technical Papers (ISSCC), 2011 IEEE International, 2011, pp. 458-460.

[14] R. J. Cameron, C. M. Kudsia, and R. R. Mansour, Microwave filters for communication systems: Wiley-Interscience, 2007.

[15] D. Ha, T.-C. Lee, D. J. Webery, and W. J. Chappell, "Power distribution to multiple implanted sensor devices using a multiport bandpass filter (BPF) approach," in Microwave Symposium (IMS), 2014 IEEE MTT-S International, 2014, pp. 1-4.

[16] M. R. Yuce, "Implementation of wireless body area networks for healthcare systems," Sensors and Actuators A: Physical, vol. 162, pp. 116-129, 2010.

[17] T. A. Kuiken, G. Li, B. A. Lock, and et al., "Targeted muscle reinnervation for real-time myoelectric control of multifunction artificial arms," JAMA, vol. 301, pp. 619-628, 2009.

[18] M. M. Lowery, N. S. Stoykov, and T. A. Kuiken, "Independence of myoelectric control signals examined using a surface EMG model," Biomedical Engineering, IEEE Transactions on, vol. 50, pp. 789-793, 2003.

[19] D. McDonnall, S. Hiatt, C. Smith, and K. S. Guillory, "Implantable multichannel wireless electromyography for prosthesis control," in Engineering in Medicine and Biology Society (EMBC), 2012 Annual International Conference of the IEEE, 2012, pp. 1350-1353.

[20] R. A. Bercich, J. Joseph, O. Z. Gall, J. Maeng, Y.-J. Kim, and P. P. Irazoqui, "Implantable device for intramuscular myoelectric signal recording," in The 34th Annual International Conference of the IEEE Engineering in Medicine and Biology Society, 2012.

[21] K. E. Koh, T. C. Beh, T. Imura, and Y. Hori, "Impedance matching and power division using impedance inverter for wireless power transfer via magnetic resonant coupling," Industry Applications, IEEE Transactions on, vol. 50, pp. 2061-2070, 2014.

[22] J. Yin, J. Yi, M. K. Law, Y. Ling, M. C. Lee, K. P. Ng, et al., "A system-on-chip EPC Gen-2 passive UHF RFID tag with embedded temperature sensor," Solid-State Circuits, IEEE Journal of, vol. 45, pp. 2404-2420, 2010.

[23] C.-Y. Yao and W.-C. Hsia, "A –21.2-dBm dual-channel UHF passive CMOS RFID tag design," Circuits and Systems I: Regular Papers, IEEE Transactions on, vol. 61, pp. 1269-1279, 2014.

[24] R. Muller, H. P. Le, W. Li, P. Ledochowitsch, S. Gambini, T. Bjorninen, et al., "24.1 A miniaturized 64-channel 225μW wireless electrocorticographic neural sensor," in 2014 IEEE International Solid-State Circuits Conference Digest of Technical Papers (ISSCC), 2014, pp. 412-413.

[25] D. Zhiming and A. M. Niknejad, "The speed-power trade-off in the design of CMOS true-single-phase-clock dividers," Solid-State Circuits, IEEE Journal of, vol. 45, pp. 2457-2465, 2010.

[26] X. Sun, C. Zhang, Y. Li, Z. Wang, and H. Chen, "Design of several key circuits of UHF passive RFID tag," China Integrated Circuit, vol. 16, 2007.

[27] H. Banba, H. Shiga, A. Umezawa, T. Miyaba, T. Tanzawa, S. Atsumi, et al., "A CMOS bandgap reference circuit with sub-1-V operation," Solid-State Circuits, IEEE Journal of, vol. 34, pp. 670-674, 1999.

[28] A. P. Chandrakasan, N. Verma, and D. C. Daly, "Ultralow-power electronics for biomedical applications," Annu. Rev. Biomed. Eng., vol. 10, pp. 247-274, 2008.

[29] R. A. Bercich, D. R. Duffy, and P. P. Irazoqui, "Far-field RF powering of implantable devices: safety considerations," Biomedical Engineering, IEEE Transactions on, vol. 60, pp. 2107-2112, 2013.

[30] H. S. Bhamra, Y.-J. Kim, J. Joseph, J. Lynch, O. Gall, H. Mei, et al., "A 24 μW, Batteryless, Crystal-free, Multi-node Synchronized SoC "Bionode" for Wireless Prosthesis Control," Solid-State Circuits, IEEE Journal of, 2015.

[31] J. Masuch, M. Delgado-Restituto, D. Milosevic, and P. Baltus, "Co-integration of an RF energy harvester into a 2.4 GHz transceiver," Solid-State Circuits, IEEE Journal of, vol. 48, pp. 1565-1574, 2013.

[32] H. Shoki, "Issues and initiatives for practical use of wireless power transmission technologies in Japan," in Microwave Workshop Series on Innovative Wireless Power Transmission: Technologies, Systems, and Applications (IMWS), 2011 IEEE MTT-S International, 2011, pp. 87-90.

[33] G. L. Cote, R. M. Lec, and M. V. Pishko, "Emerging biomedical sensing technologies and their applications," Sensors Journal, IEEE, vol. 3, pp. 251-266, 2003.

[34] L. Mateu and F. Moll, "Review of energy harvesting techniques and applications for microelectronics (Keynote Address)," in Microtechnologies for the New Millennium 2005, 2005, pp. 359-373.

[35] D. Ahn and S. Hong, "Wireless power transmission with self-regulated output voltage for biomedical implant," Industrial Electronics, IEEE Transactions on, vol. 61, pp. 2225-2235, 2014.

[36] A. Kurs, A. Karalis, R. Moffatt, J. D. Joannopoulos, P. Fisher, and M. Soljačić, "Wireless power transfer via strongly coupled magnetic resonances," Science, vol. 317, pp. 83-86, 2007.

[37] D. Ahn and S. Hong, "Effect of coupling between multiple transmitters or multiple receivers on wireless power transfer," Industrial Electronics, IEEE Transactions on, vol. 60, pp. 2602-2613, 2013.

[38] J. J. Casanova, L. Zhen Ning, and L. Jenshan, "A loosely coupled planar wireless power system for multiple receivers," Industrial Electronics, IEEE Transactions on, vol. 56, pp. 3060-3068, 2009.

[39] Y. Zhang, T. Lu, Z. Zhao, F. He, K. Chen, and L. Yuan, "Selective wireless power transfer to multiple loads using receivers of different resonant frequencie," Power Electronics, IEEE Transactions on, vol. PP, pp. 1-1, 2014.

[40] J. Lee, Y.-S. Lim, W.-J. Yang, and S.-O. Lim, "Wireless power transfer system adaptive to change in coil separation," Antennas and Propagation, IEEE Transactions on, vol. 62, pp. 889-897, 2014.

[41] A. P. Sample, D. A. Meyer, and J. R. Smith, "Analysis, experimental results, and range adaptation of magnetically coupled resonators for wireless power transfer," Industrial Electronics, IEEE Transactions on, vol. 58, pp. 544-554, 2011.

[42] I. Awai and T. Ishizaki, "Superiority of BPF theory for design of coupled resonator WPT systems," in Microwave Conference Proceedings (APMC), 2011 Asia-Pacific, 2011, pp. 1889-1892.

[43] J. H. Jang, D. F. Berdy, J. Lee, D. Peroulis, and B. Jung, "A wireless sensor node for condition monitoring powered by a vibration energy harvester," in Custom Integrated Circuits Conference (CICC), 2011 IEEE, 2011, pp. 1-4.

[44] A. Yakovlev, D. Pivonka, T. Meng, and A. Poon, "A mm-sized wirelessly powered and remotely controlled locomotive implantable device," in Solid-State Circuits Conference Digest of Technical Papers (ISSCC), 2012 IEEE International, 2012, pp. 302-304.

[45] S. B. Cohn, "Dissipation loss in multiple-coupled-resonator filters," Proceedings of the IRE, vol. 47, pp. 1342-1348, 1959.

[46] D. M. Pozar, Microwave engineering: John Wiley & Sons, 2009.

[47] J.-S. G. Hong and M. J. Lancaster, Microstrip filters for RF/microwave applications vol. 167: John Wiley & Sons, 2004.

[48] G. L. Matthaei, L. Young, and E. M. T. Jones, Microwave filters, impedance-matching networks, and coupling structures: McGraw-Hill, 1964.

[49] S. Hui, W. Zhong, and C. Lee, "A critical review of recent progress in mid-range wireless power transfer," Power Electronics, IEEE Transactions on, vol. 29, pp. 4500-4511, 2014.

[50] B. Teck Chuan, M. Kato, T. Imura, O. Sehoon, and Y. Hori, "Automated impedance matching system for robust wireless power transfer via magnetic resonance coupling," Industrial Electronics, IEEE Transactions on, vol. 60, pp. 3689-3698, 2013.

[51] D. Ha, W. N. de Vries, S. W. John, P. P. Irazoqui, and W. J. Chappell, "Polymer-based miniature flexible capacitive pressure sensor for intraocular pressure (IOP) monitoring inside a mouse eye," Biomedical microdevices, vol. 14, pp. 207-215, 2012.

[52] L. Bu, P. Cong, H.-I. Kuo, X. Ye, and W. Ko, "Micro package of short term wireless implantable microfabricated systems," in Engineering in Medicine and Biology Society, 2009. EMBC 2009. Annual International Conference of the IEEE, 2009, pp. 6395-6399.

[53] S. Gabriel, R. Lau, and C. Gabriel, "The dielectric properties of biological tissues: III. Parametric models for the dielectric spectrum of tissues," Physics in medicine and biology, vol. 41, p. 2271, 1996.

[54] E. Jovanov, "Wireless technology and system integration in body area networks for m-health applications," in Proceedings of the 27th Annual International Conference of the IEEE Engineering in Medicine and Biology Society, Shanghai, China, 2005.

[55] T. Karacolak, A. Z. Hood, and E. Topsakal, "Design of a dual-band implantable antenna and development of skin mimicking gels for continuous glucose monitoring," IEEE Transactions on Microwave Theory and Techniques, vol. 56, pp. 1001-1008, 2008.

[56] C. Liu, Y.-X. Guo, and S. Xiao, "Compact dual-band antenna for implantable devices," IEEE Antennas and Wireless Propagation Letters, vol. 11, pp. 1508-1511, 2012.

[57] Y.-J. Kim, D. Ha, W. J. Chappell, and P. P. Irazoqui, "Selective Wireless Power Transfer for Smart Power Distribution in a Miniature-Sized Multiple-Receiver System," IEEE Transactions on Industrial Electronics, vol. 63, pp. 1853-1862, 2016.

[58] Y.-J. Kim, J. Maeng, and P. P. Irazoqui, "Eyeglasses-powered, contact lens-like platform with high power transfer efficiency," Biomedical microdevices, vol. 17, pp. 1-9, 2015.

[59] Y. J. Kim, H. S. Bhamra, J. Joseph, and P. P. Irazoqui, "An Ultra-Low-Power RF Energy-Harvesting Transceiver for Multiple-Node Sensor Application," IEEE Transactions on Circuits and Systems II: Express Briefs, vol. 62, pp. 1028-1032, 2015.

[60] P. P. Mercier, S. Bandyopadhyay, A. C. Lysaght, K. M. Stankovic, and A. P. Chandrakasan, "A Sub-nW 2.4 GHz Transmitter for Low Data-Rate Sensing Applications," IEEE Journal of Solid-State Circuits, vol. 49, pp. 1463-1474, 2014.

[61] V. K. Chillara, Y.-H. Liu, B. Wang, A. Ba, M. Vidojkovic, K. Philips, et al., "9.8 An 860μW 2.1-to-2.7 GHz all-digital PLL-based frequency modulator with a DTC-assisted snapshot TDC for WPAN (Bluetooth Smart and ZigBee) applications," in 2014 IEEE International Solid-State Circuits Conference Digest of Technical Papers (ISSCC), 2014, pp. 172-173.

[62] A. Musa, W. Deng, T. Siriburanon, M. Miyahara, K. Okada, and A. Matsuzawa, "A Compact, Low-Power and Low-Jitter Dual-Loop Injection Locked PLL Using All-Digital PVT Calibration," IEEE Journal of Solid-State Circuits, vol. 49, pp. 50-60, 2014.

[63] A. Elkholy, S. Saxena, R. K. Nandwana, A. Elshazly, and P. K. Hanumolu, "A 2.0-5.5 GHz Wide Bandwidth Ring-Based Digital Fractional-N PLL With Extended Range Multi-Modulus Divider," IEEE Journal of Solid-State Circuits, vol. PP, pp. 1-14, 2016.

[64] P. P. Mercier, A. C. Lysaght, S. Bandyopadhyay, A. P. Chandrakasan, and K. M. Stankovic, "Energy extraction from the biologic battery in the inner ear," Nat Biotech, vol. 30, pp. 1240-1243, 12//print 2012.

[65] S. Carreon-Bautista, L. Huang, and E. Sanchez-Sinencio, "An Autonomous Energy Harvesting Power Management Unit With Digital Regulation for IoT Applications," IEEE Journal of Solid-State Circuits, vol. 51, pp. 1457-1474, 2016.

[66] C. Ma, C. Hu, J. Cheng, L. Xia, and P. Y. Chiang, "A near-threshold, 0.16 nJ/b OOK-transmitter with 0.18 nJ/b noise-cancelling super-regenerative receiver for the medical implant communications service," IEEE transactions on biomedical circuits and systems, vol. 7, pp. 841-850, 2013.

[67] S. Vaddiraju, Y. Wang, L. Qiang, D. J. Burgess, and F. Papadimitrakopoulos, "Microsphere Erosion in Outer Hydrogel Membranes Creating Macroscopic Porosity to Counter Biofouling-Induced Sensor Degradation," Analytical Chemistry, vol. 84, pp. 8837-8845, 2012/10/16 2012.

[68] J. C. Claussen, A. Kumar, D. B. Jaroch, M. H. Khawaja, A. B. Hibbard, D. M. Porterfield, et al., "Nanostructuring platinum nanoparticles on multilayered graphene petal nanosheets for electrochemical biosensing," Advanced Functional Materials, vol. 22, pp. 3399-3405, 2012.

[69] L. Fang, B. Liang, G. Yang, Y. Hu, Q. Zhu, and X. Ye, "Study of glucose biosensor lifetime improvement in 37 C serum based on PANI enzyme immobilization and PLGA biodegradable membrane," Biosensors and Bioelectronics, vol. 56, pp. 91-96, 2014.

[70] B. Yu, N. Long, Y. Moussy, and F. Moussy, "A long-term flexible minimally-invasive implantable glucose biosensor based on an epoxy-enhanced polyurethane membrane," Biosensors and Bioelectronics, vol. 21, pp. 2275-2282, 2006.

[71] H. Zhang, J. Wang, Z. Wang, F. Zhang, and S. Wang, "Electrodeposition of polyaniline nanostructures: A lamellar structure," Synthetic Metals, vol. 159, pp. 277-281, 2009.

[72] H. Zhou, H. Chen, S. Luo, J. Chen, W. Wei, and Y. Kuang, "Glucose biosensor based on platinum microparticles dispersed in nano-fibrous polyaniline," Biosensors and Bioelectronics, vol. 20, pp. 1305-1311, 2005.

[73] D. Zhai, B. Liu, Y. Shi, L. Pan, Y. Wang, W. Li, et al., "Highly sensitive glucose sensor based on Pt nanoparticle/polyaniline hydrogel heterostructures," ACS nano, vol. 7, pp. 3540-3546, 2013.

[74] A. Kumar, N. Ayyagari, and T. S. Fisher, "Effects of Graphene Nanopetal Outgrowths on Internal Thermal Interface Resistance in Composites," ACS Applied Materials & Interfaces, vol. 8, pp. 6678-6684, 2016/03/16 2016.

[75] F. Tuinstra and J. L. Koenig, "Raman spectrum of graphite," The Journal of Chemical Physics, vol. 53, pp. 1126-1130, 1970.

[76] L. Malard, M. Pimenta, G. Dresselhaus, and M. Dresselhaus, "Raman spectroscopy in graphene," Physics Reports, vol. 473, pp. 51-87, 2009.

[77] Q. Liu, L. Liu, K. Xie, Y. Meng, H. Wu, G. Wang, et al., "Synergistic effect of ar-GO/PANI nanocomposite electrode based air working ionic actuator with a large actuation stroke and long-term durability," Journal of Materials Chemistry A, vol. 3, pp. 8380-8388, 2015.

[78] J. Wang, "Nanomaterial-based electrochemical biosensors," Analyst, vol. 130, pp. 421-426, 2005.

[79] C. Dhand, M. Das, M. Datta, and B. Malhotra, "Recent advances in polyaniline based biosensors," Biosensors and Bioelectronics, vol. 26, pp. 2811-2821, 2011.

[80] V. Gade, D. Shirale, P. Gaikwad, P. Savale, K. Kakde, H. Kharat, et al., "Immobilization of GOD on electrochemically synthesized Ppy–PVS composite film by cross-linking via glutaraldehyde for determination of glucose," Reactive and Functional Polymers, vol. 66, pp. 1420-1426, 2006.

[81] S. J. Updike, M. C. Shults, R. K. Rhodes, B. J. Gilligan, J. O. Luebow, and D. Von Heimburg, "Enzymatic Glucose Sensors: Improved Long-Term Performance In Vitro and In Vivo," ASAIO Journal, vol. 40, pp. 157-163, 1994.

[82] H. Lee, T. K. Choi, Y. B. Lee, H. R. Cho, R. Ghaffari, L. Wang, et al., "A graphene-based electrochemical device with thermoresponsive microneedles for diabetes monitoring and therapy," Nat Nano, vol. 11, pp. 566-572, 06//print 2016.

[83] X. You and J. J. Pak, "Graphene-based field effect transistor enzymatic glucose biosensor using silk protein for enzyme immobilization and device substrate," Sensors and Actuators B: Chemical, vol. 202, pp. 1357-1365, 2014.

[84] A. J. Bandodkar, W. Jia, C. Yardımcı, X. Wang, J. Ramirez, and J. Wang, "Tattoo-based noninvasive glucose monitoring: a proof-of-concept study," Analytical chemistry, vol. 87, pp. 394-398, 2014.

[85] H. Tang, F. Yan, P. Lin, J. Xu, and H. L. W. Chan, "Highly Sensitive Glucose Biosensors Based on Organic Electrochemical Transistors Using Platinum Gate Electrodes Modified with Enzyme and Nanomaterials," Advanced Functional Materials, vol. 21, pp. 2264-2272, 2011.

[86] J. H. Luong, K. B. Male, and J. D. Glennon, "Biosensor technology: technology push versus market pull," Biotechnology advances, vol. 26, pp. 492-500, 2008.

[87] C. Jurysta, N. Bulur, B. Oguzhan, I. Satman, T. M. Yilmaz, W. J. Malaisse, et al., "Journal of biomedicine & biotechnology Volume: 2009 ISSN: 1110-7251 ISO Abbreviation: J. Biomed. Biotechnol. Publication Date: 2009," Detail:.

[88] J. D. Lane, D. M. Krumholz, R. A. Sack, and C. Morris, "Tear glucose dynamics in diabetes mellitus," Current eye research, vol. 31, pp. 895-901, 2006.

[89] M. Miyashita, N. Ito, S. Ikeda, T. Murayama, K. Oguma, and J. Kimura, "Development of urine glucose meter based on micro-planer amperometric biosensor and its clinical application for self-monitoring of urine glucose," Biosensors and Bioelectronics, vol. 24, pp. 1336-1340, 2009.

VITA

VITA

Young-Joon Kim received B.S. and M.S. degree in Electrical and Engineering from Korea Advanced Institute of Science and Technology, Daejeon, South Korea in 2008 and 2010. Since 2011, he is pursuing Ph.D. degree with Department of Electrical and Computer Engineering at Purdue University, West Lafayette, IN. His current interests are CMOS IC design, wireless power transfer, advanced packaging on flexible substrate and biosensor.